



Understanding the Most Powerful Explosions in the Universe

Sarah L. Gibson

Supervisors:

Paul O'Brien

Julian Osborne

Thesis to be submitted for the degree of
Doctor of Philosophy
at the University of Leicester.

X-ray & Observational Astronomy Group
Department of Physics and Astronomy
University of Leicester

November 18, 2018

Understanding the Most Powerful Explosions in the Universe

Sarah L. Gibson

Abstract

Gamma-ray bursts (GRBs) are the most luminous transient events in the Universe. The population of observed GRBs is organised into two categories: long and short, separated by a two second divide in gamma-ray emission duration. The short type (lasting less than two seconds) have been shown to originate from the merger of two neutron stars, whereas as long bursts (lasting longer than two seconds) originate from the collapse of massive stars. There are subtypes within both classes that challenge the standard model for GRBs. For shorts, some bursts exhibit a re-brightening in their high-energy emission becoming dominant shortly after the initial emission spike known as extended emission bursts. For long bursts, some exhibit flares in their X-ray afterglows that contain a comparable amount of energy to the prompt emission. These are so-called giant X-ray flares.

This thesis examines the central engine that drives these extreme types of bursts since they have the potential to discern between various proposed GRB models. A potential explanation for these events may be a highly magnetised, rapidly rotating neutron star (magnetar) fed by fallback accretion. The motivation for using this model is the late-time plateaux seen in some short GRBs that can be interpreted as a long-lived magnetar losing angular momentum along magnetic field lines. The fallback accretion component extends the global energy budget of the system and allows the rotational energy reservoir of the magnetar to be refreshed.

Declaration

I hereby declare that no part of this thesis has been previously submitted to this or any other University as part of the requirement for a higher degree. The work herein was conducted by the undersigned except for contributions as acknowledged in the text.

Sarah L. Gibson

November 18, 2018

Acknowledgements

Like many Ph.D. theses, this was a labour of love, frustration, and a lot of other emotions. I owe it's completion to the support I received from a lot of people over the duration, whose influence on my life has ranged from mentor to lifelong friends.

My unending gratitude goes to Graham Wynn who took on this project and was a constant source of knowledge, support, and advice that reached beyond the contents of these pages. My thanks go to Ben Gompertz, Klaas Wiersama and other members of the G17 office that offered support, helpful discussions, and made it a pleasant place to work. Also to Kim Page (thanks for the chocolate and letting me off duty whenever I was travelling!), Phil Evans, the rest of the Swift team, and Paul O'Brien.

I made a lot of lifelong friends during my time at Leicester. There isn't enough space to thank everyone individually, but special mentions go to Claudia Belardi, Bec Nealon for pushing me to be my best, Mark Fletcher, Neil Humpage who was always up for a gig, Jamie Williams, Stuart Turner, Emily Jane Watkinson, Chris Moore, Jordan Penney, Emma Longstaff, Katie Dexter, among many others. From my younger years, I need to thank Ben Gardner and especially Joe Heward for all the pizza and cups of tea. And to Sinéad for always being an understanding ear.

I'd like to thank my rock and roll brothers in The Lab: Ash Stevenson, Ed Parnell, and Liam Mills. The band provided an outlet for me when I needed it most and I'll be forever proud of us for rocking the Glastonbudget stage!

I owe a huge debt of thanks to my mum who has always supported me in everything I've done, always made sure I was happy and set up in my home life, and always goes out of her way to set me up again when it's time to move on to the next chapter of my life. Thanks for being my mum.

Also thanks to Ashbee, Bo, Chester, and Oscar for all of the fluffy cuddles.

Publications

Fallback accretion on to a newborn magnetar: short GRBs with extended emission

S. L. Gibson, G. A. Wynn, B. P. Gompertz and P. T. O'Brien

2017, MNRAS 470, 4925

Fallback accretion on to a newborn magnetar: long GRBs with giant X-ray flares

S. L. Gibson, G. A. Wynn, B. P. Gompertz and P. T. O'Brien

2018, MNRAS 478, 4323

This work is dedicated to Beryl Gibson

without her support and faith, I could not have succeeded

Contents

1	Introduction	1
1.1	History	2
1.1.1	Origins	2
1.1.2	X-ray detection	3
1.1.3	<i>Swift</i> era of Gamma-ray Burst detections	3
1.2	The <i>Swift</i> Gamma-ray Burst Mission	4
1.2.1	Burst Alert Telescope	4
1.2.2	X-Ray Telescope	6
1.2.3	Ultra-Violet/Optical Telescope	7
1.2.4	Other Gamma-ray Burst Missions	7
1.3	Gamma-ray Burst Classification	8
1.3.1	Long Gamma-ray Bursts	8

1.3.2	Short Gamma-ray Bursts	10
1.4	Emission Mechanisms	11
1.4.1	Observational Constraints on Emission	13
1.4.2	Prompt Emission	14
1.4.3	Afterglow	14
1.4.4	X-ray Afterglow	15
1.4.5	Central Engines	17
1.5	Magnetars	19
1.5.1	Neutron Stars	19
1.5.2	Field Amplification	19
1.6	This Thesis	20
2	The Magnetar Propeller Model with Fallback Accretion	21
2.1	Introduction	22
2.2	The Magnetic Propeller Model	23
2.2.1	Expelling Material from the Gravitational Potential Well of the Magnetar	29
2.3	Comparing Dipole Torque Equations	31
2.4	Exploring Parameter Space	33
2.4.1	Magnetar Properties	33

2.4.2	Comparing Types to Previous Work	37
2.5	Preliminary Fitting	38
2.5.1	Correlations	42
2.6	Summary	45
3	Fallback Accretion on to a Newborn Magnetar: Short GRBs with Extended Emission	47
3.1	Introduction	48
3.2	<i>Swift</i> SGRB with Extended Emission Sample	50
3.3	Optimisation Routine	51
3.4	Results and Discussion	53
3.4.1	GRB 050724	59
3.4.2	GRB 060614	60
3.4.3	GRB 111121A	61
3.4.4	Refitting Excluding Early-Time Data	63
3.4.5	Refitting with Enhanced Dipole Torque	67
3.4.6	The B-P Landscape	70
3.5	Conclusions	72
4	Fallback Accretion on to a Newborn Magnetar: Long GRBs with Giant X-ray Flares	73
4.1	Introduction	74

4.2	Sample of <i>Swift</i> LGRBs with Giant X-ray Flares	76
4.3	Optimisation Routine	77
4.4	Results and Discussion	79
4.5	Conclusions	87
5	Conclusions and Future Work	88
5.1	Key Conclusions	89
5.2	Future Work	93
5.2.1	Pulse Model	94
5.2.2	Methodology	95
5.2.3	Preliminary Results	96
A	Alfvén Radius Derivation	98
B	Exploded Plots of Burst Types	100
C	Correlations between Fitting Parameters	104
	Bibliography	108

List of Figures

1.1	The isotropic distribution of GRBs detected by BATSE across the sky.	3
1.2	The <i>Swift</i> satellite.	5
1.3	The observed T_{90} bimodality.	9
1.4	A schematic of the relativistic fireball model.	12
1.5	The ‘canonical’ X-ray afterglow.	16
2.1	The “switch-on” of propeller efficiency as a function of n	26
2.2	A demonstration of how the fallback parameters affect the magnetar properties over time.	28
2.3	A comparison of dipole torque equations.	32
2.4	A comparison of of light curves, mass transfer and radii for each burst type classification.	35
2.5	Exploded view of a burst showing effect of varying the fallback parameters on a type I synthetic burst.	37

2.6	A comparison of light curves generated with and without fallback accretion. . . .	39
2.7	The model results of MCMC fitting to a synthetic light curve.	43
2.8	A scatterplot matrix showing correlations between fitting parameters for a fit to a type I synthetic light curve.	44
3.1	Results of fitting the magnetar propeller model with fallback accretion to the SGRB sample with extended emission.	55
3.2	A comparison of beaming angles.	57
3.3	GRB 050724: comparative plot.	60
3.4	GRB 060614: comparative plot.	61
3.5	GRB 111121A: comparative plot.	62
3.6	Results of fitting to the SGRB sample with extended emission excluding early-time data.	65
3.7	The models fitted to the SGRB sample with extended emission using the enhanced dipole torque equation and excluding early-time data.	68
3.8	Plot of B and P_i values for different GRB fitting works.	71
4.1	Results of fitting the magnetar propeller model with fallback accretion to the LGRB sample with giant X-ray flares.	80
4.2	B - P_i and emitted energy to spin energy ratio plots of the LGRB sample with giant X-ray flares.	83
5.1	A scatterplot matrix of the results of fitting to GRB 061006 using $n = 1$ and $p = 9$.	91

5.2	A scatterplot matrix of the results of fitting to GRB 070704.	92
5.3	An example pulse to be used in a self-organised criticality regime.	94
5.4	Preliminary results of light curve matching using the pulse model.	97
B.1	Exploded view of a burst showing effect of varying the fallback parameters on a type II synthetic burst.	101
B.2	Exploded view of a burst showing effect of varying the fallback parameters on a type III synthetic burst.	102
B.3	Exploded view of a burst showing effect of varying the fallback parameters on a type IV synthetic burst.	103
C.1	A scatterplot matrix showing correlations between fitting parameters for a fit to a type II synthetic light curve.	105
C.2	A scatterplot matrix showing correlations between fitting parameters for a fit to a type III synthetic light curve.	106
C.3	A scatterplot matrix showing correlations between fitting parameters for a fit to a type IV synthetic light curve.	107

List of Tables

2.1	The values used for the parameter variation test of the magnetar propeller with fallback accretion model.	33
2.2	The parameters used to compare light curves generated by models with and without fallback accretion.	38
2.3	The parameter limits used in the MCMC routine.	40
2.4	The parameters used to generate synthetic light curves.	40
2.5	The results of MCMC fitting to synthetic light curves.	41
3.1	The k -correction parameters for the SGRB sample with extended emission. . . .	51
3.2	Upper and lower MCMC limits used to fit to <i>Swift</i> data.	52
3.3	AICc values of various fits to the SGRB sample with extended emission.	54
3.4	Comparison of jet half-opening angles.	56
3.5	The parameters derived from the fits to the SGRB sample with extended emission.	58

3.6	AICc values for fits to SGRB sample with extended emission excluding early-time data.	64
3.7	The parameters derived from the fits to the SGRB sample with extended emission excluding early-time data.	66
3.8	The AICc values for fits to the SGRB sample with extended emission using enhanced dipole torque equation and excluding early-time data.	67
3.9	The parameters derived from fits to the SGRB sample with extended emission using the enhanced dipole torque equation and excluding early-time data.	69
4.1	The k -correction parameters for the LGRB sample with giant X-ray flares.	78
4.2	The parameters derived from the fits to the LGRB sample with giant X-ray flares.	82
4.3	χ^2_ν values for fits with restricted efficiencies.	85
4.4	Lorentz factors of the LGRB with giant X-ray flare sample.	86

1

Introduction

Gamma-ray bursts (GRBs) are the brightest, most intense explosions in the Universe. They are very brief flashes of gamma-rays that last from a fraction of a second to several thousand seconds and occur at a rate of a few per day at random locations. While they are active, GRBs outshine every other source of gamma-rays in the sky including the Sun. Many questions about the more erratic features of these extreme events still remain even within the understanding of the physical processes involved brought about from over four decades of study. This thesis will endeavour to understand the mechanics of the central engines required to power the strangest of these already extreme events.

1.1 History

GRBs were discovered serendipitously by the Vela satellites in the late 1960s. This U.S. satellite network was originally launched to monitor secret nuclear testing by the USSR in breach of the Nuclear Test Ban Treaty (1963). However, the short bursts of gamma-ray radiation detected by Vela were confirmed to originate neither from the Earth nor the Sun, and were finally made public six years after detection (Klebasedel et al., 1973). The observed transient events had durations in the range 0.1 to ~ 30 seconds, with a time-integrated flux in the region $10^{-5} - 2 \times 10^{-4}$ erg cm $^{-2}$, in the energy range 0.2 – 1.5 MeV. Various theories arose regarding the nature of these events, very few of which could be ruled out by the data collected at the time. It was therefore unclear as to whether GRBs originated from within or outside our Galaxy due to the incredible energy releases involved. It was noted that the flashes appeared to have several types due to variances in time profiles, durations, and spectral shapes (Mazets & Golenetskii, 1981).

1.1.1 Origins

The Compton Gamma-Ray Observatory (CGRO), launched in 1991, provided the first steps to understanding GRBs. The Burst and Transient Spectrometer Experiment (BATSE; Fishman et al. 1985) instrument onboard CGRO performed an all-sky survey of GRBs showing that they were distributed isotropically (Meegan et al. 1992; Fig. 1.1¹) and possessed a broad range of fluxes. This gave favour to a cosmological origin for GRBs, rather than a galactic or local population origin. At cosmological distances, GRBs would outshine galaxies and quasars by a large factor which implied a catastrophic energy release if they truly originated from outside the Milky Way.

¹<http://gammaray.nsstc.nasa.gov/batse/grb/skymap/>

2704 BATSE Gamma-Ray Bursts

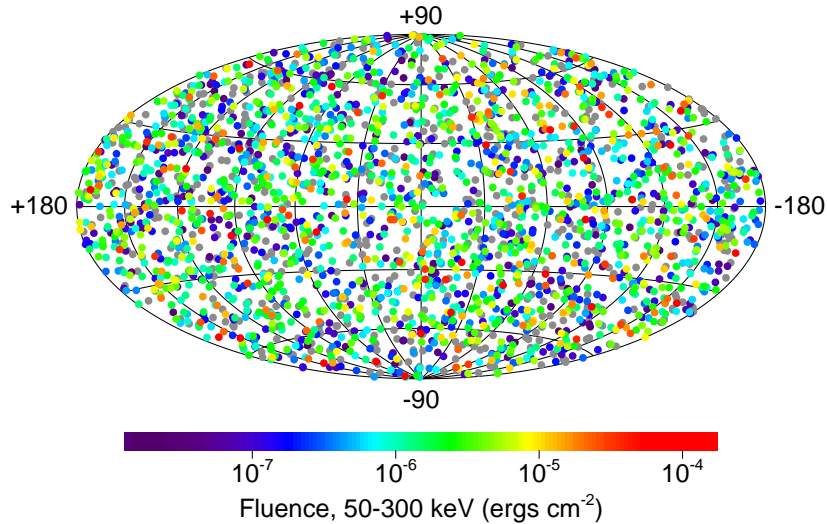


Figure 1.1: The isotropic distribution of GRBs detected by BATSE across the sky.

1.1.2 X-ray detection

From 1997, the Dutch-Italian satellite Beppo-SAX and its on-board X-ray telescope (Boella et al., 1997) began to observe GRBs within 5 – 12 hours after the trigger time, which resulted in the first detection of fading X-ray afterglows following the gamma-ray emission and accurate localisations to within a few arcminutes. The enhanced positions Beppo-SAX provided allowed ground-based observatories, in various wavelengths, to perform follow-up observations that led to the first optical afterglow detection (van Paradijs et al., 1997) and the first redshift measurement (Metzger et al., 1997). This conclusively proved that at least some of GRBs occur at cosmological distances.

1.1.3 *Swift* era of Gamma-ray Burst detections

The *Neil Gehrels Swift* satellite (hereafter referred to as *Swift*), launched in 2004, represents the most recent wave in significant advances in GRB physics (Gehrels et al., 2004). *Swift* is a multi-

wavelength observatory dedicated to GRB hunting with rapid slewing capabilities. It therefore achieved the long-awaited goal of acquiring accurate afterglow localisations and detailed X-ray light curves in approximately a minute following the burst detection. Such a feat was impossible with other available observatories of the time. The detailed light curves *Swift* produced demonstrated the smooth transition between the prompt and afterglow emission phases and revealed striking new insights into X-ray afterglow behaviour and GRB physics (Mészáros, 2006; Gehrels et al., 2009; Gehrels & Razzaque, 2013). *Swift* succeeded in localising the first afterglow from short GRBs in May 2005 which gave rise to a galaxy identification for this class. *Swift* also broke through the symbolic redshift $z > 6$ barrier and holds the records for observing the most distant GRBs: $z = 8.2$ for a spectroscopically confirmed redshift (Tanvir et al., 2009), and $z \simeq 9.4$ photometrically (Cucchiara et al., 2011). For a review of the *Swift* mission, see Gehrels et al. (2009); Gehrels & Razzaque (2013); Mészáros & Rees (2014).

1.2 The *Swift* Gamma-ray Burst Mission

The *Swift* mission provided the data used in this thesis; therefore, a more in-depth look into its operations over other missions is pertinent. *Swift* carries three instruments (Fig. 1.2²) which are described below.

1.2.1 Burst Alert Telescope

The Burst Alert Telescope (BAT; Barthelmy et al. 2005) is a coded-aperture imaging detector with a wide (1.4 steradian half coded) field of view, operating over the energy band 15 – 150 keV with an energy resolution of ~ 7 keV, and a fluence sensitivity of $\sim 10^{-8}$ erg cm⁻² s⁻¹. Within ~ 10 seconds of detecting a burst, BAT calculates the burst’s position to within a 1 – 4 arcminute accuracy, decides if the burst merits a spacecraft slew ($> 6.5\sigma$ significance) using onboard software, and passes the position to the spacecraft to perform an autonomous slew, bringing the burst into

²http://swift.gsfc.nasa.gov/about_swift/Sci_Fact_Sheet.pdf

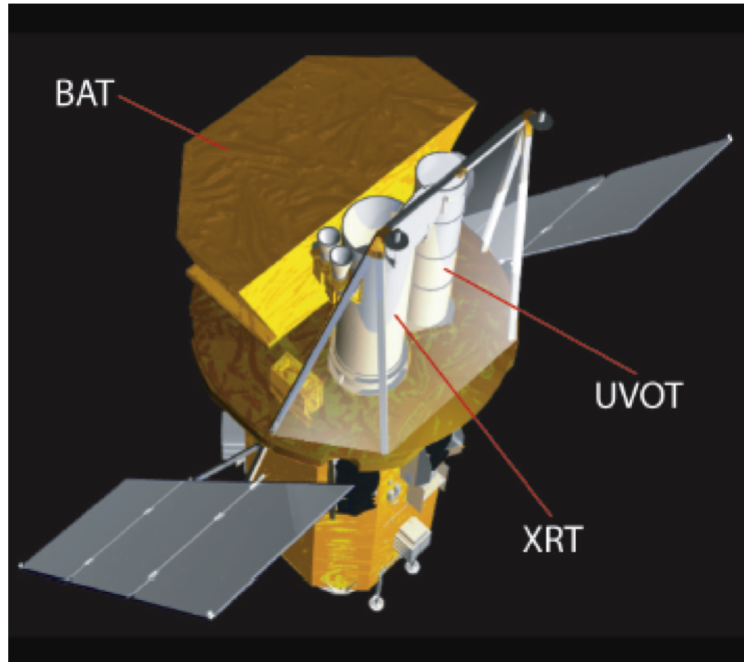


Figure 1.2: An artists impression of the *Swift* satellite with the position of the three instruments indicated (Gehrels et al., 2004).

the field of view of the X-Ray Telescope and the Ultra-Violet/Optical Telescope. The BAT field of view includes that of the X-Ray Telescope and the Ultra-Violet/Optical Telescope so that the GRB emission can be observed in all bands simultaneously after a slew.

BAT has a large dynamical range and multiple trigger capabilities to detect a range of intensities, durations and temporal structures. It has two operational modes: Burst, which finds burst positions; and Survey, which collects the gamma-ray count in 5 minute time bins over 18 energy bands to search for hard X-ray transients, as well as being used to follow up any target of opportunity requests. The burst trigger algorithm looks for excesses in the count rate above the expected background and constant sources. An imaging algorithm is then used to check the origin corresponds to a point source, making a GRB the most likely source. The sky location and intensity of the source are then immediately sent to the ground and distributed to a variety of ground- and space-based telescopes through NASA's Tracking and Data Relay Satellite System (TDRSS; Poza 1981) and the GRB Coordinates Network (GCN, formerly BACODINE; Barthelmy et al. 1994) for rapid follow-up observations while the GRB is still bright.

1.2.2 X-Ray Telescope

The X-ray Telescope (XRT; Burrows et al. 2005a) is a grazing incidence Wolter Type I imaging spectrometer designed to measure fluxes, spectra, and light curves over a sensitivity range greater than 7 orders of magnitude in the 0.3 – 10 keV energy band. It is a narrow-field instrument with a 23.6×23.6 arcminute field of view, with 7 arcsecond (full-width, half-maximum) resolution, and has a sensitivity of 2×10^{-14} erg cm⁻² s⁻¹ in 10⁴ seconds. The XRT can improve a 1 – 4 arcminute localisation from BAT to within 2.5 arcseconds (usually ~ 4 arcseconds including noise) within ~ 10 seconds of target acquisition for a typical GRB. This level of precision combined with an information delivery time of just 1 – 2 minutes allows ground-based telescopes to begin follow-up observations. XRT studies X-ray counterparts from ~ 20 – 70 seconds after acquisition up to days or weeks after.

The XRT has multiple readout modes that can be autonomously selected by the craft. Unfortunately, one of these, Photon Diode mode, was lost due to a micrometeorite strike within the first six months of the mission. The remaining functioning modes are as follows.

1. Imaging Mode is used when XRT first acquires the target. It produces an integrated image measuring the total energy deposited per pixel and is used to calculate accurate positions. Exposure times are 0.1 or 2.5 seconds. Imaging Mode produces no spectroscopic data due to high pile up from large count rates; however, it provides reasonable flux estimates.
2. Windowed Timing Mode can perform high time resolution (2.2 ms) spectroscopy by continuously clocking the central 8 arcminutes of the CCD. Imaging information is preserved only in one direction, hence position accuracy is lost. Windowed Timing mode is used to protect the CCD from becoming oversaturated during high source flux periods and while the spacecraft is slewing.
3. Photon Counting Mode uses a ‘normal’ CCD readout to provide full resolution spectral and imaging information for fluxes in the range $\sim 10^{-14}$ – 10^{-11} erg cm⁻² s⁻¹, but with a 2.5 second temporal resolution. Photon Counting mode is activated once the flux has dropped

below saturation levels (usually occurring within the first few hundred seconds of a GRB) and is, therefore, the most commonly used mode.

Approximately 90% of BAT triggers are followed up by the XRT within ~ 350 seconds of the trigger, while roughly a half are followed up within ~ 100 seconds. XRT data are automatically analysed by the UK *Swift* Science Data Centre (UKSSDC³), see Evans et al. (2007, 2009).

1.2.3 Ultra-Violet/Optical Telescope

The Ultra-Violet/Optical Telescope (UVOT; Roming et al. 2005) is a 30-cm modified Ritchey-Chrétien telescope co-aligned with the XRT and operates in the 170 – 600 nm band. UVOT has two filter wheels both with 11 positions characterised in Roming et al. (2005) (Table 2). UVOT creates a 100 second exposure finding chart, which is sent to ground-based observatories via TDRSS and GCNs. The finding chart has positional accuracy of ~ 0.3 arcseconds and, when combined with XRT, can improve the localisation of a burst to $\sim 1 - 2$ arcseconds (Goad et al., 2007). Only $\sim 30\%$ of BAT triggers are detected with UVOT.

1.2.4 Other Gamma-ray Burst Missions

While *Swift* is currently the only dedicated GRB hunter, there are other missions operating with a focus on GRB physics. Some notable missions are listed below, though this list is not exhaustive.

- The *Fermi* Gamma-ray Space Telescope (*Fermi*; Ritz et al. 2009) mission was launched by NASA in 2008 and carries two instruments: the Large Area Telescope (LAT; Atwood et al. 2009) and the Gamma-ray Burst Monitor (GBM; Meegan et al. 2009). The GBM has poor localisation capabilities, whereas the LAT is a powerful instrument for observing GRBs due to its good angular resolution for source localisation; high sensitivity over a broad field

³www.swift.ac.uk

of view to monitor and detect transients; good calorimetry over an extended energy band to study spectral breaks and cutoffs; and good calibration and stability for long term flux measurement.

- The Konus-Wind instrument onboard the Global Geospace Science satellite (GGS-Wind, launched in 1994; Aptekar et al. 1995) contributes to the Inter-Planetary Network (IPN) which uses data from pairs of satellites to triangulate GRB positions. Other contributors include *Swift*, HETE-2, and Mars Odyssey.
- The International Gamma-Ray Astrophysics Laboratory (INTEGRAL, launched in 2002; Winkler et al. 1993) has a very high sensitivity and is therefore mostly used to detect the faintest GRB populations.

1.3 Gamma-ray Burst Classification

A bimodal distribution in the temporal and spectral properties of GRB emission can be identified in BATSE's sample (Kouveliotou et al. 1993; Fig. 1.3). This results in two broad classes of GRB: long-soft and short-hard (LGRBs and SGRBs respectively). The T_{90} property is defined as the time period over which 90% of gamma-ray photons are detected and the two classes sit either side of a $T_{90} \simeq 2$ seconds divide. This strong bimodality is convincing evidence for separate physical origins for the classes of GRB. However, a strict T_{90} cut at 2 seconds risks including GRBs in the tail of the other class since the distributions experience significant overlap. As a result, the T_{90} definition has been criticised (*e.g.*, Bromberg et al. 2013) *e.g.*, a third, intermediate group may exist but could also be related to detector biases (see Ripa & Mészáros, 2015, for a review).

1.3.1 Long Gamma-ray Bursts

In 1998, supernova 1998bw was detected within the position error box of GRB 980425 (Galama et al., 1998) and this provided the first observational clue to the origin of LGRBs. Further sup-

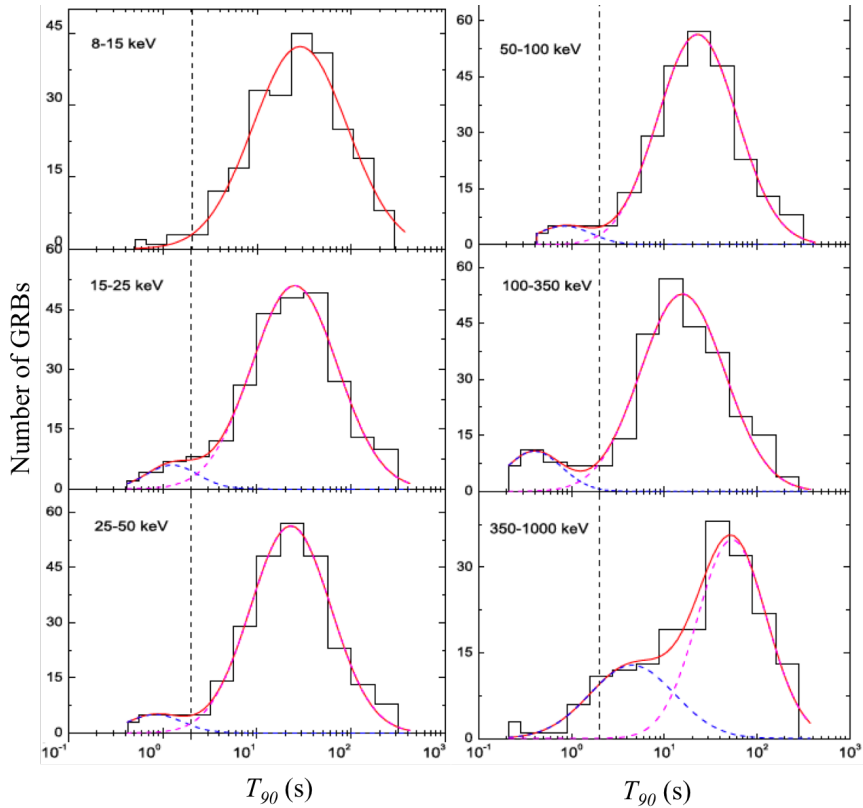


Figure 1.3: The T_{90} bimodality observed in different energy bands (Qin et al., 2012).

porting evidence for a GRB-supernova connection arose through the detection of small ‘bumps’ at late times in some GRB optical afterglow light curves (*e.g.*, Bloom et al. 1999b; Galama et al. 2000), which are a characteristic feature of supernovae. Finally in 2003, the ‘smoking gun’ was detected. The HETE-2 satellite localised GRB 030329, which had an especially bright afterglow, resulting in the first unambiguous association of a GRB with a supernova (SN2003dh). After the optical emission had faded, characteristic features of the supernova were detected in both the light curves and the spectra (Hjorth et al., 2003; Stanek et al., 2003).

These findings are strong evidence in support of the collapsar model (Woosley, 1993; MacFadyen & Woosley, 1999) which describes the formation of LGRBs from the death and core-collapse of massive stars ($> 15M_{\odot}$). Further evidence includes LGRB host galaxies having high star formation rates and low metallicity (Bloom et al., 1998; Djorgovski et al., 1998; Fruchter et al., 1999; Bloom et al., 2002; Wainwright et al., 2007), since massive stars have shorter lifespans and stellar growth can be limited by high metallicity. Studies of the LGRB population show that

they occur closer to star forming regions in fainter, more irregular galaxies than core-collapse supernovae (Fruchter et al., 2006; Svensson et al., 2010) which suggests that they are related to the deaths of the most massive stars in chemically-limited environments.

1.3.2 Short Gamma-ray Bursts

SGRBs are detected less frequently than LGRBs because they are much shorter lived and have much fainter afterglows, so the observational breakthrough regarding their progenitors has been greatly delayed compared to that for LGRBs. It has long been considered that SGRB progenitors are from a different population to LGRBs since their temporal and spectral properties are so distinct from each other. A lack of supernova detections in deep searches of SGRB fields (*e.g.*, GRB 050509B, Bloom et al. 2006; GRB 050709, Fox et al. 2005) is convincing evidence to rule out massive stars undergoing core-collapse supernovae as progenitors. SGRBs have been observed in a range of environments including: old elliptical galaxies with very little star formation (Gehrels et al., 2005), young galaxies similar to hosts of long bursts (D’Avanzo et al., 2009), and in the intergalactic medium with large offsets from any potential hosts (Berger, 2010; Tunnicliffe et al., 2014) which also indicates a different origin to LGRBs.

The most popular candidates have long been compact object binary mergers (Paczynski, 1986; Fryer et al., 1999; Rosswog et al., 2003; Belczynski et al., 2006; Chapman et al., 2007) - most likely a neutron star binary merger or a black hole-neutron star merger. These systems lose orbital angular momentum by radiating gravitational waves and spiral into each other, eventually merging, which provides the energy release required to power the GRB. A compact object binary system would have to evolve off the main sequence and have both stars collapse (often receiving a large natal ‘kick’ in the process, Bloom et al. 1999a; Grindlay et al. 2006) before producing an SGRB which explains why they are observed with offsets from star forming regions or host galaxies.

On August 17, 2017 at 12:41:04 UTC, the Advanced Laser Interferometry Gravitational wave Observatory (LIGO) and Advanced Virgo detector network observed gravitational waves from

the inspiral of a binary neutron star system (GW170817; Abbott et al. 2017a) which had near-simultaneous observations of the short burst GRB 170817A by the *Fermi* and INTEGRAL satellites (Abbott et al., 2017b; Goldstein et al., 2017; Savchenko et al., 2017) thus providing the ‘smoking gun’ evidence that double neutron star mergers are the progenitors of SGRBs. The localisation from the gravitational wave detectors and space-based satellites allowed for a multitude of ground-based follow-up observations across all wavelengths and timescales (Abbott et al., 2017c) inaugurating the field into era of gravitational wave/electromagnetic multi-messenger astronomy.

This discovery also led to the first well-sampled light curve of a kilonova associated with an SGRB (Villar et al., 2017; Gompertz et al., 2017). A compact object binary merger is expected to produce a faint optical/near-infrared transient (known as a kilonova or ‘macronova’) as neutron-rich ejecta forms heavy elements via rapid neutron capture (*r*-process) nucleosynthesis, which then decays radioactively. Since GRB 170817A was observed off-axis and no X-ray afterglow was immediately detected (Evans et al., 2017), this allowed the kilonova to be observed completely independently of any afterglow emission from the associated GRB. Hence Gompertz et al. (2017) could compare this observation to previously confirmed and suspected kilonovae. Gompertz et al. (2017) suggests that the diversity of kilonova emission and the absence of kilonovae from some SGRBs could be a product of the merger type, *i.e.*, double neutron star versus black hole-neutron star, since more material can be ejected in a black hole-neutron star merger to power the kilonova.

1.4 Emission Mechanisms

GRB emission is traditionally classified as either ‘prompt’ or ‘afterglow’ emission. The prompt emission refers to the initial burst of gamma-rays (and on occasion any simultaneous observations in lower frequencies, such as hard X-rays or optical flashes) whereas the afterglow encompasses all emissions in other bands, from X-rays down to radio. This nomenclature can be misleading however (Zhang, 2007), since some hard X-ray flares can be detected by gamma-ray detectors and central engines can remain active for long durations after the main burst (*e.g.*, dipole spin-

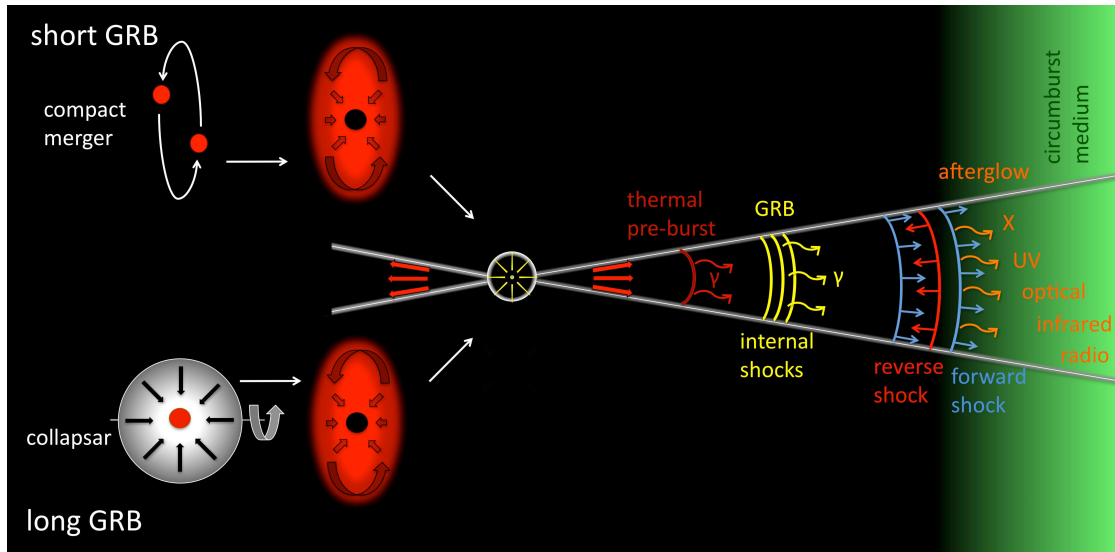


Figure 1.4: A schematic of the relativistic fireball model from Gomboc (2012) depicting the two favoured progenitor routes.

down emission, Zhang & Mészáros 2001), driving emissions that could be classed as afterglow. Therefore, it is often more useful to consider GRB emission to be either ‘internal’ (*i.e.*, powered by the central engine) or ‘external’ (*i.e.*, produced in the surrounding medium of the GRB).

The physics of GRB emission can be explained using the fireball shock model (Goodman, 1986; Paczynski, 1986). For reviews, see Piran (1999); Mészáros (2002); Zhang & Mészáros (2004); Mészáros (2006). An instantaneous release of a large amount of gravitational energy forms a relativistically expanding fireball and the GRB is borne from the dissipation of the energy contained within the outflow. The prompt gamma-ray emission is produced by energy dissipation from within the flow, while the afterglow is produced via external shocks between the outflow and an external medium, see Fig. 1.4.

1.4.1 Observational Constraints on Emission

GRB emission shows variability on a timescale on the order of milliseconds. This demands a very compact emission region via a simple causality relation

$$D < c\Delta t \tag{1.1}$$

where D is the size of the emitting region, c is the speed of light and Δt is the observed minimum variability timescale.

The cosmological distances of GRBs require that their gamma-ray energy release be of the order of 10^{52} erg. and the required compactness of the progenitor constrains the radiation to emit thermally via a blackbody spectrum. However, the observed spectra are non-thermal. This is a contradiction known as the compactness problem and it can be solved by assuming that the emission source is moving ultra-relativistically towards the observer. The emission region would increase in size by a factor of $2\gamma^2$ (where γ is the Lorentz factor) due to the temporal term in Equation (1.1) being replaced with the rest frame time.

The inferred isotropic broadband energy can be as high as 10^{54} erg for some GRBs, which is an astounding output that a compact progenitor would struggle to produce. The strain on the energy budget can be relaxed by factors in the range of 100 – 1,000 if the outflow is collimated into a jet. Observationally, this jetted structure has been supported by achromatic jet breaks in GRB light curves (Harrison et al., 1999; Panaitescu & Kumar, 2001; Soderberg et al., 2006; Racusin et al., 2009). The observer must be aligned very closely with the jet axis for the emission to trigger a gamma-ray detector. This indicates that, initially, it is strongly beamed towards the observer with an opening angle of $\theta = 1/\Gamma$ (where Γ is the bulk Lorentz factor of the outflow). The beaming effect ensures that, initially, only emission from the jet is observed and it cannot be distinguished from the isotropic case. The jetted structure of the emission becomes apparent as the blast wave decelerates (causing a decrease in Γ) and the beaming angle becomes greater than the physical opening angle of the jet. Lower fluxes than the isotropic case are observed which causes an achromatic steepening in the light curves.

1.4.2 Prompt Emission

According to the fireball model (Goodman, 1986; Paczynski, 1986), the ultimate energy source of GRBs is a catastrophic energy release event: either the core-collapse supernova of a massive star or the merger of a compact object binary system. The freed gravitational energy is deposited into an explosion driven by thermal processes. The fireball expands and accelerates to relativistic speeds (Cavallo & Rees, 1978; Goodman, 1986; Paczynski, 1986, 1990) due to internal thermal and/or magnetic pressures and a series of shells with a range of Lorentz factors is formed from the ejecta. As shells with higher Lorentz factors catch up with slower moving shells, a shock front (known as an ‘internal’ shock; Rees & Meszaros 1994) is formed and the kinetic energy of the outflow is converted into electromagnetic radiation. This is generally considered to be the main site of the prompt emission, though magnetic dissipation could be responsible without shocks (Zhang & Yan, 2011).

The prompt emission can consist of a series of pulses with a fast-rise, exponential-decay shape (Norris et al., 1996) which do not appear to evolve with time (Ramirez-Ruiz & Fenimore, 2000). LGRBs exhibit a spectral lag where lower frequency photons arrive at a later time compared to higher energy photons with a time delay in the range of 10 – 2000 milliseconds.

The spectra of prompt emission are usually fitted with the Band function (Band et al., 1993) which is a phenomenological model consisting of a broken power law that is steeper at high energies and has an exponential cut-off at lower energies.

1.4.3 Afterglow

The blast wave expands outwards and collides with the circumburst material, sweeping up particles as it proceeds. Strong shock fronts are formed at the head of the ejecta through the interaction between the blast wave and circumburst material: a forward shock propagates out into the circumburst material, whilst a short-lived reverse shock travels back through the ejecta (Rees & Meszaros, 1992; Mészáros & Rees, 1993, 1997, 1999). These shocks produce the broadband

afterglow emission.

Electrons crossing the magnetised boundary between the ejecta and the circumburst material result in the shock front radiating synchrotron emission. At early times, the electrons are excited into energy states with short cooling times, known as the ‘fast cooling’ regime. The synchrotron peak frequency corresponds to the minimum and most common Lorentz factor of the electrons and moves to lower frequencies with time. Once this has shifted below the cooling break (where the cooling time of the electrons becomes short compared to the expansion time, Mészáros 2002), the system is then in the ‘slow cooling’ regime (Sari et al., 1998; Wijers & Galama, 1999). The peak frequency will continue to move to increasingly lower frequencies until it falls below the self-absorption frequency. At this point, the medium becomes optically thick which corresponds to a dramatic drop in luminosity.

1.4.4 X-ray Afterglow

The detailed X-ray observations provided by *Swift*-XRT gave rise to a ‘canonical’ X-ray afterglow (Nousek et al., 2006; O’Brien et al., 2006; Zhang et al., 2006), shown in Fig. 1.5, that can consist of up to five stages characterised by an X-ray flux, $F_X \propto t^{-\alpha}$, and an energy spectrum, $F_\nu \propto \nu^{-\beta}$, where α and β are the temporal and spectral indices respectively. *Swift* also demonstrated that the transition between the prompt emission and afterglow phase is a smooth one. It should be noted that stages 4 and 5 need not be present in all bursts.

1. An initial **steep decay phase** immediately follows the prompt emission and causes a rapid drop in flux. It was thought to be most likely due to off-axis, high-latitude emission from regions $\theta > \Gamma^{-1}$ known as the curvature effect (where θ is the jet opening angle; Kumar & Panaitescu 2000; Dermer 2004; Panaitescu et al. 2006; Willingale et al. 2010). After the line-of-sight gamma-rays have ceased, the off-axis emission is smaller and arrives later. This corresponds to an observed flux decreasing as $F_\nu \propto t^{-2}$. Hence, the steep decay would be delayed prompt emission with a spectrum Doppler softened into the X-ray band. However, the spectral and temporal indices do not follow the correlation predicted by this

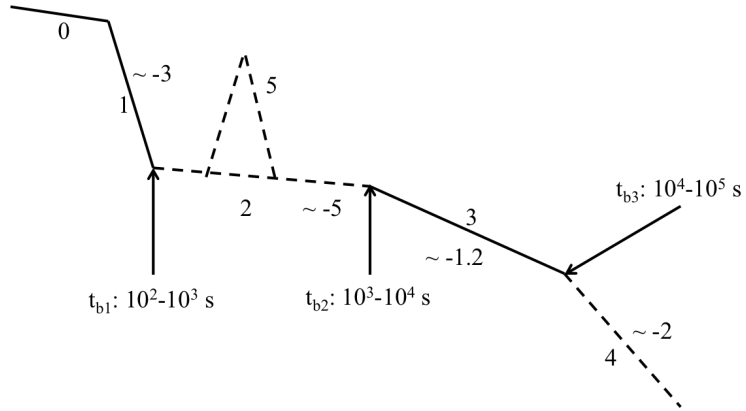


Figure 1.5: The ‘canonical’ X-ray afterglow as shown in Zhang et al. (2006). Phase 0 depicts the prompt emission and phases 1, 2, 3, 4 and 5 depict the steep decay, shallow decay, normal decay, jet breaks and flares, respectively. Phases 1 and 3 are most common and are therefore represented by solid lines. Typical temporal indices of the four segments are shown along with rough estimates of break times (t_b).

model, making a combination of the curvature effect and afterglow the most likely origin of the early steep decay.

2. A **shallow decay phase** follows stage 1, so-called because the temporal index is too shallow to be consistent with the predicted deceleration of the forward shock in the circumburst material by the fireball model. It is motivation for continuous energy injection from late-time central engine activity. Sections of outflow with a low Γ arrive at later times and refresh the forward shock, hence flattening light curves for hours and as long as days. It is often cited in favour of the magnetar model (Fan & Xu, 2006; Rowlinson et al., 2010, 2013) and is referred to as a ‘plateau’.
3. A **normal decay phase**, which unlike stages 1 and 2 was observed in the pre-*Swift* era, follows stage 2. It is consistent with a decelerating shock in the slow cooling regime (Zhang et al., 2006).
4. In some GRBs, an achromatic steepening or **jet break** is observed, which is interpreted as being the drop in flux associated with the beaming angle becoming larger than the physical opening angle of the jet. This reveals the jetted structure of the emission to the observer for the first time, as discussed in Section 1.4.1.

5. **Flares** are observed in approximately half of the GRB afterglows observed by *Swift* (Swenson & Roming, 2014). They are increases in flux up to a factor ~ 500 above the smooth afterglow continuum (*e.g.*, GRB 050502B) and are often characterised by fast-rise, exponential-decay pulse shapes comparable to the prompt emission (though there are some exceptions, *e.g.*, GRB 050502B). Current theories attribute them to similar central engine activity that produced the prompt emission (Burrows et al., 2005a; Falcone et al., 2006; Curran et al., 2008; Chincarini et al., 2010; Margutti et al., 2011; Sonbas et al., 2013) since the energy budget and fast-rise, exponential-decay profile are more easily satisfied and their spectra are very similar.

1.4.5 Central Engines

GRBs have large energy demands and strict compactness criteria which severely restricts the range of potential candidates for the central engine. Candidates must be compact, have a large reservoir of energy, and have the capability of launching relativistic jets with Lorentz factors of at least ~ 100 . Within these requirements, the two most popular central engine candidates are accreting black holes or highly magnetized, rapidly rotating neutron stars (known as magnetars), both of which can be produced within the collapsar model (LGRBs; Popham et al. 1999; Dessart et al. 2008; Metzger et al. 2011) or a compact object binary merger scenario (SGRBs; Rosswog et al. 2003; Giacomazzo & Perna 2013).

Black Holes

The collapse of a super massive star (*i.e.*, a collapsar; MacFadyen & Woosley 1999) into a black hole, the mergers of stellar mass black holes and neutron stars or neutron star binary systems often lead to a GRB that has a black hole of several solar masses operating as its central engine. The resultant black hole also often has an accretion disc of mass $0.01 - 1M_{\odot}$ (Woosley, 1993; Popham et al., 1999). The GRB jets are launched through magnetic processes, e^{\pm} annihilation, or neutrino interactions (Paczynski, 1991; Narayan et al., 1992; Katz, 1997; MacFadyen & Woosley, 1999;

Rosswog et al., 2003; Lei et al., 2013). The advantages of the black hole central engine scenario are that the rates of black hole-neutron star and neutron star binary mergers are consistent with the GRB rates (Narayan et al., 1991; Phinney, 1991) and a black hole provides a low-baryon environment which does not impede a relativistic jet. However, the black hole central engine doesn't offer a natural explanation for the late-time flattening observed in the light curves (Rowlinson et al., 2013).

Magnetars

A magnetar cannot be formed with black hole involvement and so they have a limited selection of progenitor options. The most common progenitor would be a neutron star binary merger (Rosswog et al., 2003; Belczynski et al., 2006); though a collapsar, white dwarf binary mergers and the accretion induced collapse of a white dwarf are also probable progenitor scenarios (Chapman et al., 2007; Metzger et al., 2008). The merger produces a hyper-massive neutron star with an initial spin period of a few milliseconds and an intense magnetic field of the order of $\sim 10^{15}$ G. The great success of the magnetar model is its ability to explain X-ray plateaux stemming from extra energy tapped from the dipole spin-down and injected into the fireball (Usov, 1992; Zhang & Mészáros, 2001; Metzger et al., 2011; Rowlinson et al., 2013). However, the model's main weakness is the prompt emission. A magnetar would not clear its surroundings as efficiently as a black hole and the environment would therefore be baryon-rich, hence reducing the bulk Lorentz factor of a relativistic jet (Drenkhahn & Spruit, 2002; Dessart et al., 2007). The magnetar is expected to be spun down very rapidly during the prompt emission and the available energy from a magnetar is strictly limited by the rotational energy. Hence GRBs with beam-corrected energies exceeding a few 10^{52} erg would be inconsistent with the magnetar central engine model. The available kinetic energy is approximated as:

$$E_{\text{total}} \sim 10^{52} \left(\frac{P}{1 \text{ ms}} \right)^{-2} \text{ erg} \quad (1.2)$$

where P is the spin period of the magnetar in milliseconds.

1.5 Magnetars

Evidence for magnetars within the Milky Way stems from observations of soft gamma repeaters (Norris et al., 1991). The spectral hardness and extreme luminosities of these events implies and magnetic field of the order $\sim 10^{15}$ G (Thompson & Duncan, 1995).

1.5.1 Neutron Stars

Neutron stars can be created during core-collapse supernovae, white dwarf binary mergers or via the accretion induced collapse of a white dwarf. The known mass range for neutron stars varies between $1.25 - 2.01M_{\odot}$ (Miller & Miller, 2015). The equation of state of neutron stars is an important concept that determines the compressibility of the neutron star material. A ‘soft’ equation of state implies a compressible composition and this will diminish the maximum mass of a neutron star before further collapse into a black hole. In order to form a magnetar from a neutron star binary merger and avoid collapse to a black hole (at least temporarily), the equation of state needs to be ‘rigid’. The parent neutron stars of such a merger would likely have individual masses $\sim 1.4M_{\odot}$ and would produce a remnant of mass $\sim 2M_{\odot}$. Such high neutron star masses have been confirmed using Shapiro delay measurements (Shapiro, 1964). Since magnetars would be born with rapid rotation rates, they would also be supported against further collapse by the rotational energy, at least initially.

1.5.2 Field Amplification

Magnetars possess the strongest magnetic fields in the Universe with surface dipolar fields on the order $\sim 10^{14} - 10^{15}$ G (Hurley et al., 2005; Palmer et al., 2005). There are many theories on how these fields are created. The most popular ones are an $\alpha - \Omega$ dynamo (Duncan & Thompson, 1992; Thompson & Duncan, 1993), shear instabilities during the merger (Price & Rosswog, 2006), and magneto-rotational instabilities during core collapse (Akiyama et al., 2003; Thompson et al.,

2005).

1.6 This Thesis

Over the course of this thesis, I aim to understand the mechanisms available to a magnetar as a central engine, specifically the propeller mechanism which utilises magneto-centrifugal slinging to eject accreting material from the system producing emission through shocks. I will then ascertain whether this mechanism is an energetically viable candidate for the most energetically and morphologically challenging subtypes of GRBs, including SGRBs with extended emission and LGRBs with giant X-ray flares. I will attempt to overcome the inherent weaknesses of the magnetar model, *i.e.*, a restricted rotational energy reservoir and rapid spin down at early times, by incorporating a fallback accretion component, which will increase the global energy budget and allow the magnetar to be spun back up, thereby refreshing the rotational energy reservoir.

Chapter 2 introduces the theoretical framework used to model fallback accretion within the magnetar model and tests this against previous work before going on to develop and test a Markov chain Monte Carlo fitting routine. Chapter 3 discusses the results of fitting the magnetar propeller model with fallback accretion to a sample of SGRBs exhibiting extended emission and Chapter 4 applies to model to LGRBs exhibiting giant X-ray flares. I summarise my key conclusions in Chapter 5 and outline the motivation and methodology for future works.

2

The Magnetar Propeller Model with Fallback Accretion

The work presented in this chapter was partially published in Gibson et al. (2017).

Abstract

I present the propeller model of a magnetar and accretion disc system which I have modified to include late-time fallback accretion. The fallback timescale and the global mass budget for fallback have been parameterised in terms of the viscous timescale and the initial mass of the disc respectively. An ordinary differential equation integrator has been used to return values of the disc mass, M_D , and angular frequency, ω , for a given time period. I show that the modifications are capable of reproducing the phenomenological classes found in earlier models (Gompertz et al., 2014) and explore the parameter space of the model. I then develop a Markov chain Monte Carlo simulation to optimise this model for a sample of synthetic light curves.

2.1 Introduction

The magnetar model involves the extraction of spin energy from a rapidly rotating, highly magnetised neutron star (magnetar) via interactions between its intense dipole field and a circumstellar environment (Zhang & Mészáros, 2001). This can happen through phenomena such as the Blandford-Znajek mechanism (Blandford & Znajek, 1977) or magnetic propeller (Piro & Ott, 2011; Gompertz et al., 2014). Magnetic propeller involves the expulsion of mass from a magnetar-accretion disc system due to the centrifugal barrier formed by the rapidly rotating, intense magnetic field. Some rotational energy is removed from the magnetar by the escaping material.

The birth and early-time spin down of magnetars has been suggested as a progenitor for GRBs for both long (Zhang & Mészáros, 2001; Troja et al., 2007; Lyons et al., 2010; Dall’Osso et al., 2011; Metzger et al., 2011) and short types (Fan & Xu, 2006; Rowlinson et al., 2010, 2013). This model is a concept that is competing with black holes as the source of power in GRBs, mainly due to its potential as a naturally long-lived central engine (see Bernardini 2015 for a review). The magnetar model has been used to explain plateaux in GRB afterglows (Rowlinson et al., 2013; Gompertz et al., 2013), extended emission in SGRBs (Gompertz et al., 2014), and also provides

a favourable candidate for the source of flares in the afterglows of all GRBs since the contained energy and timescales of flares are naturally satisfied by a compact object central engine. Also the superposition of flares onto a background continuum indicate that they do not originate from the same emission site as the afterglow (Chincarini et al., 2010). However, there are some issues with the magnetar model as a GRB central engine since there is a strict energy upper limit imposed by the rotational energy reservoir of the neutron star which is typically taken to be $\approx 3 \times 10^{52}$ erg for a $1.4 M_{\odot}$ neutron star with a 1 ms spin period. Also, the magnetar is expected to be spun down very rapidly during the prompt emission phases, thereby further limiting the amount of available energy.

In both collapsars and compact object binary mergers, remaining material is expected to be available for fallback accretion and therefore is an important mechanism to include in GRB models. In collapsars, fallback material would arise from stripped envelopes of massive stars before they explode. Alternatively as compact objects spiral inwards, simulations suggest that some material is ejected by tidal disruption into a tidal tail through the outer Lagrange point and the resulting fallback mass could potentially be up to $0.1 M_{\odot}$ (Rosswog, 2007; Lee et al., 2009). Adding a fallback mechanism into the model augments the magnetar energy budget, as it provides a mechanism to spin the magnetar back up.

The theory of the model is presented in Section 2.2. A comparison of dipole torque equations is performed in Section 2.3. An exploration of parameter space is performed in Section 2.4, including classifying the burst morphologies and comparing these morphologies to previous work. Finally, the Markov chain Monte Carlo optimisation routine is described and tested on synthetic light curves in Section 2.5.

2.2 The Magnetic Propeller Model

The magnetic dipole moment for a magnetar with a dipole field strength B and radius R is given by $\mu = BR$ and the magnetic field can then be described as $B = \mu/r^3$. This leads to a magnetic

pressure for a given radius, r , as follows.

$$P_{\text{mag}} = \frac{\mu^2}{8\pi r^6} \quad (2.1)$$

P_{mag} is opposed by a ram pressure, exerted by material falling in from the accretion disc, given by

$$P_{\text{ram}} = \frac{\dot{M}}{4\pi} \left(\frac{2GM_*}{r^5} \right)^{\frac{1}{2}} \quad (2.2)$$

where M_* is the mass of the magnetar. The radius at which these two pressures are equal is one of the two key radii that determines the behaviour of the magnetar. This is the Alfvén radius, r_m , and is the radius at which the dynamics of the gas within the disc is strongly influenced by the magnetic field (see Appendix A for derivation). It is given by

$$r_m \simeq \mu^{\frac{4}{7}} (GM_*)^{-\frac{1}{7}} \dot{M}^{-\frac{2}{7}} \quad (2.3)$$

where $\dot{M} = M_D(t)/t_\nu$. $M_D(t)$ is the evolution of the disc mass with time and $t_\nu = R_D/\alpha c_s$ is the timescale for mass flowing through a viscous disc (R_D is the disc radius, c_s is the sound speed in the disc, and α is a viscosity prescription). The other key radius is the co-rotation radius, r_c , at which material orbits the magnetar at the same rate as the stellar surface

$$r_c = \left(\frac{GM_*}{\omega^2} \right)^{\frac{1}{3}} \quad (2.4)$$

where $\omega = 2\pi/P$ is the angular frequency of the magnetar and P is the spin period. Two regimes of magnetar behaviour are then defined by comparing Equations (2.3) and (2.4). If $r_c > r_m$, the accretion disc is rotating more rapidly than the magnetic field (assuming the field rotates rigidly with the magnetar surface) and the effect of this is to slow the in falling material down and allow it to accrete. In this case, the magnetar gains angular momentum and spins up, hence the rotation of the field increases. Conversely if $r_c < r_m$, the magnetic field is rotating faster than the material and the result is that particles are accelerated to super-Keplerian velocities and ejected from the system. The magnetar loses angular momentum to the ejected material and its rotation is slowed. This condition is the propeller regime. To prevent the ejecta from exceeding the speed of light, r_m is capped at some fraction, k , of the light cylinder radius, r_{lc} . At $r_{lc} = c/\omega$, the magnetic field lines must orbit at the speed of light in order to maintain a rigid rotation with the magnetar surface.

The propeller and accretion regimes both have an effect on the angular frequency of the magnetar by exerting a torque. If $r_m > R$ (where R is the radius of the magnetar), an accretion torque can be defined as

$$\tau_{\text{acc}} = (GM_* r_m)^{\frac{1}{2}} \left(\dot{M}_{\text{acc}} - \dot{M}_{\text{prop}} \right) \quad (2.5)$$

If $r_m < R$, the accretion torque becomes

$$\tau_{\text{acc}} = (GM_* R)^{\frac{1}{2}} \left(\dot{M}_{\text{acc}} - \dot{M}_{\text{prop}} \right) \quad (2.6)$$

τ_{acc} will spin the magnetar up when $r_c > r_m$, but becomes negative and spins the magnetar down when $r_c < r_m$ to account for the loss of angular momentum to the ejected material. In Equations (2.5) and (2.6), \dot{M}_{prop} is the flow of ejected mass, given by

$$\dot{M}_{\text{prop}} = \eta_2 \frac{M_{\text{D}}(t)}{t_\nu} \quad (2.7)$$

and \dot{M}_{acc} is the accretion rate onto the magnetar, given by

$$\dot{M}_{\text{acc}} = (1 - \eta_2) \frac{M_{\text{D}}(t)}{t_\nu} \quad (2.8)$$

where η_2 is the efficiency of the propeller mechanism which I define as

$$\eta_2 = \frac{1}{2} \left(1 + \tanh [n(\Omega - 1)] \right) \quad (2.9)$$

This definition of η_2 allows accretion to be turned off at a variable rate as the propeller switches on and the combined efficiency of these mechanisms can never exceed 100%. In Equation (2.9), Ω is the ‘fastness parameter’, $\Omega = \omega / (GM_* / r_m^3)^{1/2} = (r_m / r_c)^{3/2}$, which switches the propeller on as $\Omega \rightarrow 1$, and n controls how “sharp” the propeller switch-on is, as demonstrated in Fig. 2.1.

The dipole spin-down, τ_{dip} , is the final contributing factor to the torque and is given by

$$\tau_{\text{dip}} = -\frac{\mu^2 \omega^3}{6c^3} \quad (2.10)$$

The negative sign indicates that τ_{dip} spins the magnetar down and produces dipole emission. From these torques, the rate of change of the spin can be calculated from

$$\dot{\omega} = \frac{\tau_{\text{acc}} + \tau_{\text{dip}}}{I} \quad (2.11)$$

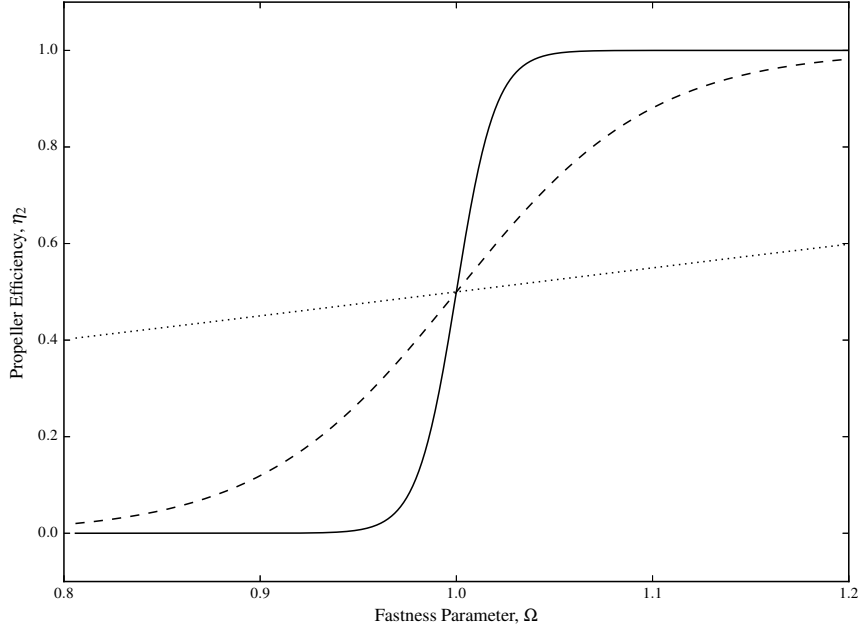


Figure 2.1: A demonstration of how quickly the propeller becomes active as a function of n . The dotted line corresponds to $n = 1$, the dashed line corresponds to $n = 10$, and the solid line corresponds to $n = 100$.

where $I = \frac{4}{5}M_*R^2$ is the moment of inertia of the magnetar.

As the spin rate changes, the rotation parameter, β , must be monitored. For $\beta > 0.27$, a dynamical bar-mode instability becomes important and will radiate or hydro-dynamically readjust the angular momentum. In this case, the accretion torque will be set to zero, $\tau_{\text{acc}} = 0$, and the magnetar allowed to spin down until the instabilities subside. The rotation parameter is defined as $\beta = \frac{T}{|W|}$, where $T = \frac{1}{2}I\omega^2$ is the rotational energy and $|W|$ is the binding energy. As in Piro & Ott (2011), following the prescription from Lattimer & Prakash (2001), $|W|$ is given by

$$|W| \approx 0.6M_*c^2 \frac{GM_*/Rc^2}{1 - 0.5(GM/Rc^2)} \quad (2.12)$$

I assume an accretion disc with a surrounding global mass budget available to fallback onto the outer radius of the disc on a ballistic timescale of $t^{-\frac{5}{3}}$. I have parameterised the available fallback mass as a fraction (δ) of the initial disc mass, $M_{\text{fb}} = \delta M_{\text{D},i}$, and the fallback timescale is similarly parameterised as a fraction (ϵ) of the viscous timescale, $t_{\text{fb}} = \epsilon t_\nu$. Hence, the fallback mass flow

is defined as

$$\dot{M}_{\text{fb}} = \frac{M_{\text{fb}}}{t_{\text{fb}}} \left(\frac{t + t_{\text{fb}}}{t_{\text{fb}}} \right)^{-\frac{5}{3}} \quad (2.13)$$

Collecting together Equations (2.7), (2.8) and (2.13) defines a total mass flow rate through the disc

$$\dot{M}_{\text{D}} = \dot{M}_{\text{fb}} - \dot{M}_{\text{prop}} - \dot{M}_{\text{acc}} \quad (2.14)$$

which accounts for mass added to the disc through fallback accretion (\dot{M}_{fb}) and mass lost from the disc via accretion onto the magnetar or the propeller mechanism (\dot{M}_{acc} and \dot{M}_{prop} , respectively).

The critical equations here are Equations (2.11) and (2.14) since these are coupled, first order, ordinary differential equations (ODEs) and the values of $M_{\text{D}}(t)$ and $\omega(t)$ can be calculated using an ODE integrator for a given time period. The model was written in *Python* and made use of the *lsoda* ODE solver from *ODEPACK* (Hindmarsh, 1983).

Fig. 2.2 demonstrates how these fallback parameters affect the disc mass and angular frequency of a magnetar and disc system and how the propeller condition $r_{\text{m}}/r_{\text{c}}$ evolves with time. For short timescales and small fallback masses ($\epsilon = 1$ and $\delta = 1$; solid, red curve), the magnetar spins up more slowly despite rapid fallback because the disc is only being fed small amounts of mass. Hence, the propeller mechanism turns on earlier since the propeller condition is at a lower frequency. For short timescales and large fallback masses ($\epsilon = 1$ and $\delta = 10$; dashed, red curve), mass is quickly added to the disc and the magnetar spins up rapidly. The propeller mechanism is turned on later because the conditional frequency is higher. For long timescales and small fallback masses ($\epsilon = 10$ and $\delta = 1$; solid, green curve), the disc is fed a small amount of mass very slowly and so the magnetar spins up gradually. Again, the propeller condition is at a lower frequency and therefore the mechanism turns on earlier. For long timescales and large fallback masses ($\epsilon = 10$ and $\delta = 10$; dashed, green curve), the disc mass stays constant over a longer period providing a gentle spin-up of the magnetar. Again, the propeller condition is at a higher frequency and the mechanism turns on later. Generally speaking, an initially denser disc makes the propeller mechanism harder to initiate, but the magnetar is spun up more rapidly and therefore satisfies the propeller condition at an earlier time.

The terms are collected together to estimate the luminosities from the dipole and propellered

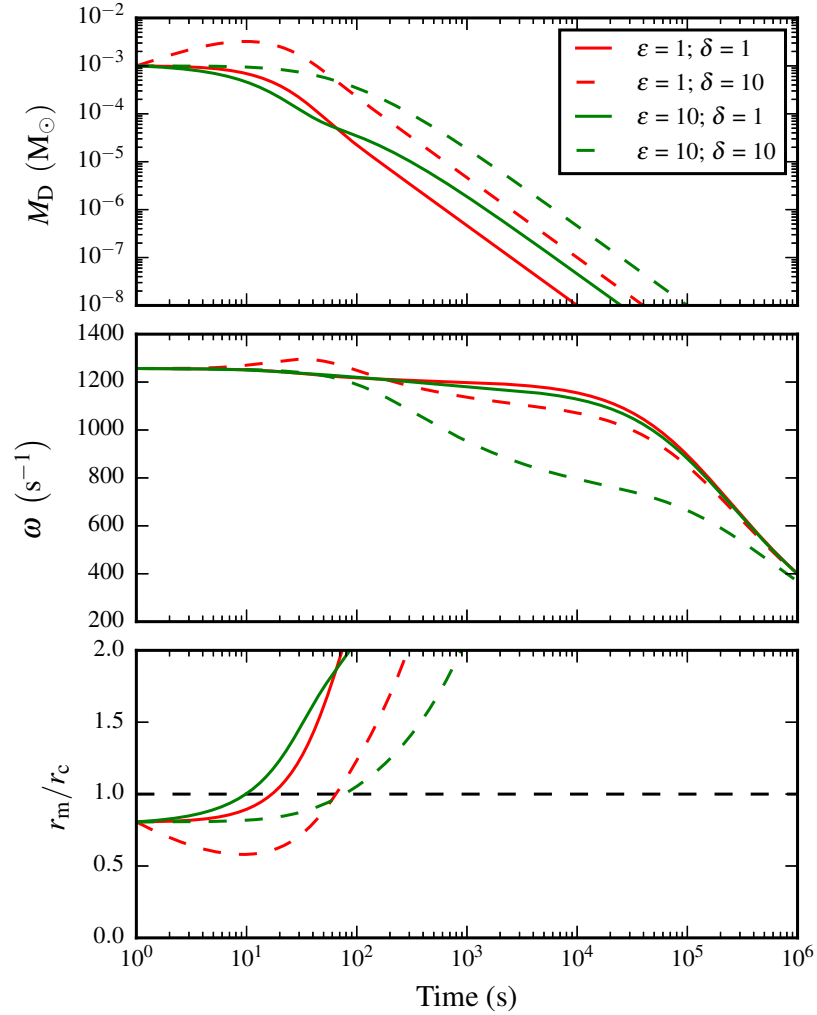


Figure 2.2: A demonstration of how different combinations of the fallback parameters ϵ and δ affect the disc mass (top panel) and angular frequency (centre panel) of a magnetar and disc system with fixed magnetic field, initial spin period, initial disc mass and radius. The bottom panel shows the evolution of the propeller condition r_m/r_c over time for each combination. The system is in the propeller regime when $r_m/r_c > 1$ (*i.e.*, above the black, dashed line).

components, such that

$$L_{\text{prop}} = -\tau_{\text{acc}}\omega \quad (2.15)$$

and

$$L_{\text{dip}} = -\tau_{\text{dip}}\omega \quad (2.16)$$

Equation (2.15) is an estimate of the kinetic luminosity of the propellered material and is negative to account for the negative sign of τ_{acc} when the magnetar is spinning down. With Equation (2.15), expulsion of the material is implicitly assumed to originate from the inner radius of the disc. The total luminosity is given by the sum of the dipole and propeller luminosities and their relative efficiencies, then multiplied by a beaming fraction to account for the relativistic beaming of the jet

$$L_{\text{tot}} = \frac{1}{f_{\text{B}}} (\eta_{\text{dip}}L_{\text{dip}} + \eta_{\text{prop}}L_{\text{prop}}) \quad (2.17)$$

where η_{prop} and η_{dip} are the propeller and dipole energy-luminosity conversion efficiencies respectively and $1/f_{\text{B}}$ is the fraction of the stellar sphere which is emitting and is related to the half-opening angle of the jet, θ_{j} , as $f_{\text{B}} = 1 - \cos(\theta_{\text{j}})$ (Rhoads, 1999; Sari et al., 1999).

2.2.1 Expelling Material from the Gravitational Potential Well of the Magnetar

In previous work, an extra term was added to the propeller luminosity equation so that it took the form:

$$L_{\text{prop}} = -\tau_{\text{acc}}\omega - \frac{GM_*}{r_{\text{m}}} \frac{M_{\text{D}}}{t_{\nu}} \eta_2 \quad (2.18)$$

where the second term accounts for the gravitational potential well the expelled material must climb out of before emission can be produced (Gompertz et al., 2014). In the following body of work, I have chosen not to explicitly remove the energy associated with this escaping material for two reasons: (i) it is trivial to show that the energy relating to the gravitational potential well can be adapted into a modified version of the propeller efficiency parameter η_{prop} , and (ii) explicitly removing the escape energy excludes models where the magnetar injects angular momentum into the accretion flow at r_{m} while viscous torques redistribute this to expand the disc, maximising the

energy available for conversion into electromagnetic radiation at the central engine site. The two approaches are mathematically equivalent which I will show through the following derivations.

Using Equations (2.7), (2.8), (2.13), (2.14) and the relation $\eta_1 = 1 - \eta_2$, a torque equation can be defined in terms of the accretion, propelling and dipole components (assuming $\dot{M}_{\text{acc}} = \dot{M}_{\text{prop}} = \frac{M_{\text{D}}}{t_{\nu}}$) as follows.

$$\begin{aligned}
\tau &= \tau_{\text{acc}} - \tau_{\text{prop}} - \tau_{\text{dip}} \\
&= \frac{M_{\text{D}}}{t_{\nu}} (GM_* r_{\text{m}})^{\frac{1}{2}} \eta_1 - \frac{M_{\text{D}}}{t_{\nu}} (GM_* r_{\text{m}})^{\frac{1}{2}} \eta_2 - \tau_{\text{dip}} \\
&= \frac{M_{\text{D}}}{t_{\nu}} (GM_* r_{\text{m}})^{\frac{1}{2}} (\eta_1 - \eta_2) - \tau_{\text{dip}} \\
&= \frac{M_{\text{D}}}{t_{\nu}} (GM_* r_{\text{m}})^{\frac{1}{2}} (1 - 2\eta_2) - \tau_{\text{dip}} \\
&= I\dot{\omega}
\end{aligned} \tag{2.19}$$

The spin down power of the magnetar is defined as

$$P = -\omega\tau = -I\omega\dot{\omega} \tag{2.20}$$

and the electromagnetic luminosity is defined as some fraction, f , of the spin down power

$$\begin{aligned}
L_{\text{EM}} &= -fP \\
&= -\omega \left[\frac{M_{\text{D}}}{t_{\nu}} (GM_* r_{\text{m}})^{\frac{1}{2}} (1 - 2\eta_2) \eta_{\text{prop}} + \eta_{\text{dip}} \tau_{\text{dip}} \right] \\
&= \eta_{\text{prop}} L_{\text{prop}} + \eta_{\text{dip}} L_{\text{dip}}
\end{aligned} \tag{2.21}$$

During spin up phases (*i.e.*, when the net effect of the accretion and propeller torques is positive), I set L_{prop} to zero.

The electromagnetic luminosity accounting for the gravitational potential well of the magnetar is now defined as follows.

$$L_{\text{EM}} = -\omega \frac{M_{\text{D}}}{t_{\nu}} (GM_* r_{\text{m}})^{\frac{1}{2}} (1 - 2\eta_2) \eta'_{\text{prop}} - \frac{GM_*}{r_{\text{m}}} \frac{M_{\text{D}}}{t_{\nu}} \eta_2 - \eta_{\text{dip}} \tau_{\text{dip}} \omega \tag{2.22}$$

where η'_{prop} is equivalent to the propeller efficiency parameter used in previous work (*e.g.*, Gompertz et al. 2014).

Since $\omega = \left(\frac{GM}{r^3}\right)^{\frac{1}{2}}$ then $\omega(GMr_m)^{\frac{1}{2}} = \frac{GM}{r_m}$ and Equation (2.22) can be rewritten as

$$\begin{aligned} L_{\text{EM}} &= -\omega \frac{M_{\text{D}}}{t_{\nu}} (GMr_m)^{\frac{1}{2}} (1 - 2\eta_2) \eta'_{\text{prop}} - \omega \frac{M_{\text{D}}}{t_{\nu}} (GMr_m)^{\frac{1}{2}} \eta_2 - \eta_{\text{dip}} \tau_{\text{dip}} \omega \\ \therefore L_{\text{EM}} &= -\omega \frac{M_{\text{D}}}{t_{\nu}} (GMr_m)^{\frac{1}{2}} \left[(1 - 2\eta_2) \eta'_{\text{prop}} - \eta_2 \right] - \eta_{\text{dip}} \tau_{\text{dip}} \omega \end{aligned} \quad (2.23)$$

Assuming the material is fully ejected from the system, it can be shown that

$$(1 - 2\eta_2) \eta'_{\text{prop}} - \eta_2 = (1 - 2\eta_2) \eta_{\text{prop}}$$

and hence the relation between the modified (η_{prop}) and unmodified (η'_{prop}) propeller efficiency parameters is given by

$$\eta'_{\text{prop}} = \eta_{\text{prop}} + \frac{\eta_2}{(1 - 2\eta_2)} \quad (2.24)$$

When $\eta_2 = 0$, these two cases are equivalent but the propeller mechanism is not activated. At maximum propelling or $\eta_2 = 1$, there is an extra term of $-\frac{1}{2}$ and η_{prop} would have to be capped at 50% when assuming everything escapes as electromagnetic radiation in this case. All the results presented forthwith use η_{prop} , not η'_{prop} .

2.3 Comparing Dipole Torque Equations

In Section 2.2, I have used Equation (2.10) for the dipole torque, which is the classical solution experienced by any rotating, magnetised body (Shapiro & Teukolsky, 1983) and I follow Piro & Ott (2011) in implementing this. However, work done by Gompertz et al. (2014) instead uses the following form for the dipole torque

$$\tau_{\text{dip}} = -\frac{2}{3} \frac{\mu^2 \omega^3}{c^3} \left(\frac{r_{\text{lc}}}{r_m} \right)^3 \quad (2.25)$$

which is Equation (2) in Bucciantini et al. (2006).

Bucciantini et al. (2006) use a relativistic magneto-hydrodynamic treatment to solve for the plasma winds emanating from a rotating NS and accretion disc system. They assume that the flow emerges from open flux tubes (providing the extent and shape of the open field line region in the magnetic

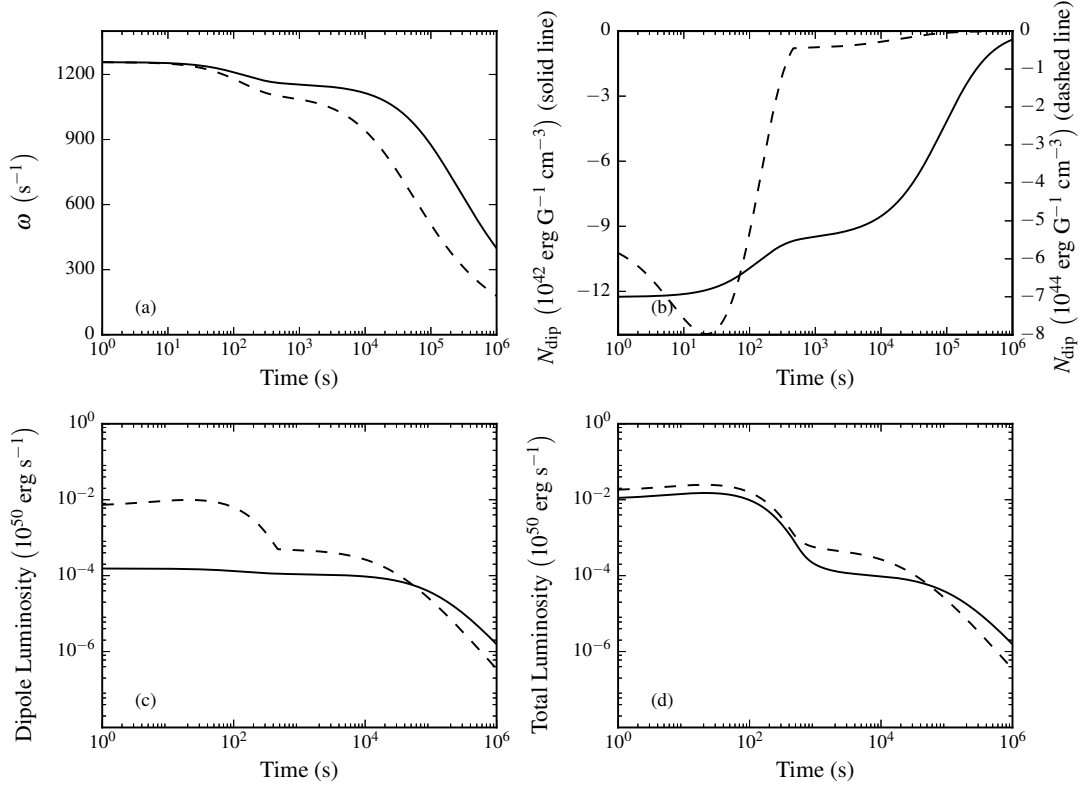


Figure 2.3: A comparison of how Equation (2.10) (solid line; Piro & Ott 2011) and Equation (2.25) (dashed line; Bucciantini et al. 2006) affect (a) the stellar spin; (b) the dipole torque (note the dual y axes); (c) the dipole luminosity; and (d) the total luminosity of a synthetic GRB X-ray light curve.

field is known) and that a truncation of the disc produces more open flux tubes and therefore a greater mass loss. Equation (2.25) is then derived from these assumptions. However, I cannot be certain that these assumptions apply within the model presented in this work and I do not present a full magneto-hydrodynamic treatment of the magnetic propeller. Therefore, I chose to use Equation (2.10) rather than introduce uncertain assumptions into the model. A comparison between Equations (2.10) and (2.25) is shown in Fig. 2.3 using a synthetic GRB X-ray light curve with arbitrary parameters.

Table 2.1: The values used to test the effect of parameter variation on the shape of an X-ray light curve. The total number of combinations resulted in 129, 600 synthetic light curves. B - magnetic field; P_i - initial spin period; $M_{D,i}$ - initial disc mass; R_D - disc radius; ϵ - timescale ratio; δ - fraction of initial disc mass available in the global mass budget; n - sharpness of propeller “switch-on”; α - viscosity prescription for the disc; c_s - sound speed in the disc; k - capping fraction of r_m to r_{lc} .

B	($\times 10^{15}$ G)	1	5	10	50	-
P_i	(ms)	1	5	10	-	-
$M_{D,i}$	(M_\odot)	10^{-5}	10^{-4}	10^{-3}	10^{-2}	10^{-1}
R_D	(km)	100	500	1000	-	-
ϵ		1	10	-	-	-
δ		1	10	-	-	-
n		1	10	50	-	-
α		0.1	0.2	0.3	0.4	0.5
c_s	(10^7 cm s $^{-1}$)	1	2	3	-	-
k		0.90	0.95	0.99	-	-

2.4 Exploring Parameter Space

To determine how the modifications to the propeller model have affected the phenomenological classes outlined in Gompertz et al. (2014), I repeated the parameter variation experiment they originally performed with values from Table 2.1. I fixed the magnetar mass and radius to be $1.4 M_\odot$ and 10 km respectively and set the propeller and dipole efficiencies to 100% and the beaming fraction to 1 since they only act to normalise the luminosity here. The total combination of parameters in Table 2.1 resulted in a sample of 97, 200 synthetic light curves.

2.4.1 Magnetar Properties

Initially, 2, 160 light curves were examined. They represented all combinations of B , P_i , $M_{D,i}$, R_D , ϵ , δ , and n with constant $\alpha = 0.1$, $c_s = 10^7$ cm s $^{-1}$, and $k = 0.90$. The four phenomenological

types originally outlined in Gompertz et al. (2014) were recovered and examples of each are shown in Fig. 2.4.

Type I - ‘Humped’ A ‘humped’ burst is initially powered only by dipole emission before the propeller is switched on after a delay. The hump in the light curve arises from the rapid increase in propeller luminosity. The propeller regime can be delayed like this because the accretion rate, \dot{M}_{acc} , is high and/or spin period, P_i , is low so that either $r_c > r_m$ holds true and the system is in the accretion regime, or the propellered material does not have enough energy to escape the potential well and hence falls back into the disc. Type I bursts are generated almost exclusively by relatively low magnetic fields (1×10^{15} G). Higher magnetic fields are only seen with longer initial spin periods (5 – 10 ms) since a stronger magnetic field compensates for the low spin rate to produce the propeller effect. 222 out of the 2,160 synthetic bursts (10.3%) are type I.

Type II - ‘Classic’ The ‘classic’ bursts exhibit a reasonably flat and well-defined propeller plateau which then transitions into a dipole plateau. Type II bursts are also almost exclusively generated by low magnetic fields (1×10^{15} G) but their initial spin periods are longer than types I bursts (5 – 10 ms). 132 of the 2,160 synthetic light curves (6.1%) are type II.

Type III - ‘Sloped’ ‘Sloped’ light curves result from approximately equal contributions from both emission components. They appear to act as one and produce a poorly-defined plateau. ‘Sloped’ bursts often have a single component look in their light curves. Type III bursts are the only type which include magnetic fields of 50×10^{15} G, suggesting such a high field makes the propeller effect indistinguishable from the dipole emission. 626 of the 2,160 synthetic bursts (29.0%) are type III.

Type IV - ‘Stuttering’ ‘Stuttering’ bursts are characterised by a brief period of propeller, followed by a dipole period before the propeller turns back on again, creating a hump. An example of this can be seen in the middle panel of the bottom row in Fig. 2.4 which shows a peaked

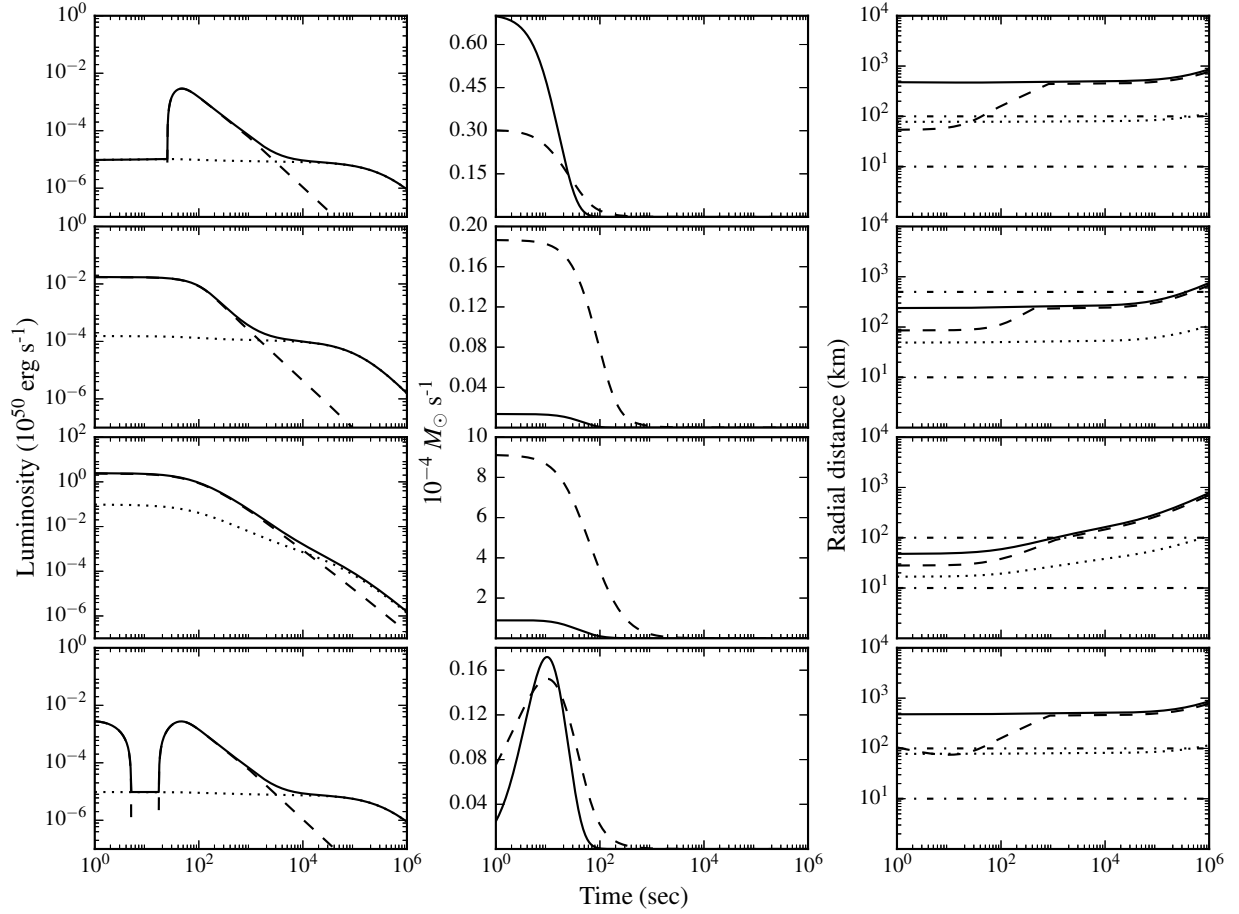


Figure 2.4: **Top to bottom:** Type I - ‘Humped’; Type II - ‘Classic’; Type III - ‘Sloped’; Type IV - ‘Stuttering’. Each row shows plots for one example of each class. They are not fully representative of the range of energetics or morphology for their respective classes since they are intended to highlight the light curve shapes only. **Left panels:** synthetic light curves representing the four phenomenological classes. Dotted line - dipole luminosity; dashed line - propeller luminosity; solid line - total luminosity. **Centre panels:** mass flow rates in the system. Solid line - mass flow rate on to the central magnetar; dashed line - propellered mass flow out of the system. **Right panels:** positions of key radii (in km) relative to the centre of the magnetar. Dashed line - Alfvén radius; dotted line - co-rotation radius; solid line - light cylinder radius. Lower horizontal dot-dashed line is the magnetar radius, upper horizontal dot-dashed line is the outer disc radius.

accretion event in the centre of the propelling regime. In this case, the magnetar is born in the propeller regime (like type II) but is rapidly spun down by the expelled mass. The accretion regime then begins, spinning the magnetar back up into the propeller regime and producing the second hump (like type I). ‘Stuttering’ bursts are formed almost exclusively through the combination of $B = 1 \times 10^{15}$ G, $\epsilon = 1$, and $\delta = 10$. 122 of the 2,160 synthetic bursts (5.7%) are type IV.

6 of the synthetic light curves were discarded due to a numerical failure of the ODE integrator (0.3%). A further 48.7% of light curves displayed other characteristics, such as sharp drop-offs, that were difficult to categorise into the four types. Some examples of these can be seen in the exploded plot for a type I burst shown in Fig. 2.5. Examples of the other types are presented in Figs. B.1, B.2 and B.3 in Appendix B. With these proportions in mind, a fitting routine will need a robust fitting statistic, the ability to sample a large amount of parameter space and be capable of recognising and dismissing local minima to be able to find an optimal fit. Since only type III bursts are generated when $B = 50 \times 10^{15}$ G, I will exclude the high end of the range for a fitting routine since this is not the type of burst I wish to model. All values for n appeared commonly in each type suggesting that the model is insensitive to n . Therefore, I will use a fixed value during fitting.

After this initial examination, the parameters α , c_s , and k were reintroduced as variables. As found in Gompertz et al. (2014), this did not introduce any new class types but instead introduced a greater range of burst shapes within each class. The effect of changing α and c_s was to reduce the delay before the onset of propelling by a few seconds, to sharpen the switch-on of the propeller, and a small increase in propeller peak luminosity in type I bursts. The effect of varying k was a slight increase in luminosity in the late-time dipole plateau due to there being more energy available. These effects are very slight so the parameters α , c_s , and k will be fixed to 0.1, 10^7 , and 0.90 respectively in fitting routines, to stay consistent with Gompertz et al. (2014).

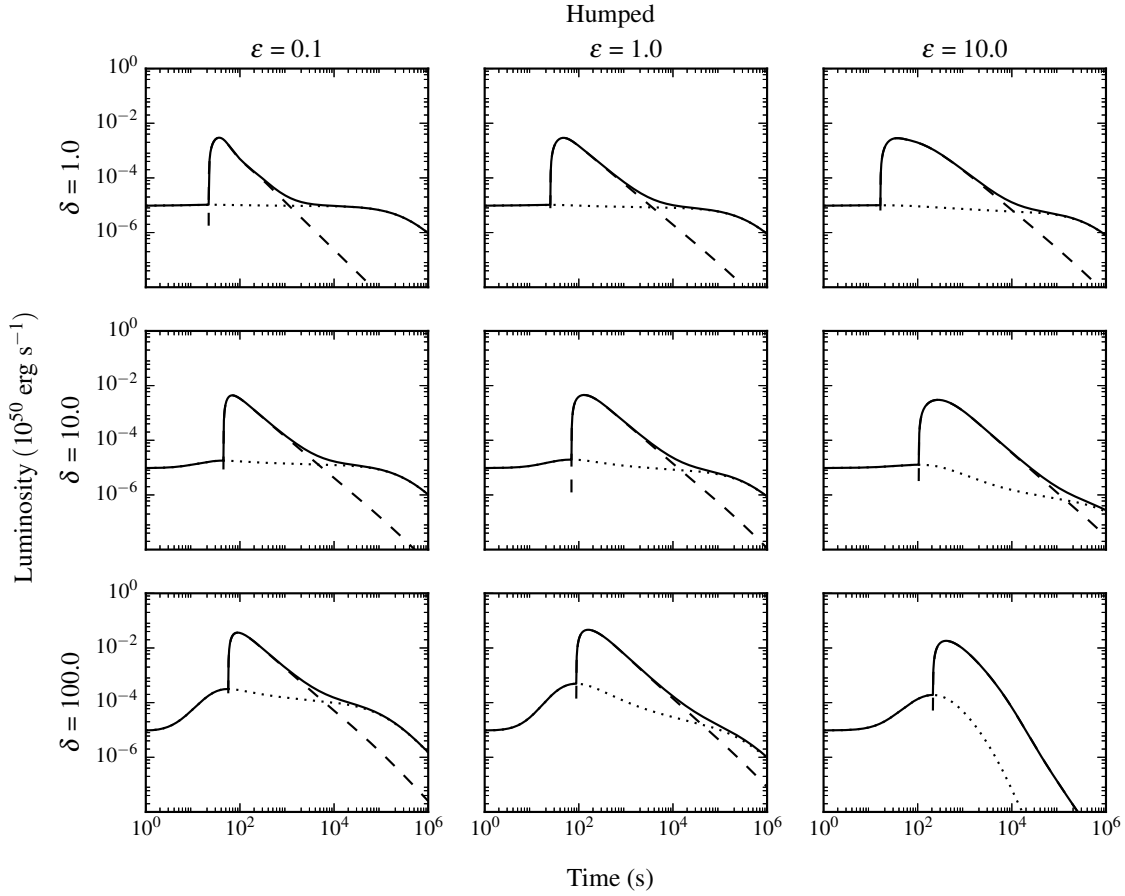


Figure 2.5: “Exploded” view of a ‘humped’ type burst (of arbitrary parameters) depicting how the fallback parameters effect the morphology of the burst. The fraction of the fallback timescale, ϵ , increases from left to right and the fraction of the fallback mass, δ , increases from top to bottom.

2.4.2 Comparing Types to Previous Work

In order to determine how well the modified model recovered the four types, I used the parameters given in Table 2.2 to generate light curves using the previous model described in Gompertz et al. (2014). The fallback accretion in the modified model was turned off by setting $\epsilon = 1$ and $\delta = 10^{-6}$, *i.e.*, the amount of fallback mass is so negligible that the magnetar behaves as if only the accretion disc is present and the fallback timescale becomes irrelevant. The value of n used was 1 as this is the closest approximation to the propeller switch-on modelled in Gompertz et al. (2014). Fig. 2.6 compares the modified model without fallback to the previous work. The difference in dipole luminosity between the two models is explained by my use of the classical dipole torque as

Table 2.2: The main parameters used to compare light curves from the previous model (Gompertz et al. 2014) with the modified model without fallback accretion.

		Humped	Classic	Sloped	Stuttering
B	($\times 10^{15}$ G)	1	1	10	5
P_i	(ms)	5	5	5	5
$M_{D,i}$	(M_\odot)	10^{-3}	10^{-4}	10^{-4}	10^{-2}
R_D	(km)	100	1000	1000	500

discussed in Section 2.3. However, the modified model does not recover the propeller luminosity and has produces type II light curves in all cases. Since it has already been shown in Fig. 2.4 that the modified model is capable of reproducing all types successfully, I would suggest that they have moved in parameter space due to the inclusion of \dot{M}_{prop} and its link to \dot{M}_{acc} through η_2 .

2.5 Preliminary Fitting

A Markov chain Monte Carlo simulation (MCMC; MacKay 2003, chap. 4) was used to optimise the model to data as there are a minimum of six parameters and the MCMC will efficiently search a large portion of parameter space (using an array of “walkers”) and increase the probability of finding the global minimum of the model. However, the MCMC method requires a burn-in phase which is loosely defined as an unknown number of steps at the beginning of the simulation where each “walker” attempts to find the lowest region of probability space. The chain is generally considered to be burned in when all walkers have converged onto this region of probability space. I implemented the *emcee* module, written for *Python*, to handle the MCMC (Foreman-Mackey et al., 2013). To construct the posterior probability distribution, a Gaussian log-likelihood function of the following form was chosen

$$\ln(p_{\text{likelihood}}) = \frac{1}{2} \sum_{i=1}^N \left(\frac{y_i - \hat{y}_i}{\sigma_i} \right)^2 \quad (2.26)$$

where y_i is a data point, σ_i is its associated uncertainty, and \hat{y}_i is a model point calculated at the same x -value as y_i . I chose a prior probability that is flat when the parameters are within the limits

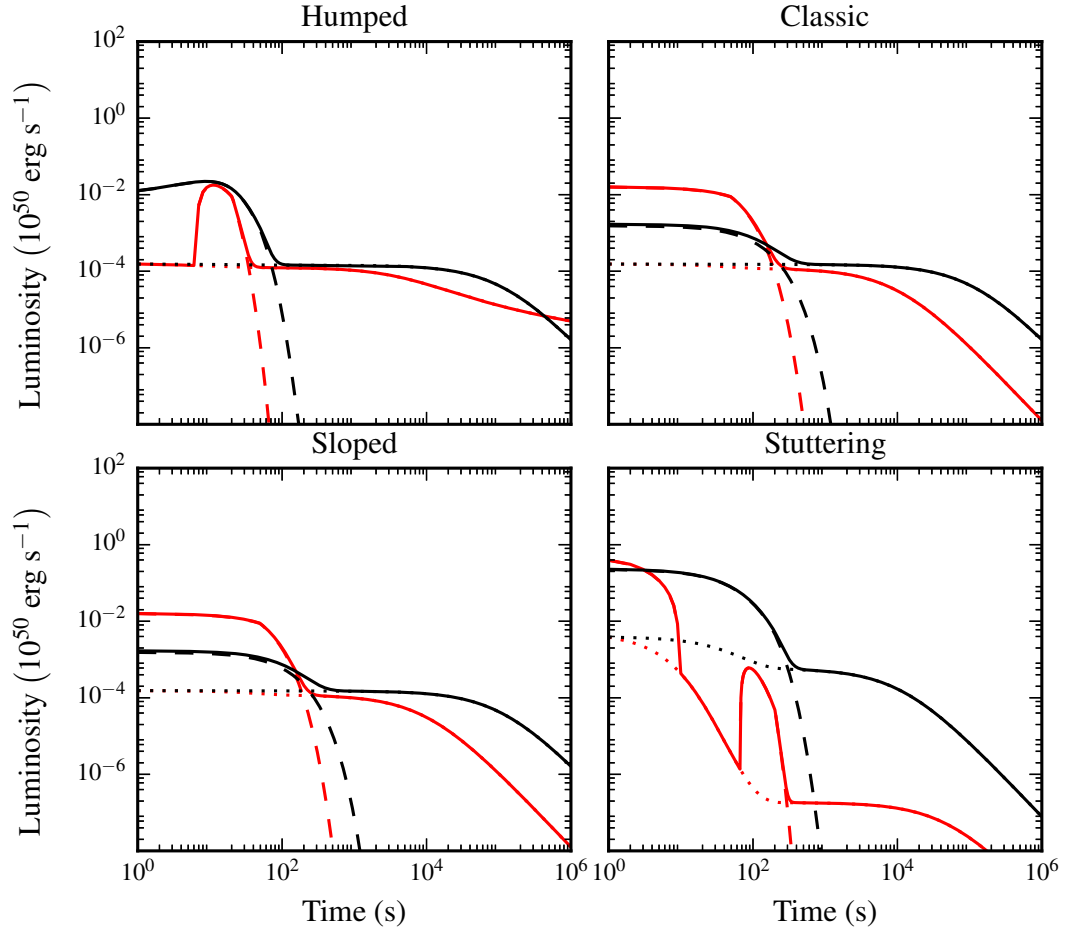


Figure 2.6: A comparison of light curves generated by the previous model (Gompertz et al. 2014; red curves) and the modified model without fallback accretion (black curves). The fallback was turned off by setting $\epsilon = 1$ and $\delta = 10^{-6}$. $n = 1$ was used as the closest approximation to the switch on in the previous model. Solid lines - total luminosity; dashed lines - propeller luminosity; dotted lines - dipole luminosity.

Table 2.3: The upper and lower limits placed on the fitting parameters in the MCMC routine. $M_{D,i}$, R_D , ϵ , and δ were searched in log-space for efficiency.

		Lower	Upper
B	($\times 10^{15}$ G)	10^{-3}	10
P_i	(ms)	0.69	10
$M_{D,i}$	(M_\odot)	10^{-6}	10^{-2}
R_D	(km)	50	2000
ϵ		0.01	100
δ		0.1	1000

Table 2.4: The parameter values used to generate synthetic light curves to test the MCMC routine.

Burst Type	B ($\times 10^{15}$ G)	P_i (ms)	$M_{D,i}$ (M_\odot)	R_D (km)	ϵ	δ
Humped	1	10	10^{-3}	100	1	1
Classic	1	5	10^{-3}	500	1	1
Sloped	1	1	10^{-2}	100	10	10
Stuttering	1	10	10^{-4}	100	1	10

given in Table 2.3 for fitting synthetic light curves.

$$\ln(p_{\text{prior}}) = \begin{cases} 0 & : x_l < x < x_u \\ -\infty & : \text{otherwise} \end{cases} \quad (2.27)$$

Hence, the full posterior probability distribution is calculated as follows.

$$\ln(p) = \ln(p_{\text{likelihood}}) + \ln(p_{\text{prior}}) \quad (2.28)$$

To test the routine, I extracted 50 random data points (from a uniform distribution) from each type of synthetic light curve generated in Section 2.4.1 to see if the correct values (given in Table 2.4) could be recovered. I added Gaussian noise to the synthetic data by defining an error bar to be an order of magnitude smaller than the luminosity value I had drawn, selected a random number from a Gaussian distribution with a mean of zero and a width equal to the generated error bar, and finally added this to the luminosity I had drawn. All the other parameters were given the fixed

Table 2.5: The numerical results derived from the MCMC fitting routine to synthetic light curves and the χ^2_ν goodness of fit statistic. The presented results are the median of the sampled population and the uncertainties represent a 95% confidence interval.

Burst Type	B ($\times 10^{15}$ G)	P_i (ms)	$M_{D,i}$ ($\times 10^{-3}$ M_\odot)	R_D (km)	ϵ	δ	χ^2_ν
Humped	$0.96^{+0.06}_{-0.08}$	$9.73^{+0.26}_{-0.46}$	$0.52^{+1.15}_{-0.35}$	85^{+70}_{-32}	$0.84^{+1.24}_{-0.31}$	$2.48^{+7.68}_{-2.18}$	1.24
Classic	$0.95^{+0.10}_{-0.09}$	$4.85^{+0.18}_{-0.16}$	$1.25^{+0.90}_{-0.79}$	673^{+467}_{-393}	$1.24^{+11.2}_{-0.63}$	$0.62^{+2.24}_{-0.48}$	1.06
Sloped	$1.03^{+0.13}_{-0.13}$	$0.99^{+0.03}_{-0.03}$	$8.24^{+1.67}_{-2.20}$	63^{+21}_{-12}	$18.1^{+5.19}_{-5.06}$	$12.2^{+4.89}_{-2.45}$	1.00
Stuttering	$0.98^{+0.06}_{-0.08}$	$9.78^{+0.21}_{-0.35}$	$0.10^{+0.05}_{-0.04}$	93^{+24}_{-17}	$1.09^{+0.48}_{-0.38}$	$9.75^{+6.34}_{-3.46}$	0.79

values discussed in Section 2.4 and were not classed as fitting variables in the routine. Initially, I ran trials consisting of 50 walkers taking 20,000 steps with initial positions very close to the true parameters. As a result, the burn-in phase for these trials were very short at 500 steps per walker in each case.

When testing the MCMC routine, I found difficulties with “bad” models, *i.e.*, models that caused *ODEPACK* - which is the routine used to integrate Equations (2.11) and (2.14) - to raise integration errors. I found most of these errors were due to *ODEPACK* being unable to integrate over the irregularly spaced time arrays I had generated to mimic the *Swift* data I intended to use. I solved this problem by having *ODEPACK* integrate over a evenly spaced array and interpolated the required data points off this “smooth” model. However, this still left some “bad” models that were a result of numerical failures of the integrator solely due to the randomised nature of the chosen input parameters. Since there is no way to predict these models, I developed a flag which would assign these nuisance parameter sets an infinite probability and output them to a file so they could be removed from the MCMC chain after the simulation had completed.

Table 2.5 presents the results of the MCMC. The values given are the median of the population and the uncertainties represent a 95% confidence interval. I chose the median, rather than the mean or mode, since it is less sensitive to the tails of distributions and is preserved under reversible transformations of the data (*e.g.*, $\log_{10} \epsilon \rightarrow \epsilon$). The MCMC is very successful in recovering the values for B and P_i for each burst type. The results for ϵ and δ have a much wider and asymmetric

uncertainty range and aren't as close to the true values. The reasons for this will be discussed in Section 2.5.1 where the correlations brought to light by the MCMC are discussed. The routine performs well when fitting type I and II bursts, though there are some competing effects between ϵ and δ . I have only provided here a plot for the type I burst as an example in Fig. 2.7.

2.5.1 Correlations

Fig. 2.8 shows a scatterplot matrix of the sample distribution for each parameter tested by the MCMC routine with burn-in steps removed. It reveals some strong correlations between some of the parameters: $r_{B,P_i} = 0.85$, $r_{M_{D,i},\epsilon} = 0.70$, $r_{M_{D,i},\delta} = -0.98$, $r_{\epsilon,\delta} = -0.77$ (where $r_{x,y}$ is the Pearson's product-moment correlation coefficient between parameters x and y ; $r_{B,P}$ is the only correlation coefficient not given in log-space). The correlation between B and P_i has a physical significance as it indicates that a magnetar born with lower magnetic fields requires faster initial spin periods in order for the propeller regime to be efficient (Rowlinson et al., 2013; Gompertz et al., 2014). Similarly, the strong, negative correlation in log-space between $M_{D,i}$ and δ makes physical sense as more mass will be required to fallback into the disc if the initial mass contained in the disc is small.

The strong, negative correlation between ϵ and δ is a surprising one in terms of the physical model. One would at least expect a positive correlation as more mass would need to fall back on a longer timescale to produce the same effect. Investigation into the cause of this revealed that ϵ and δ both affect when the condition for propellering is satisfied ($r_m > r_c$). Increasing the density of the disc with a large amount of fallback mass or a short fallback timescale (*i.e.*, increasing δ or decreasing ϵ) increases the spin frequency of the magnetar required for propellering. However, a denser disc promotes a higher accretion rate which spins the magnetar up to meet the propellering condition at an earlier time. Therefore, ϵ and δ are competing for dominance in controlling the propellering condition and how quickly it is met, thus generating the strong correlation shown in Fig. 2.8. The strong correlation between $M_{D,i}$ and ϵ is an artefact of the non-Gaussian probability density distribution generated for ϵ through the strong correlation with δ .

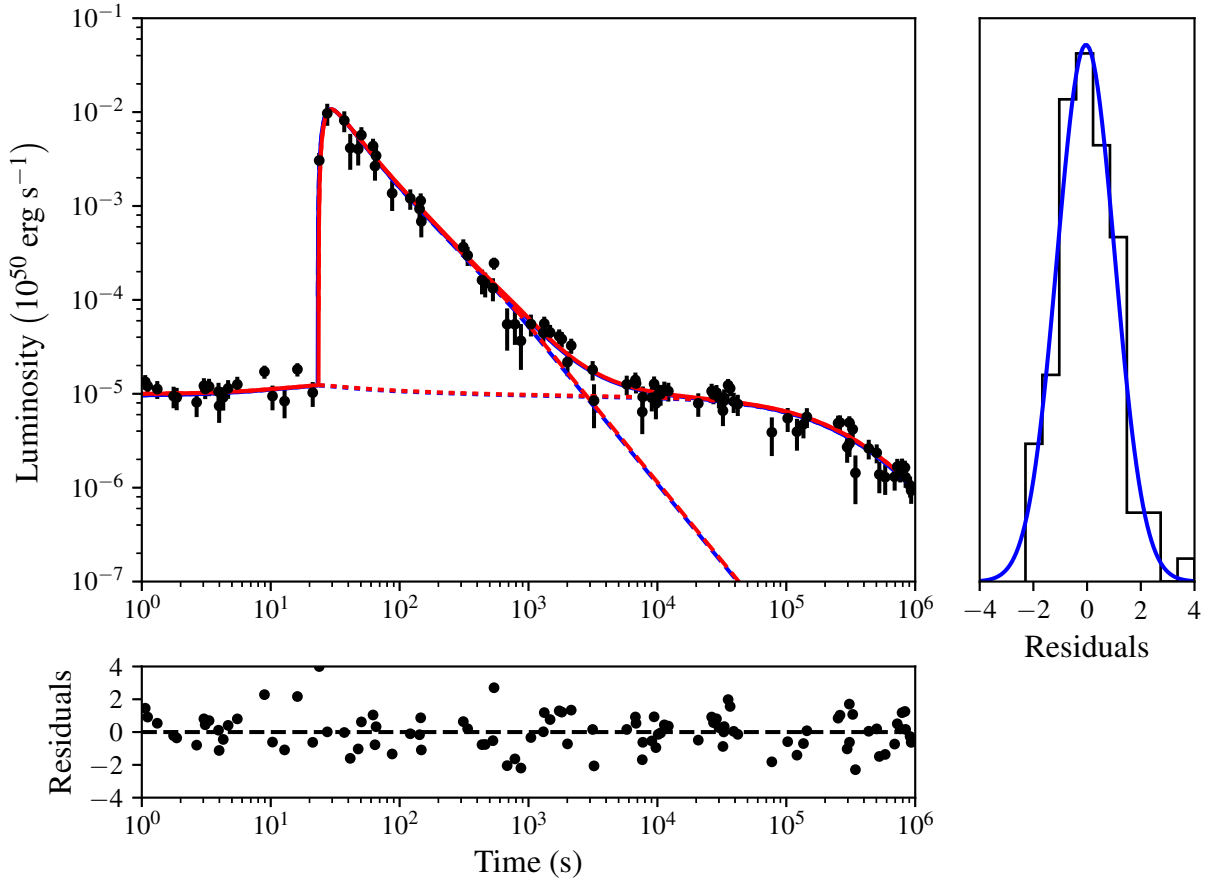


Figure 2.7: The model generated by MCMC fitting to a type I synthetic light curve. **Main panel:** black points - synthetic data with added Gaussian noise; blue curves - true synthetic light curve; red curves - recovered light curve; dashed lines - propeller luminosities; dotted lines - dipole luminosities; solid lines - total luminosities. **Bottom panel:** the residuals of the fit calculated from $(y_{\text{obs}} - y_{\text{model}}) / \sigma_{\text{obs}}$. **Right panel:** histogram of the residuals with fitted Gaussian profile (blue line) of $\mu \simeq 0$ and $\sigma \simeq 1$. This indicates the residuals likely come from the added Gaussian noise.

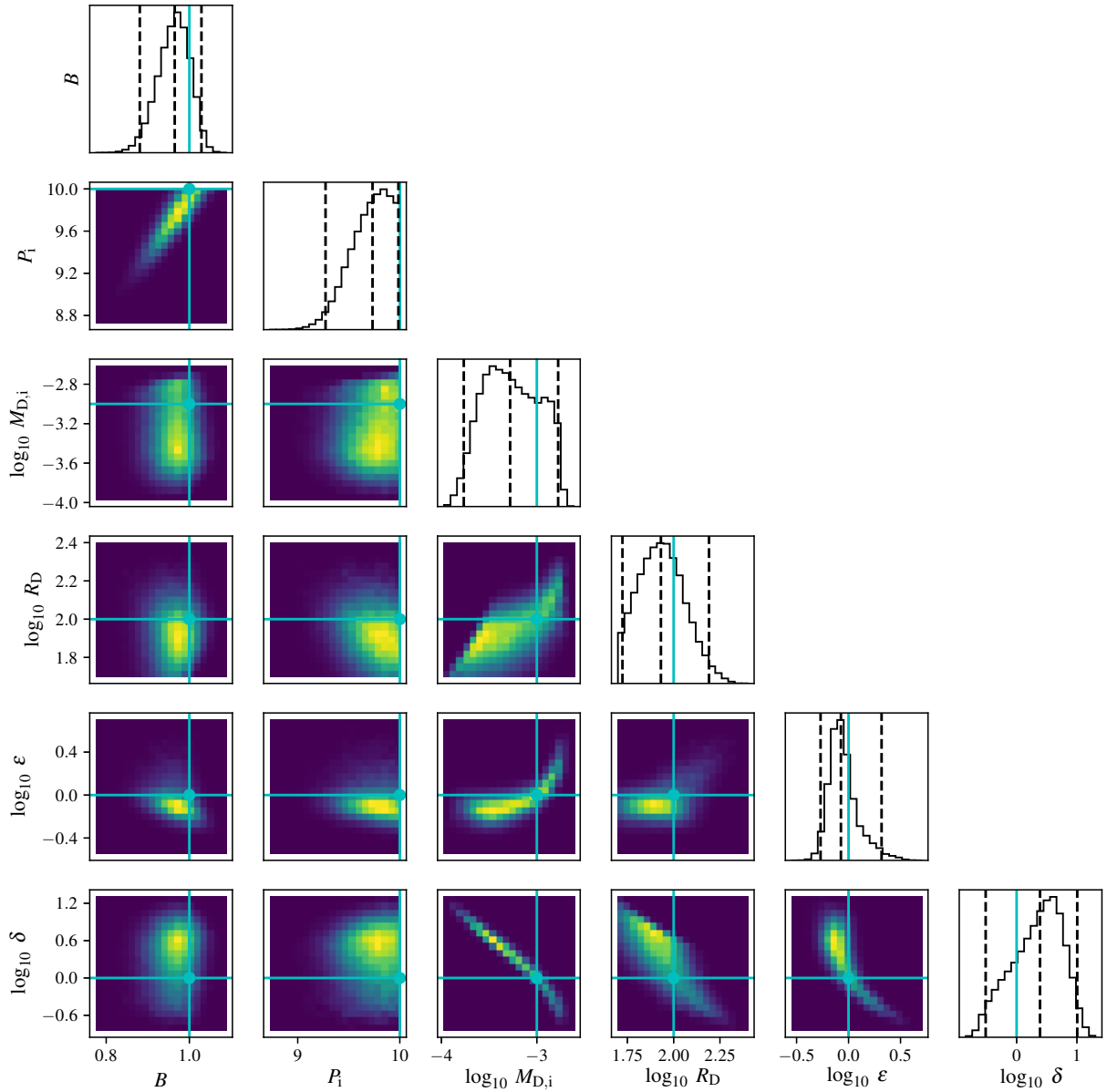


Figure 2.8: A scatterplot matrix showing all the values for each parameter the MCMC investigated after the burn-in phase. Strong correlations can be seen between B and P_1 ; $M_{D,i}$ and ϵ (in log-space); $M_{D,i}$ and δ (in log-space); and ϵ and δ (in log-space). The blue lines indicate the true parameter values. The dashed black lines on the histograms indicate the median value and a confidence interval of 95%.

Examples of the correlations when fitting other burst types are presented in Figs. C.1, C.2 and C.3 in Appendix C where it can be seen that the strong correlations between $M_{D,i}$ and δ , $M_{D,i}$ and ϵ , and ϵ and δ remain. The correlation between B and P_i is absent in the ‘sloped’ case since the dipole and propeller emission are indistinguishable and an effective propeller mechanism cannot be constrained.

While these plots reveal some strong correlations, the correlations change strength and shape for each burst type. In the ‘sloped’ burst case (Fig. C.2), the correlation between B and P_i disappears completely because the dipole and propeller luminosity components are indistinguishable from one another in the light curve. Therefore, the parameters cannot always be degenerate with one another since the correlations change as the input parameters are varied and hence a treatment of these degeneracies is not required, even when the number of free parameters is increased in Chapters 3 and 4.

2.6 Summary

The magnetar model is a naturally long-lived central engine that can provide continuous energy injection into a GRB fireball in order to explain phenomena such as: X-ray plateaux (Rowlinson et al., 2013; Gompertz et al., 2013), extended emission in SGRBs (Gompertz et al., 2014), and flares (Chincarini et al., 2010). This can be achieved by the extraction of rotational energy from the magnetar and conversion into emission via a Blandford-Znajek mechanism (Blandford & Znajek, 1977) or magnetic propeller (Piro & Ott, 2011; Gompertz et al., 2014).

Since, after a collapsar or compact object binary merger, it is expected that a reservoir of mass would be available for fallback (up to $\approx 0.1 M_{\odot}$; Rosswog 2007; Lee et al. 2009), I modified a simple version of the magnetic propeller model to include fallback accretion. Fallback accretion augments the energy budget of the magnetar as it provides a mechanism to spin the magnetar back up, and hence easing the restrictions on the upper limit of the rotational energy of the magnetar. I implemented a ballistic fallback rate of $t^{-\frac{5}{3}}$ (Rosswog, 2007) and parameterised the fallback

parameters ϵ and δ in terms of the viscous timescale, t_ν , and initial disc mass, $M_{D,i}$, respectively; so that $t_{fb} = \epsilon t_\nu$ and $M_{fb} = \delta M_{D,i}$.

During testing of the modified model, I have shown that the four types previously defined in Gompertz et al. (2014) are recoverable with the modifications, although they have moved in parameter space, and uncovered new morphologies of light curves. I have also shown that the dipole torque used from Bucciattini et al. (2006) has very little effect on the light curve morphology within the modified model. Finally, I developed an MCMC optimisation routine and recovered the parameters of four light curves (one from each type) successfully. I also explored the underlying correlations that drive the model, such as: $B-P_i$ which has a strong positive correlation in order to produce an effective propeller, $M_{D,i}-\delta$ which has a strong negative correlation in log-space in order to maximise the total amount of mass available thereby maximising the total energy budget, and $\epsilon-\delta$ which has a strong negative correlation due to both parameters attempting to control the switch-on of the propeller regime and is completely artificial.

3

Fallback Accretion on to a Newborn Magnetar: Short GRBs with Extended Emission

The work presented in this chapter was published in Gibson et al. (2017).

Abstract

There are a subset of short gamma-ray bursts (SGRBs) which exhibit a re-brightening in their high-energy light curves known as extended emission. These bursts have the potential to discern between various models proposed to describe SGRBs as any model needs to account for extended emission. In this chapter, I use a Markov chain Monte Carlo simulation to fit the magnetar propeller model with fallback accretion to the afterglows of 15 SGRBs exhibiting extended emission from the *Swift* archive. I present fits to the extended emission SGRB sample that are morphologically and energetically consistent with the data provided by *Swift*-BAT and XRT telescopes. The parameters derived from these fits are consistent with predictions for magnetar properties and fallback accretion models. Fallback accretion provides a noticeable improvement to the fits of the light curves of SGRBs with extended emission when compared to previous work and could play an important role in explaining features such as variability, flares and long dipole plateaux.

3.1 Introduction

SGRBs with extended emission are a subset of SGRBs which show re-brightening in their high-energy light curves after the prompt emission spike (approximately 10 s after trigger), which is referred to as the extended emission (Norris & Bonnell, 2006). The peak flux of extended emission is usually lower than the initial spike but it can last for a few hundred seconds, therefore the total fluence is often higher (Perley et al., 2009). They are believed to be a subset of SGRBs due to their hard spectra, association with galaxies with low star-forming rates and the lack of any detectable supernovae coincident with the burst. These bursts are an interesting subset to study since any model hoping to describe SGRBs generally needs to account for those which exhibit extended emission and provide an argument as to why some bursts don't, or determine whether extended emission is just an observational artefact. Also, a model would need to explain extended emission energetically and account for the similar total energy in the extended and the prompt emissions.

Different mechanisms have been suggested to power extended emission, including magnetar spin-

down (Metzger et al., 2008; Bucciantini et al., 2012), a two-jet solution (Barkov & Pozanenko, 2011), fallback accretion (Rosswog, 2007), r -process heating of the accretion disc (Metzger et al., 2010), and magnetic reconnection and turbulence (Zhang & Yan, 2011). Previously, Gompertz et al. (2014) have implemented a propeller model with a magnetar central engine as an explanation for extended emission bursts. The magnetar is believed to be formed during the merger of two compact objects, *i.e.*, a neutron star binary (Rosswog et al., 2003; Belczynski et al., 2006), a white dwarf binary (Chapman et al., 2007), or a neutron star-white dwarf binary. Compact object binary mergers are also the most popular candidates for SGRB progenitors. Magnetars have proven to be a favourable central engine choice since the energy released from their magnetic field via dipole spin-down is comparable to the energy contained within the extended emission. The magnetic propeller model aims to extract the energy required for extended emission from mass ejected from the system via the propeller mechanism. The version presented in Gompertz et al. (2014) consists of a static disc which is fully formed at $t = 0$ and is drained via either accretion or propelling. The results presented in Gompertz et al. (2014) run out of energy before fitting the fading afterglow, since the energy reservoir is not replenished, and does not fit to the prompt emission.

Models such as Rosswog (2007), Kumar et al. (2008), and Cannizzo et al. (2011) predict the fallback of mass into a disc and so the version of the propeller model presented in Chapter 2 has been extended to include fallback accretion. This replenishes the disc and thereby increases the overall available energy budget within the model. This means that the mass of the disc can vary over time as opposed to the static disc presented in Gompertz et al. (2014) and affects the spin-up of the magnetar thereby changing the morphology of the light curves produced. This extension to the model will allow me to fit the prompt emission and retain enough energy to fit the fading afterglow where previous models could not. The fallback rate is modelled with a $t^{-\frac{5}{3}}$ profile (Rosswog, 2007) and the fallback timescale, along with the available fallback mass, have been parameterised in terms of preexisting parameters within the model. I aim to explain the prompt emission (and hence all of the high-energy light curve) with a single model. As well as the addition of fallback mass and disc physics into the model, I have also introduced a new model for the propeller, fitted with variable efficiency parameters, and fitted to prompt emission data

which were not included in Gompertz et al. (2014).

Section 3.2 introduces the sample of SGRBs with extended emission to be studied and Section 3.3 briefly revisits the method used to fit the model to the data. Results and concluding remarks are presented in Sections 3.4 and 3.5 respectively.

3.2 *Swift* SGRB with Extended Emission Sample

The data for the GRB sample were collected by the *Swift* satellite (Gehrels et al., 2004), which is a multi-wavelength observatory with rapid slewing capabilities that was launched in 2004. It carries three instruments: the Burst Alert Telescope (BAT; Barthelmy et al. 2005), the X-ray Telescope (XRT; Burrows et al. 2005a), and the Ultra-Violet/Optical Telescope (UVOT; Roming et al. 2005). The *Swift* mission and the UK *Swift* Science Data Centre (UKSSDC¹, Evans et al. 2007, 2009) provided the data presented here.

The data need to undergo a cosmological k -correction and absorption correction, as described in Bloom et al. (2001), to produce bolometric (1 – 10000 keV), redshift-corrected light curves before they can be fitted by the model. This method requires the photon index, Γ , the absorption coefficient, σ (given by the ratio of counts-to-flux unabsorbed to counts-to-flux observed, which are all available on the UKSDCC repository) and the redshift, z , some of which were found in the literature (see Table 3.1).

The sample studied in Gompertz et al. (2013) and Gompertz et al. (2014) has been expanded here by selecting identified SGRBs with extended emission from Kaneko et al. (2015) (which covers bursts to the end of 2012) that have good data available in the *Swift* archive. Plus GRBs 150424A and 160410A which are identified as extended emission bursts within GCN Circulars (Norris et al. 2015 and Sakamoto et al. 2016 respectively). The data used in the fitting incorporates XRT data and BAT data that have been extrapolated into the XRT bandpass (available from the UKSDCC Burst Analyser tool) since the effect of the extended emission is not always evident in the XRT

¹www.swift.ac.uk

Table 3.1: The sample of SGRBs with extended emission and the parameters required for a cosmological k -correction. For GRBs with an unknown redshift (marked with an *), the sample mean of 0.39 from Gompertz et al. (2014) was used. [†]Upper limit (D’Avanzo et al., 2009). ^aProchaska et al. (2005); ^bSoderberg et al. (2005); ^cPrice et al. (2006); ^eBerger (2007); ^dCenko et al. (2006); ^eGraham et al. (2009); ^fD’Avanzo et al. (2007); ^gSelsing et al. (2016).

GRB	Γ	σ	z
050724	$1.58^{+0.21}_{-0.19}$	1.26	0.2578 ^a
051016B	$1.85^{+0.14}_{-0.13}$	1.31	0.9364 ^b
051227	$2.1^{+0.4}_{-0.4}$	1.31	2.8 [†]
060614	$1.78^{+0.08}_{-0.08}$	1.06	0.1254 ^c
061006	$2.1^{+0.6}_{-0.4}$	1.61	0.4377 ^c
061210	$2.60^{+1.92}_{-0.71}$	3.48	0.4095 ^d
070714B	$1.79^{+0.24}_{-0.22}$	1.15	0.9224 ^e
071227	$1.5^{+0.6}_{-0.5}$	1.02	0.381 ^f
080123	$2.46^{+1.04}_{-0.70}$	1.71	0.39*
080503	$2.38^{+0.42}_{-0.16}$	1.24	0.39*
100212A	$1.99^{+0.40}_{-0.18}$	1.37	0.39*
100522A	$2.40^{+0.17}_{-0.16}$	2.45	0.39*
111121A	$1.78^{+0.21}_{-0.20}$	1.42	0.39*
150424A	$1.98^{+0.24}_{-0.22}$	1.23	0.39*
160410A	$1.5^{+0.7}_{-0.6}$	1.02	1.717 ^g

light curve alone.

3.3 Optimisation Routine

For the Markov chain Monte Carlo (MCMC), 100 affine invariant walkers (Goodman & Weare, 2010) were implemented and ran for a 50,000 step burn-in phase to allow the walkers to test as much of parameter space as possible. After this run, the best 100 distinct probabilities were

Table 3.2: Upper and lower limits placed on the fitting parameters in the MCMC. $M_{D,i}$, R_D , ϵ , and δ were searched in log-space for efficiency.

		Lower	Upper
B	($\times 10^{15}$ G)	10^{-3}	10
P_i	(ms)	0.69	10
$M_{D,i}$	(M_\odot)	10^{-3}	10^{-1}
R_D	(km)	50	2000
ϵ		0.1	1000
δ		10^{-5}	50
η_{dip}	(%)	1	100
η_{prop}	(%)	1	100
$1/f_B$		1	600

chosen to serve as the starting point for the final MCMC run of the same length. This made sure that the parameters recovered were representative of the global minimum, not a local minimum, and reduces the burn-in of the chain to < 1000 steps in most cases. Although, if the time series (parameter or probability value vs. model number for each walker) showed that the chain had not fully converged, the process of selecting the 100 best probabilities was repeated and the chain run again until convergence was achieved. The values given in Table 3.2 were used to constrain the walkers in the prior probability distribution (Equation 2.27). The optimal parameters were found by taking the median of the posterior probability distributions and their uncertainties are given by 95% confidence intervals.

Fits to the SGRB sample with extended emission were produced with a range of free parameters (p): $p = 6$ (B , P_i , $M_{D,i}$, R_D , ϵ and δ); 7 (original 6 plus $1/f_B$); 8 (original 6 plus η_{dip} and η_{prop}); and 9 (all listed parameters). η_{dip} , η_{prop} and $1/f_B$ were fixed to 5%, 40% and 1 respectively when they were not free parameters, maintaining consistency with Gompertz et al. (2014). The fits were repeated for fixed values of $n = 1, 10, 100$ and the corrected Akaike Information Criterion (AICc; Cavanaugh & Neath 2011) was used to establish the best-fitting models. I chose this statistic since it allows me to compare models of varying free parameter number (p).

AICc is given by the following equation

$$AICc = -2 \ln(L) + 2k + \frac{2k(k+1)}{N-k-1} \quad (3.1)$$

where k is the number of free parameters and N is the number of observations in the data set. This penalises a model for ‘over-fitting’ and scales with k . I have substituted Equation (2.26) for the maximum log-likelihood $\ln(L)$, which then cancels down to the χ^2 statistic. The minimum AICc value within a set is then representative of the optimum model fit since if the AICc value of a model that has a large number of free parameters (and hence a large penalty) is less than a model with fewer free parameters (and hence a smaller penalty), then it can be generally assumed that the extra parameters improve the quality of fit.

3.4 Results and Discussion

Table 3.3 presents the AICc values for all results of the optimisation routine. The large spread of values is representative of the difficulty χ^2 (the root of the AICc) has comparing a smooth model with highly variable data, especially in the early-time BAT data. Table 3.3 shows that the general picture of the model is stable over all n values since there is a reasonable spread of best fits. This also confirms the observation made in Section 2.4 that the model is reasonably insensitive to n . Increasing n only makes features such as humps appear sharper, which does not have a great impact on the overall quality of the fit. The best global fits to the SGRB sample with extended emission (bold values in Table 3.3) are presented in Fig. 3.1.

The $p = 6$ set represents the core physics of the model by constraining the fundamental properties of the magnetar (B and P_i), the accretion disc ($M_{D,i}$ and R_D) and the fallback (M_{fb} and t_{fb} through δ and ϵ respectively) and is the most energetically restricted case compared to the $p = 9$ case which has the largest energy reservoir. Furthermore, η_{dip} and η_{prop} determine the efficiency at which the dipole and propeller mechanisms respectively need to work at in order to convert the energy to luminosity. Lastly, f_B accounts the anisotropy of the radiation ($1/f_B$ is the fraction of the stellar sphere which is emitting).

Table 3.3: AICc values for models using 6, 7, 8 and 9 free parameters (p) for $n = 1, 10, 100$ fitted to the SGRB sample with extended emission. Underlined values are the lowest AICc values for each n bracket and values in **bold** are the minima across all values of n . Values marked with an * are modified since $N - k - 1 \leq 0$ for these models.

GRB	$n = 1$			$n = 10$			$n = 100$					
	$p = 6$	$p = 7$	$p = 8$	$p = 6$	$p = 7$	$p = 8$	$p = 6$	$p = 7$	$p = 8$	$p = 9$		
050724	2,085	<u>1,741</u>	1,820	1,748	2,104	1,654	2,062	1,653	2,212	1,932	2,058	1,673
051016B	725	426	674	<u>393</u>	721	371	635	499	728	<u>442</u>	585	514
051227	335	<u>311</u>	318	338	325	332	318	<u>232</u>	325	224	318	234
060614	47,253	44,796	47,252	45,949	45,966	44,915	<u>44,886</u>	44,888	46,519	46,017	46,009	<u>45,535</u>
061006	365	191	225	183	277	<u>210</u>	217	244	254	<u>223</u>	285	290
061210	570	538	543*	387	815	<u>529</u>	2,452*	1,778	<u>1,039</u>	39,862,020	9,950*	6,711
070714B	<u>1,260</u>	1,282	1,284	1,331	1,260	<u>1,004</u>	1,285	1,349	1,260	5,612	1,285	835
071227	149	187	158	194	182	<u>178</u>	204	186	189	<u>156</u>	333	212
080123	426	431	<u>302</u>	339	274	399	282	463	<u>310</u>	370	318	383
080503	<u>2,321</u>	2,323	2,337	2,348	2,305	2,314	2,305	<u>2,302</u>	2,217	2,219	2,220	2,223
100212A	<u>8,646</u>	9,084	8,695	8,918	8,622	8,594	8,675	8,695	<u>8,675</u>	8,741	8,699	8,770
100522A	25,724	25,254	25,182	25,225	25,694	25,696	<u>25,677</u>	25,695	25,694	25,696	<u>25,677</u>	25,680
111121A	<u>1,748</u>	1,750	1,753	<u>1,748</u>	1,753	<u>1,738</u>	1,752	1,940	1,753	1,732	1,753	2,819
150424A	2,456	2,516	2,301	<u>2,163</u>	2,282	2,479	<u>1,683</u>	2,260	1,987	1,555	2,343	1,560
160410A	475	405	406	416	468	<u>411</u>	414	492	459	596	<u>414</u>	538

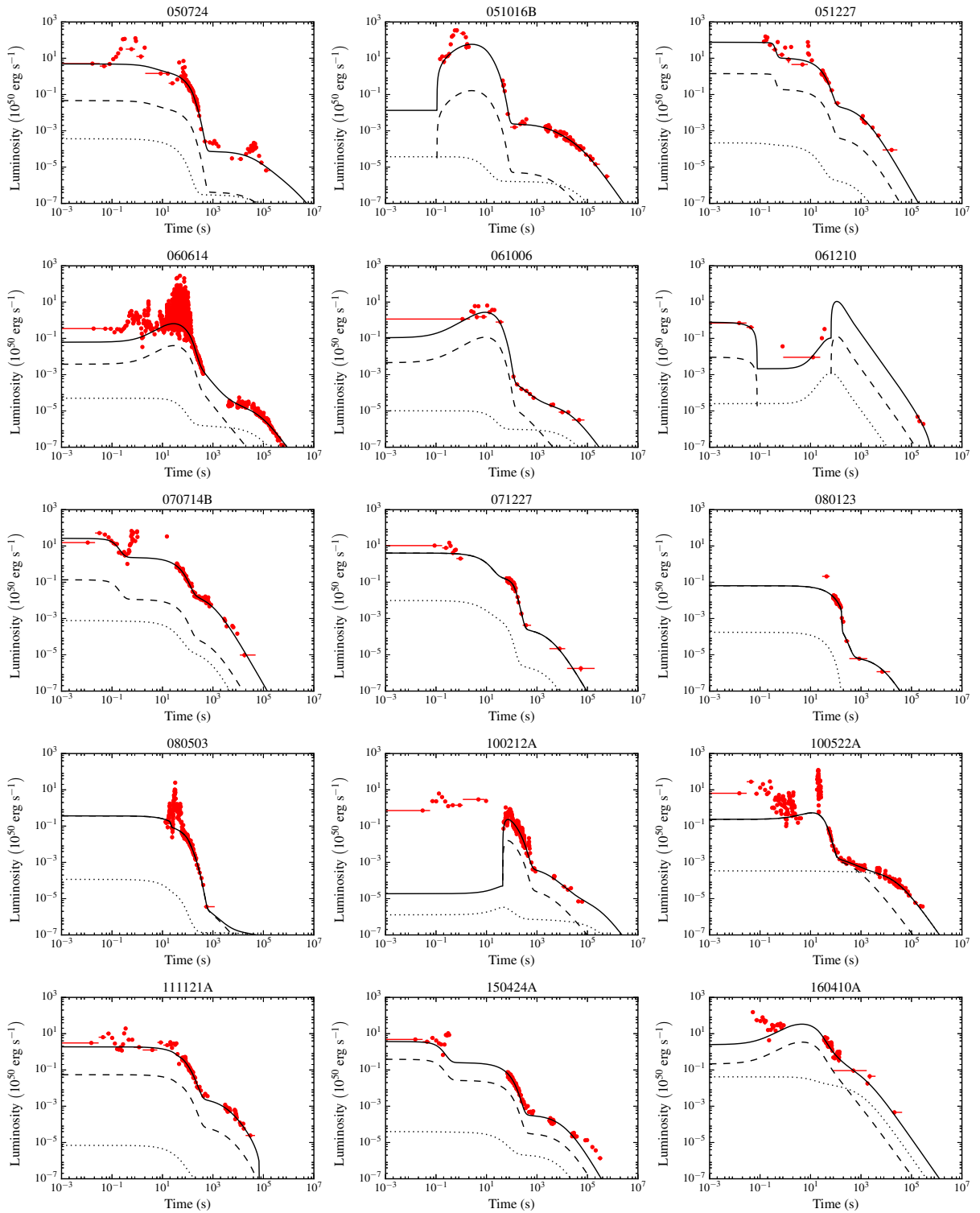


Figure 3.1: Best global fits to the SGRB sample with extended emission (bold values in Table 3.3). Dashed line - propeller luminosity; dotted line - dipole luminosity; solid line - total luminosity; red points - combined BAT and XRT data.

Table 3.4: Table showing the half-opening angles (in radians) for 4 GRBs, calculated from $f_B = 1 - \cos(\theta_j)$. θ_j values are from the global best fits of this work (uncertainties are 95% confidence interval); θ_0 values are from Ryan et al. (2015).

GRB	θ_j	θ_0
051016B	$0.07^{+0.14}_{-0.12}$	$0.35^{+0.11}_{-0.24}$
060614	$0.35^{+0.93}_{-0.99}$	$0.293^{+0.122}_{-0.085}$
061006	$0.29^{+0.38}_{-0.42}$	$0.407^{+0.068}_{-0.173}$
070714B	$0.10^{+0.07}_{-0.11}$	$0.33^{+0.11}_{-0.11}$

The results of the MCMC were analysed for parameter correlations though none were found since my method of selecting the best probabilities after the burn-in phase removes most strong correlations by placing the parameters in the global minimum.

The k -correction performed in Section 3.2 assumes isotropic emission, whereas in actuality, GRBs are beamed into a very narrow opening angle due to their relativistic velocity (Fruchter et al., 1999; Harrison et al., 1999; Frail et al., 2001). Rather than divide the data down to a beam-corrected level, my routine works to multiply the model up to the isotropic luminosity level so that model comparison becomes easier on the same scale. The morphologies of the fits change as each new parameter is introduced since they handle the high luminosities at early times allowing the core parameters to reconfigure. This means that there can be more energy available at late times to fit the fading afterglow.

It is interesting to compare the freedom of the model (*i.e.*, how many free parameters are used) with the “sharpness” of the propeller (*i.e.*, the n value). Generally speaking, the AICc value of the fit improves as the number of free parameters increases, whereas, increasing n for the same number of free parameters often does not improve the fit. Also, $p = 8$ fits often perform worse than $p = 7$ fits implying that the beaming fraction has a greater role within the model than the efficiencies, but the inclusion of all 3 of these parameters are most preferable. Table 3.4 shows a comparison of the jet half-opening angles derived from the best fits in this work with hydrodynamical modelling performed by Ryan et al. (2015) for 4 GRBs common to both studies. My model produces jets that are consistent with or slightly narrower than the values from Ryan et al. (2015). We are

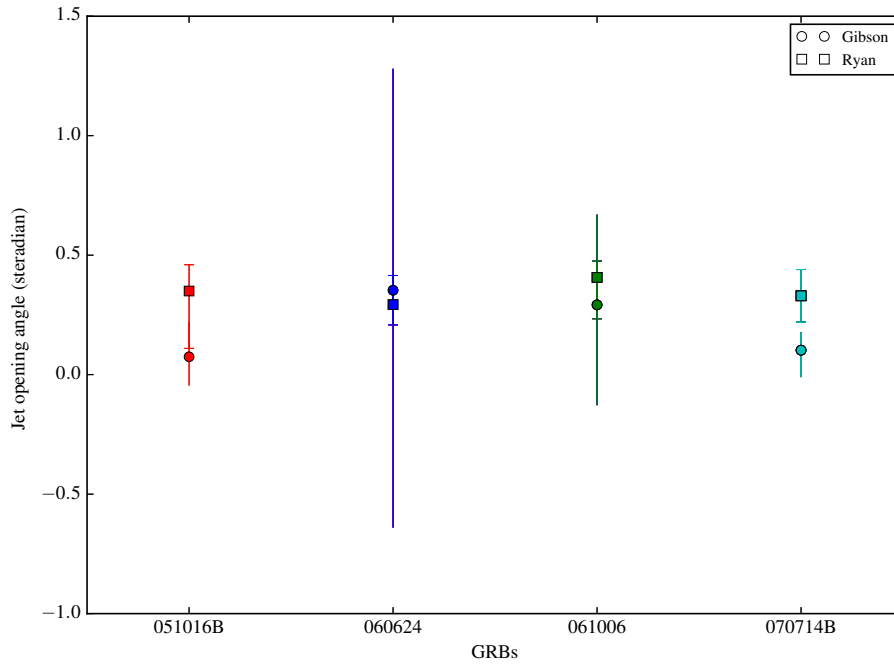


Figure 3.2: A graphical comparison of the beaming angle of 4 GRBs common to this work (circular point, uncapped error bars) and Ryan et al. (2015) (square point, capped error bars).

partially consistent with Ryan et al. (2015) in errors (*e.g.*, GRBs 051016B), and where they are not (*e.g.*, GRB 070714B), they are broadly consistent to $\sim 2 - 2.5\sigma$ (see Fig. 3.2).

Comparing my results with that of Gompertz et al. (2014), it is shown that the inclusion of fallback accretion within the propeller model allows for an improvement in fitting the ‘tail’ of the fading afterglow. This is can be seen in GRBs 051227, 060614 and 061006 where Gompertz et al. (2014) did not produce such good fits to the tail. Hence, fallback accretion is a necessary addition to the propeller model in order to fully explain the energetics and morphologies of SGRBs with extended emission. Additionally, the extended model handles variability and flares within the data much more naturally than Gompertz et al. (2014) and copes with the early-time luminosity detected by BAT.

The parameters derived from the fits in Fig. 3.1 are presented in Table 3.5. I find that the magnetic fields derived from the fits are in the moderate to high end of the parameter space and that the sample generally have slow initial spins. The slow initial spins are most likely due to the additional

Table 3.5: The parameters derived from the best global fits to the SGRB sample with extended emission (bold values in Table 3.3). Reported errors are 95%. Values marked with an [L] have reached a parameter limit; those marked with [F] were fixed during fitting. The χ^2_{ν} values are presented to indicate goodness of fit. χ^2_{ν} values marked with an * are modified values since $N - k - 1 \leq 0$. The last column gives the opening angle of the jet, θ_j , in steradians calculated from $f_B = 1 - \cos(\theta_j)$.

GRB	n [F]	B ($\times 10^{15}$ G)	P_i (ms)	$M_{D,i}$ ($\times 10^{-2} M_{\odot}$)	R_D (km)	ϵ	δ	η_{dip} (%)	η_{prop} (%)	$1/f_B$	χ^2_{ν}	θ_j (sr)
050724	10	$4.12^{+0.82}_{-1.14}$	$7.23^{+2.66}_{-3.36}$	$4.08^{+5.29}_{-1.51}$	469^{+8}_{-8}	$958.58^{+39.89}_{-139.25}$	$(5.79^{+2.25}_{-1.69}) \times 10^{-3}$	61^{+37}_{-42}	15^{+15}_{-9}	104^{+230}_{-79}	7	$0.14^{+0.09}_{-0.16}$
051016B	10	$7.09^{+0.63}_{-0.99}$	$8.97^{+0.98}_{-2.01}$	$1.31^{+0.48}_{-0.21}$	71^{+2}_{-2}	$596.24^{+240.77}_{-195.94}$	$(5.29^{+1.99}_{-1.91}) \times 10^{-3}$	5[F]	40[F]	358^{+96}_{-137}	4	$0.07^{+0.14}_{-0.12}$
051227	100	$9.50^{+0.48}_{-1.51}$	$6.69^{+2.19}_{-1.21}$	$7.83^{+2.06}_{-3.65}$	140^{+16}_{-11}	$79.81^{+54.19}_{-24.03}$	$6.37^{+3.25}_{-1.66}$	5[F]	40[F]	54^{+40}_{-17}	6	$0.19^{+0.22}_{-0.34}$
060614	1	$4.32^{+0.16}_{-0.16}$	$6.50^{+0.48}_{-0.46}$	$4.88^{+0.54}_{-0.47}$	349^{+3}_{-3}	0.10[L]	$(4.57^{+0.30}_{-0.34}) \times 10^{-2}$	5[F]	40[F]	16^{+3}_{-2}	19	$0.35^{+0.93}_{-0.99}$
061006	1	$7.81^{+1.72}_{-1.23}$	$9.20^{+0.77}_{-2.44}$	$2.17^{+1.82}_{-0.68}$	106^{+4}_{-5}	$11.66^{+15.28}_{-9.42}$	$(3.16^{+2.36}_{-0.73}) \times 10^{-4}$	1[L]	85^{+15}_{-39}	24^{+14}_{-12}	12	$0.29^{+0.38}_{-0.42}$
061210	1	$2.09^{+0.20}_{-0.39}$	$8.67^{+1.27}_{-2.93}$	$0.38^{+0.28}_{-0.07}$	408^{+38}_{-50}	$0.11^{+0.02}_{-0.01}$	$48.47^{+1.47}_{-6.09}$	34^{+31}_{-23}	60^{+38}_{-39}	84^{+196}_{-50}	-550*	$0.15^{+0.10}_{-0.20}$
070714B	100	$9.76^{+0.23}_{-0.61}$	$9.16^{+0.70}_{-0.67}$	$9.32^{+0.65}_{-1.36}$	297^{+14}_{-13}	$30.38^{+4.81}_{-4.07}$	$3.60^{+0.59}_{-0.54}$	60^{+38}_{-54}	9^{+46}_{-6}	191^{+358}_{-158}	7	$0.10^{+0.07}_{-0.11}$
071227	1	$5.26^{+0.86}_{-0.52}$	$1.92^{+0.17}_{-0.21}$	$5.22^{+2.54}_{-1.57}$	68^{+59}_{-17}	$521.30^{+422.42}_{-316.28}$	$20.68^{+19.34}_{-10.31}$	5[F]	40[F]	1[F]	4	-
080123	10	$9.54^{+0.44}_{-0.83}$	$7.08^{+0.44}_{-0.45}$	$1.22^{+0.12}_{-0.11}$	760^{+170}_{-122}	$91.46^{+65.44}_{-30.13}$	$17.27^{+11.67}_{-5.87}$	5[F]	40[F]	1[F]	6	-
080503	100	$2.67^{+0.11}_{-0.11}$	$4.15^{+0.09}_{-0.09}$	$4.68^{+0.28}_{-0.27}$	464^{+9}_{-9}	[U]	$(2.82^{+33.68}_{-2.67}) \times 10^{-4}$	5[F]	40[F]	1[F]	9	-
100212A	10	$1.49^{+0.07}_{-0.12}$	$9.57^{+0.41}_{-1.58}$	$1.62^{+0.53}_{-0.24}$	719^{+11}_{-11}	$43.12^{+10.25}_{-8.93}$	$(1.67^{+0.24}_{-0.23}) \times 10^{-2}$	5[F]	40[F]	15^{+3}_{-5}	22	$0.37^{+0.87}_{-0.66}$
100522A	1	$0.38^{+0.11}_{-0.04}$	$0.83^{+0.22}_{-0.07}$	$1.32^{+0.13}_{-0.12}$	130^{+3}_{-3}	$32.30^{+9.26}_{-7.14}$	$(1.85^{+0.29}_{-0.24}) \times 10^{-2}$	1[L]	80^{+18}_{-11}	1[F]	101	-
111121A	100	$2.71^{+0.25}_{-0.68}$	$8.43^{+1.50}_{-3.68}$	$1.35^{+1.55}_{-0.27}$	543^{+13}_{-14}	$65.91^{+22.69}_{-17.34}$	$(1.26^{+0.12}_{-0.12}) \times 10^{-1}$	5[F]	40[F]	34^{+13}_{-24}	13	$0.24^{+0.39}_{-0.29}$
150424A	100	$9.11^{+0.15}_{-0.15}$	$9.99^{+0.01}_{-0.05}$	$9.99^{+0.01}_{-0.06}$	443^{+14}_{-14}	$260.14^{+16.12}_{-16.60}$	$48.98^{+0.98}_{-4.35}$	5[F]	40[F]	$9.5^{+0.3}_{-0.3}$	12	0.46[L]
160410A	1	$2.52^{+2.50}_{-0.87}$	$0.92^{+0.64}_{-0.22}$	$0.12^{+0.11}_{-0.02}$	82^{+41}_{-19}	$0.35^{+0.28}_{-0.23}$	$33.38^{+15.56}_{-21.96}$	5[F]	40[F]	10^{+18}_{-4}	6	$0.46^{+0.33}_{-0.71}$

fallback spinning the magnetar up and, therefore, the constraints on high initial spin rates is relaxed. This has an impact on the value of the magnetic field derived as the fit moves along the correlation between B and P_i discussed in Gompertz et al. (2014). The sample fits also tend to favour massive discs and narrow jet opening angles. This is most likely due to the model extracting as much of the available energy as possible to fit the high luminosities at early times in the light curve, data which was not included in the fits of Gompertz et al. (2014). The values of ϵ , δ , η_{dip} and η_{prop} are widely distributed throughout the parameter space. The derived parameters are consistent with predictions for a magnetar (Giacomazzo & Perna 2013; Mereghetti et al. 2015; Rea et al. 2015) and are also consistent with the results in Gompertz et al. (2014).

I will now examine how increasing the number of free parameters affects the fits in 3 arbitrarily selected GRBs from the sample.

3.4.1 GRB 050724

Fig. 3.3 shows a comparison of fits with varying p to GRB 050724 for $n = 100$. For $p = 6$, the model misses the high luminosity at early times and does not retain enough energy to fit the tail after fitting the well-sampled drop in luminosity. The fit demanded a reasonable amount of fallback, $\delta = (4.82^{+2.75}_{-1.94}) \times 10^{-1}$, on a relatively short timescale, $\epsilon = 1.68^{+1.05}_{-0.77}$, and a rapid initial spin period, $P_i = 0.92^{+0.13}_{-0.04}$ ms, in order to produce a high luminosity so early. Since the fallback mass reaches the disc quickly, there is nothing left in the fallback budget to provide energy for the late-time emission. The $p = 8$ fit suffers similar issues and also fails to fit the tail. The $p = 7$ run provided an improved fit to the early-time luminosity and the tail. This fit required a small amount of fallback mass, $\delta = (1.45^{+6.62}_{-1.33}) \times 10^{-4}$, over a reasonably long timescale, $\epsilon = 10.30^{+579.07}_{-10.17}$, and a slow initial spin period, $P_i = 8.42^{+1.52}_{-3.82}$ ms, which kept the disc fed in order to produce sustained luminosity. $p = 9$ is the best-fitting model of this bracket but requires a highly efficient emission mechanism for the propeller, $\eta_{\text{prop}} = 73^{+25}_{-38}\%$.

It is interesting to note the late-time giant flare within the tail of GRB 050724 that the model has not been able to fit. At present, the phenomena that cause such large outbursts at these late times

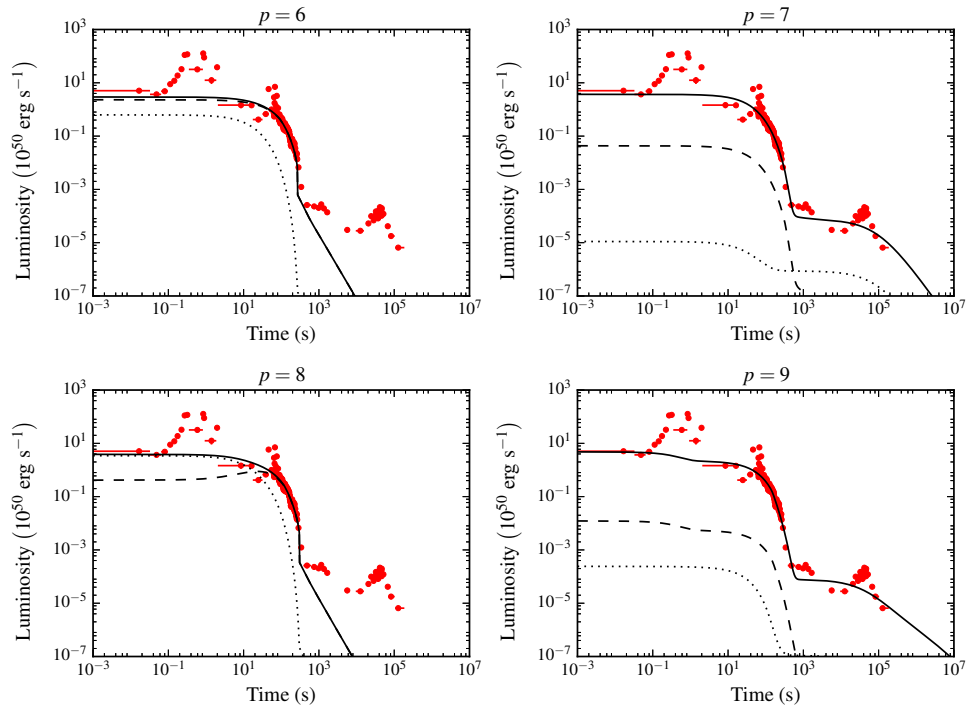


Figure 3.3: Models fitted to GRB 050724 with $n = 100$ and $p = 6$ (top left), 7 (top right), 8 (bottom left), and 9 (bottom right). Solid line - total luminosity; dashed line - propeller luminosity; dotted line - dipole luminosity; red points - combined BAT and XRT data.

are still poorly understood (*e.g.*, Falcone et al., 2006; Curran et al., 2008; Chincarini et al., 2010)).

3.4.2 GRB 060614

GRB 060614 poses a challenge to typical long/short classification scheme since it has a duration of ~ 100 seconds but the hard spectrum and lack of supernova connection are more indicative of the short classification (Mangano et al., 2007; Zhang et al., 2007; Xu et al., 2009).

Fig. 3.4 presents model fits of varying p and $n = 100$ to data for GRB 060614. The runs for $p = 6, 7$ and 8 all fit the tail of the emission but fail to fit the early-time data, instead creating a ‘humped’ feature while attempting to fit the period of rapid variability between 1 – 100 s. Again, $p = 9$ offers the best results for fitting to the tail and a reasonable fit to the early-time data but

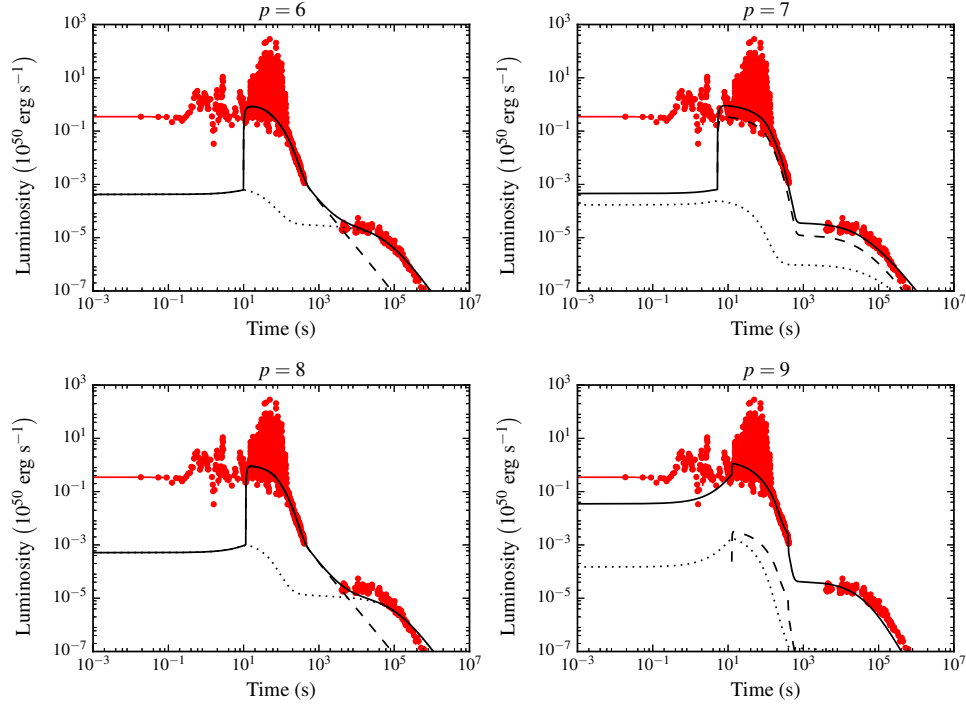


Figure 3.4: Models fitted to GRB 060614 with $n = 100$ and $p = 6$ (top left), 7 (top right), 8 (bottom left), and 9 (bottom right). Solid line - total luminosity; dashed line - propeller luminosity; dotted line - dipole luminosity; red points - combined BAT and XRT data.

requires extreme values of the emission efficiencies, $\eta_{\text{dip}} = 100\%$ (limit) and $\eta_{\text{prop}} = 1\%$ (limit), and a moderate beaming fraction, $1/f_B = 235_{-8}^{+17}$. In the case of the emission efficiencies, the propeller's main job is to modulate the spin in order to achieve the desired luminosities. Since the propeller plays a very small role in this particular fit, this indicates that that has been almost completely taken over by the fallback.

3.4.3 GRB 11121A

Fig. 3.5 presents model fits of varying p and $n = 100$ to data for GRB 11121A. This is an example of the model behaving well across all values of p . Despite the fits for $p = 6$, 7 and 8 looking very similar, the spin periods (and hence energy reservoirs) derived from the fits vary. Fits $p = 6$ and 8 have very similar and rapid initial spin periods and $P_i = 1.25_{-0.19}^{+0.09}$ ms and $P_i = 1.82_{-0.64}^{+0.32}$ ms

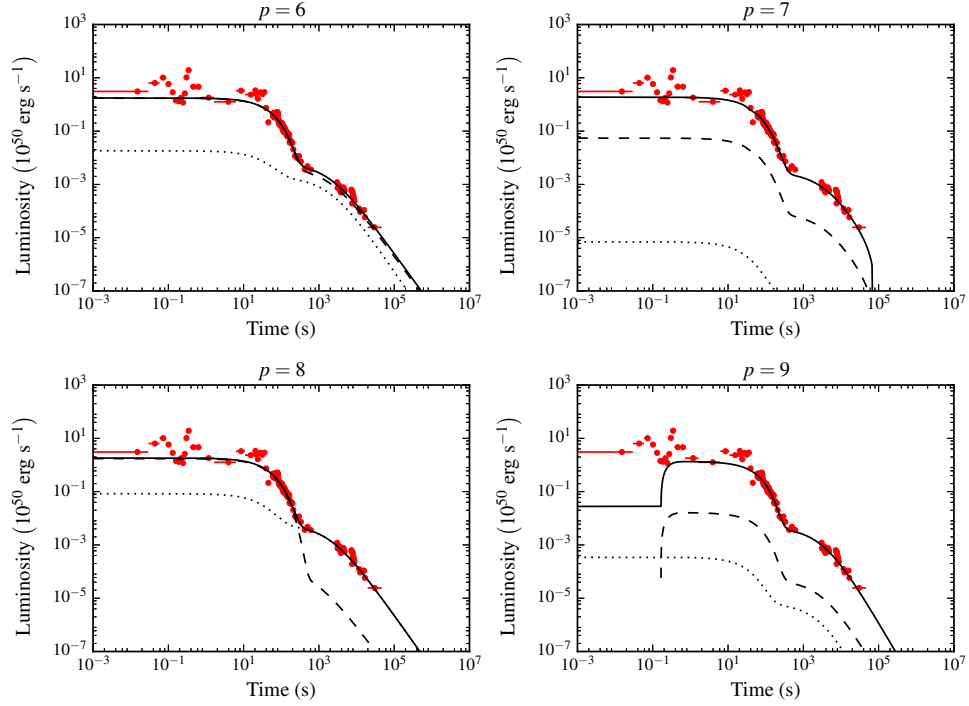


Figure 3.5: Models fitted to GRB 111121A with $n = 100$ and $p = 6$ (top left), 7 (top right), 8 (bottom left), and 9 (bottom right). Solid line - total luminosity; dashed line - propeller luminosity; dotted line - dipole luminosity; red points - combined BAT and XRT data.

respectively, whereas $p = 7$ has a slower initial spin period of $P_1 = 8.43_{-3.68}^{+1.50}$ ms.

Lastly, the $p = 9$ fit has a large magnetic field and slow spin of $B = 8.47_{-0.65}^{+0.44} \times 10^{15}$ G and $P_1 = 9.74_{-0.71}^{+0.25}$ ms respectively. It has a slowly fed disc with a large amount of fallback mass, $\epsilon = 79.62_{-10.61}^{+14.49}$ and $\delta = 7.64_{-1.35}^{+1.12}$. I derive a propeller efficiency of $\eta_{\text{prop}} = 20_{-15}^{+63}\%$ but the dipole efficiency could not be adequately constrained. The fit also produces a broad jet opening angle of $1/f_B = 81_{-61}^{+212}$. However, this fit does use a flare to fit the early-time data which could be indicative of over-fitting.

3.4.4 Refitting Excluding Early-Time Data

The results presented in Table 3.5 show that the model requires quite massive discs initially. This is most likely due to the model’s need to have a high accretion rate at early-times in order to reach the high luminosities at those times. Since the emission produced at these times is usually attributed to internal shocks and energy drawn from the merger rather than magnetic particle acceleration, fitting these high early-time luminosities may not strictly be within the remit of the model. I therefore chose to refit the sample excluding some of the early-time data.

I chose an arbitrary cut-off of 10 seconds to define the on-set of extended emission after the prompt emission. This meant I avoided making an arbitrary cut for each individual burst since extended emission isn’t currently well defined. The fits were performed for $p = 6, 7, 8$ and 9 and $n = 1$ for comparison with the work in Gompertz et al. (2014).

Table 3.6 presents the AICc values of the refits. The best fits (bold values) from Table 3.6 are plotted in Fig. 3.6 and the parameters derived from these fits are presented in Table 3.7 with the χ^2_ν goodness of fit statistic. GRB 061210 has very few data points and excluding data < 10 seconds means that there are fewer data points than free parameters which resulted in negative AICc and χ^2_ν values. Therefore, it is shown here for consistency rather than as a statistically significant result.

As is shown in Fig. 3.6, the result of excluding the early-time data is to produce more light curves of the ‘humped’ morphology than ‘sloped’ or ‘classic’ in Fig. 3.1. But most surprisingly, this experiment did not succeed in reducing $M_{D,i}$ as expected with values still reaching the moderate to high range, suggesting the extra mass is a result of another change in the model, most likely the use of Equation (2.10) instead of Equation (2.25), which would enhance the dipole spin-down and mass-loss resulting in a lower initial disc mass.

Table 3.6: AICc values for fits to the SGRB sample with extended emission with varying p values and $n = 1$ and data < 10 s excluded. Values in **bold** are the minimum value for each GRB. *GRB 061210 has fewer data points than free parameters resulting in a negative AICc value which was not considered when choosing the best fit.

GRB	$p = 6$	$p = 7$	$p = 8$	$p = 9$
050724	1,526	1,173	1,305	1, 138
051016B	263	198	213	144
051227	51	52	59	60
060614	45,153	42,746	43,416	42, 656
061006	208	91.3	136	91.1
061210	-35*	509	94	279
070714B	175	204	204	234
071227	91	142	98	119
080123	426	431	387	609
080503	2,333	2, 323	2,336	2,345
100212A	8,067	7, 859	8,168	7,862
100522A	7,464	6, 335	6,461	6,349
111121A	859	858	854	795
150424A	264	241	255	336
160410A	202	192	184	170

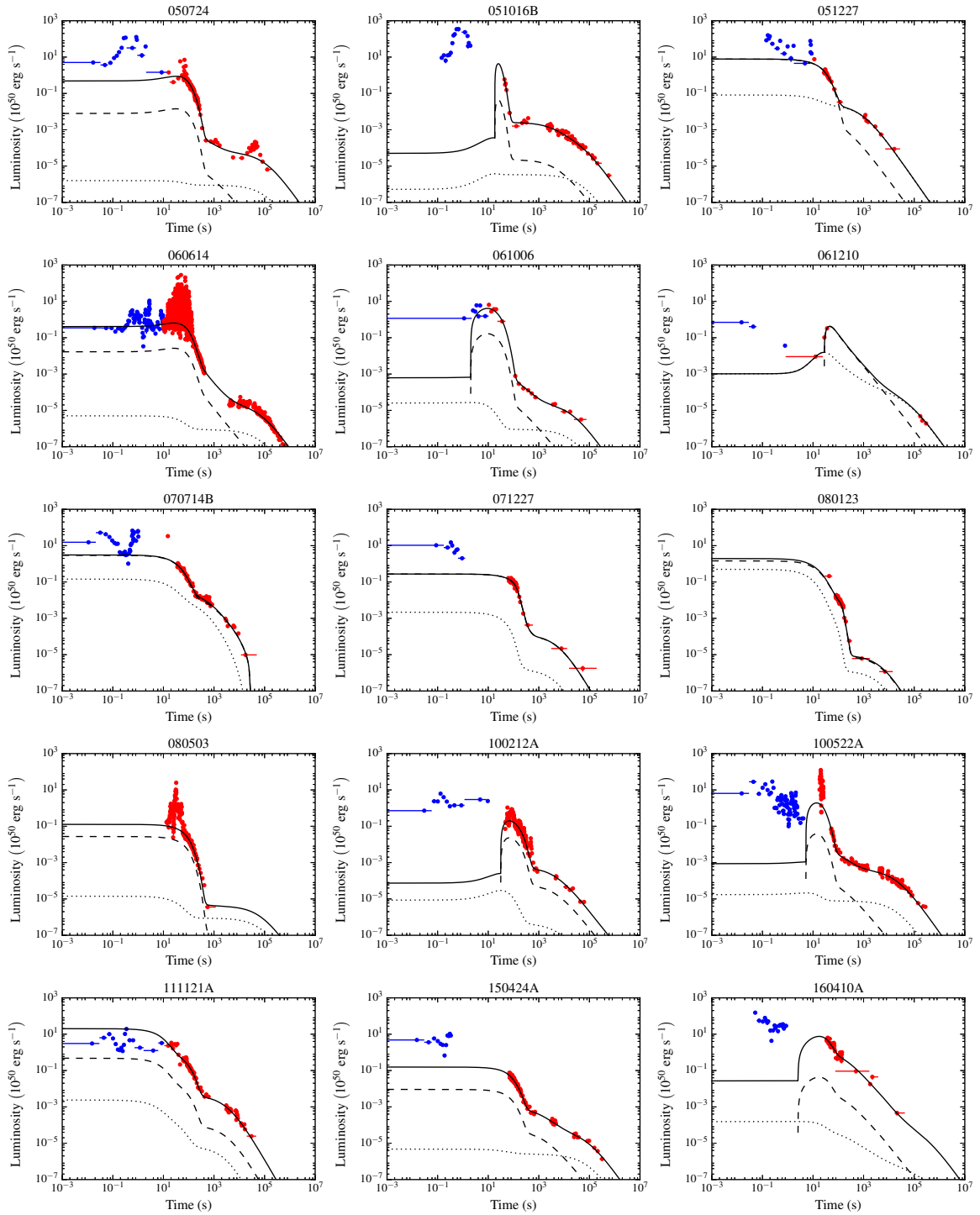


Figure 3.6: Global best fit models produced from fitting to the SGRB sample with extended emission for $n = 1$ and excluding data < 10 s (bold values in Table 3.6). Solid, black line - total luminosity; dashed, black line - propeller luminosity; dotted, black line - dipole luminosity. Points are combined BAT and XRT data: red points have been included in the fitting, blue points were excluded.

Table 3.7: Parameters derived from the best fitting models to the SGRB sample with extended emission for $n = 1$ and excluding data $< 10s$. Uncertainties represent a 95% confidence interval. Values marked with an [L] are a parameter limit; those marked with an [F] were fixed during fitting. χ^2_ν values are shown to indicate goodness of fit. *GRB 061210 has fewer data points than free parameters resulting in a negative χ^2_ν value.

GRB	B ($\times 10^{-15}$ G)	P_i (ms)	$M_{D,i}$ ($\times 10^{-2} M_\odot$)	R_D (km)	ϵ	δ	η_{dip} (%)	η_{prop} (%)	$1/f_B$	χ^2_ν
050724	$1.82^{+0.57}_{-0.43}$	$7.51^{+2.07}_{-1.65}$	$0.55^{+0.21}_{-0.16}$	408^{+9}_{-9}	$11.57^{+15.66}_{-10.59}$	$(10.00^{+8.12}_{-3.63}) \times 10^{-4}$	2^{+1}_{-1}	74^{+25}_{-34}	62^{+69}_{-26}	5
051016B	$1.74^{+1.37}_{-0.69}$	$8.95^{+1.01}_{-3.17}$	$4.27^{+5.20}_{-2.99}$	60^{+4}_{-4}	$781.19^{+196.60}_{-249.72}$	$(1.93^{+1.53}_{-0.89}) \times 10^{-3}$	1[L]	88^{+11}_{-30}	96^{+184}_{-60}	2
051227	$2.38^{+1.05}_{-0.43}$	$0.76^{+0.07}_{-0.06}$	$9.51^{+0.46}_{-1.36}$	178^{+23}_{-40}	[U]	$(0.04^{+2.62}_{-0.04}) \times 10^{-1}$	5[F]	40[F]	1	2
060614	$3.43^{+0.24}_{-0.24}$	$8.37^{+0.53}_{-0.50}$	$1.37^{+0.30}_{-0.22}$	356^{+4}_{-4}	$0.12^{+0.09}_{-0.02}$	$(5.07^{+0.88}_{-1.60}) \times 10^{-2}$	2^{+1}_{-1}	66^{+33}_{-34}	24^{+26}_{-9}	19
061006	$9.39^{+0.59}_{-1.59}$	$8.50^{+1.44}_{-3.02}$	$4.53^{+4.99}_{-2.66}$	98^{+7}_{-9}	$8.60^{+15.43}_{-8.33}$	$(2.11^{+9.14}_{-0.73}) \times 10^{-4}$	2^{+2}_{-1}	74^{+25}_{-41}	25^{+22}_{-14}	7
061210	$1.90^{+0.59}_{-0.89}$	$3.64^{+5.92}_{-2.45}$	$2.91^{+6.66}_{-2.42}$	127^{+156}_{-70}	$0.20^{+1.23}_{-0.09}$	$8.95^{+37.10}_{-7.31}$	51^{+46}_{-43}	33^{+54}_{-23}	1[F]	-42*
070714B	$6.88^{+0.87}_{-1.85}$	$1.12^{+0.12}_{-0.15}$	$7.21^{+1.47}_{-0.89}$	328^{+22}_{-21}	$24.29^{+15.03}_{-6.90}$	$(2.22^{+0.24}_{-0.23}) \times 10^{-1}$	5[F]	40[F]	1[F]	2
071227	$5.36^{+1.38}_{-1.09}$	$2.82^{+0.30}_{-1.17}$	$4.28^{+3.87}_{-2.81}$	1181^{+783}_{-1126}	$52.92^{+684.66}_{-45.61}$	$31.73^{+17.34}_{-22.00}$	5[F]	40[F]	1[F]	3
080123	$9.73^{+0.26}_{-1.72}$	$1.45^{+2.19}_{-0.17}$	$8.57^{+1.38}_{-6.29}$	176^{+1486}_{-20}	$319.24^{+181.28}_{-279.28}$	$8.63^{+27.57}_{-3.12}$	24^{+56}_{-22}	10^{+5}_{-7}	1[F]	9
080503	$4.82^{+0.46}_{-0.44}$	$9.42^{+0.56}_{-2.06}$	$1.36^{+0.89}_{-0.31}$	367^{+13}_{-13}	[U]	$(4.31^{+56.68}_{-3.24}) \times 10^{-5}$	5[F]	40[F]	5^{+1}_{-2}	9
100212A	$4.17^{+0.10}_{-0.10}$	$9.93^{+0.06}_{-0.27}$	$9.91^{+0.09}_{-0.38}$	560^{+9}_{-9}	$81.35^{+21.75}_{-16.35}$	$(1.08^{+0.20}_{-0.15}) \times 10^{-2}$	5[F]	40[F]	$8.6^{+0.4}_{-0.3}$	21
100522A	$5.87^{+0.70}_{-0.57}$	$9.90^{+0.09}_{-0.35}$	$1.77^{+0.60}_{-0.45}$	83^{+3}_{-2}	$12.28^{+6.02}_{-4.98}$	$(1.84^{+0.30}_{-0.23}) \times 10^{-3}$	5[F]	40[F]	51^{+12}_{-10}	37
111121A	$9.76^{+0.23}_{-0.80}$	$6.12^{+1.15}_{-0.55}$	$9.20^{+0.77}_{-2.23}$	428^{+17}_{-17}	$83.37^{+14.45}_{-11.29}$	$10.34^{+1.43}_{-1.38}$	37^{+59}_{-34}	42^{+54}_{-32}	42^{+129}_{-24}	7
150424A	$2.48^{+0.66}_{-0.78}$	$8.89^{+1.06}_{-2.87}$	$0.23^{+0.19}_{-0.05}$	468^{+20}_{-20}	$32.04^{+11.14}_{-9.15}$	$(7.02^{+1.06}_{-1.01}) \times 10^{-2}$	5[F]	40[F]	17^{+5}_{-9}	2
160410A	$4.69^{+4.72}_{-1.84}$	$7.94^{+1.98}_{-4.75}$	$1.89^{+6.24}_{-1.57}$	150^{+45}_{-27}	$11.86^{+7.45}_{-6.34}$	$(1.80^{+1.43}_{-0.82}) \times 10^{-1}$	29^{+67}_{-27}	47^{+50}_{-39}	175^{+373}_{-145}	4

Table 3.8: AICc values for fits to the SGRB sample with extended emission excluding data < 10 seconds and using Equation (2.25) for the dipole torque. **Bold** values are the minima. *GRB 061210 has fewer data points than free parameters and so these statistics should be treat with caution.

GRB	$p = 6$	$p = 7$	$p = 8$	$p = 9$
050724	1,327	1,418	1,206	1,187
051016B	312	173	281	146
051227	55	48	61	93
060614	45,783	43,317	42,836	43,184
061006	109	98	106	92
061210*	348	447	50	71
070714B	179	233	180	306
071227	101	87	88	91
080123	440	254	292	276
080503	2,338	2,307	2,291	2,328
100212A	8,373	8,131	8,369	6,639
100522A	7,859	6,111	6,929	5,825
111121A	859	618	880	604
150424A	337	262	245	255
160410A	225	185	1,964	216

3.4.5 Refitting with Enhanced Dipole Torque

For direct comparison with Gompertz et al. (2014), the sample was fitted once more using the enhanced dipole torque in Equation (2.25) (Bucciantini et al., 2006) for $n = 1$ and $p = 6, 7, 8$ and 9. The AICc values for the fits are presented in Table 3.8, the best fits from this table are shown in Fig. 3.7, and the parameters derived from those fits are presented in Table 3.9.

Including Equation (2.25) in the model provides a marginal improvement in fitting, *e.g.*, the tail of GRB 060614 is matched more closely in Fig. 3.7 than Fig. 3.6, though in some cases it performs

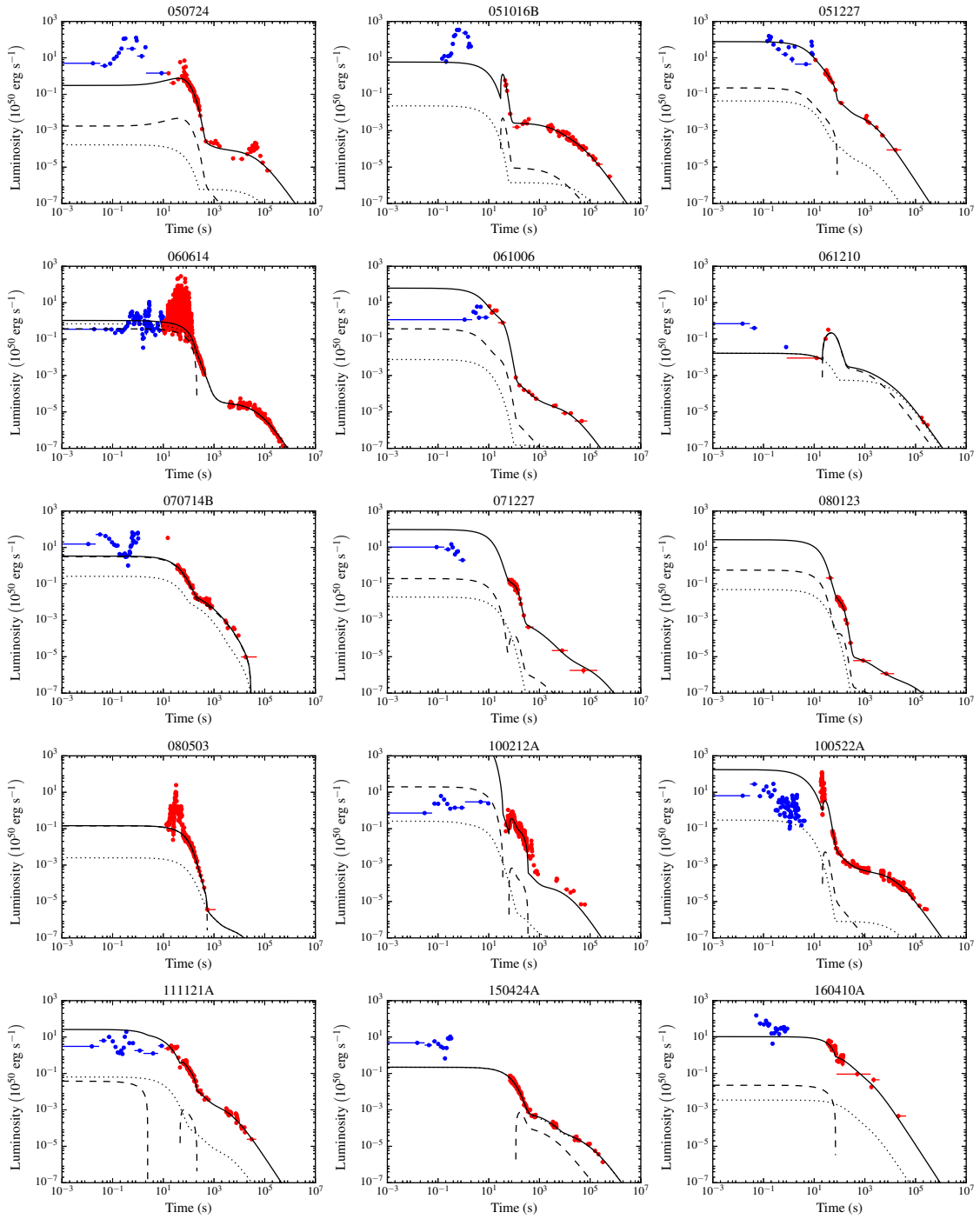


Figure 3.7: The results of fitting to the SGRB sample with extended emission for the best global fits (bold values in Table 3.8) excluding data < 10 s and using Equation (2.25) for the dipole torque. Solid, black line - total luminosity; dashed, black line - propeller luminosity; dotted, black line - dipole luminosity. Data points are combined BAT and XRT data: blue points have been excluded from the fit, red points were included.

Table 3.9: Parameters derived from fits to SGRB sample with extended emission for the globals fits (bold values in Table 3.8) excluding data < 10s and using Equation (2.25) for the dipole torque and the χ^2_ν goodness of fit statistic. Uncertainties are a 95% confidence interval and values marked with an [L] are a parameter limit. *GRB 061210 has fewer data points than parameters resulting in a negative χ^2_ν value.

GRB	B ($\times 10^{15}$ G)	P_i (ms)	$M_{D,i}$ ($\times 10^{-2} M_\odot$)	R_D (km)	ϵ	δ	η_{dip} (%)	η_{prop} (%)	$1/f_B$	χ^2_ν
050724	$1.45^{+0.13}_{-0.11}$	$9.93^{+0.07}_{-0.30}$	$0.21^{+0.03}_{-0.03}$	402^{+8}_{-8}	$1.65^{+14.66}_{-1.53}$	$(7.31^{+33.06}_{-6.34}) \times 10^{-4}$	1[L]	99^{+1}_{-4}	156^{+17}_{-18}	5
051016B	$1.27^{+0.45}_{-0.39}$	$9.10^{+0.86}_{-2.71}$	$6.56^{+3.24}_{-4.01}$	55^{+4}_{-4}	$833.98^{+155.69}_{-262.79}$	$(6.47^{+6.13}_{-3.06}) \times 10^{-4}$	1[L]	85^{+14}_{-35}	254^{+175}_{-129}	2
051227	$8.49^{+1.43}_{-2.84}$	$7.01^{+2.86}_{-3.95}$	$1.75^{+7.17}_{-1.10}$	92^{+126}_{-40}	$192.68^{+159.04}_{-161.84}$	$3.62^{+8.64}_{-3.56}$	5[F]	40[F]	291^{+263}_{-222}	2
060614	$5.10^{+0.24}_{-0.58}$	$2.07^{+0.16}_{-0.23}$	$6.00^{+1.09}_{-0.50}$	1526^{+60}_{-56}	$380.59^{+25.37}_{-23.89}$	$2.73^{+0.18}_{-0.13}$	92^{+8}_{-26}	38^{+15}_{-6}	1[F]	19
061006	$9.56^{+0.43}_{-1.25}$	$8.38^{+1.54}_{-2.92}$	$1.49^{+1.27}_{-0.42}$	91^{+8}_{-13}	$5.32^{+15.52}_{-5.18}$	$(1.30^{+8.04}_{-0.62}) \times 10^{-4}$	1[L]	89^{+11}_{-26}	168^{+81}_{-77}	7
061210	$0.18^{+0.21}_{-0.02}$	$0.72^{+0.47}_{-0.03}$	$2.26^{+1.00}_{-0.47}$	223^{+92}_{-56}	$78.96^{+809.05}_{-78.77}$	$(5.56^{+47.26}_{-5.56}) \times 10^{-2}$	1[L]	$98.5^{+1.5}_{-6.8}$	1[F]	-27*
070714B	$2.84^{+0.33}_{-0.66}$	$1.01^{+0.04}_{-0.06}$	$7.43^{+2.28}_{-1.22}$	320^{+21}_{-20}	$25.42^{+17.54}_{-7.43}$	$(1.96^{+0.22}_{-0.21}) \times 10^{-1}$	5[F]	40[F]	1[F]	2.1
071227	$8.79^{+0.92}_{-2.22}$	$7.03^{+2.79}_{-3.41}$	$1.71^{+2.07}_{-0.50}$	237^{+21}_{-20}	$21.40^{+29.93}_{-21.21}$	$(7.45^{+27.30}_{-3.51}) \times 10^{-4}$	5[F]	40[F]	449^{+144}_{-307}	2
080123	$8.92^{+1.04}_{-2.41}$	$4.06^{+1.48}_{-1.89}$	$2.67^{+3.48}_{-0.84}$	234^{+8}_{-7}	$56.84^{+71.22}_{-52.33}$	$(1.11^{+0.62}_{-0.36}) \times 10^{-4}$	5[F]	40[F]	43^{+25}_{-31}	5
080503	$4.92^{+1.30}_{-0.98}$	$5.30^{+0.64}_{-1.61}$	$1.64^{+0.96}_{-0.35}$	991^{+126}_{-118}	$138.98^{+771.43}_{-131.51}$	$1.67^{+9.08}_{-1.48}$	2^{+3}_{-1}	80^{+19}_{-42}	1[F]	9
100212A	$9.96^{+0.04}_{-0.15}$	$1.28^{+0.83}_{-0.02}$	$9.90^{+0.10}_{-3.93}$	135^{+6}_{-2}	$990.37^{+9.25}_{-39.59}$	$(2.12^{+1.29}_{-0.10}) \times 10^{-1}$	1[L]	87^{+12}_{-14}	511^{+83}_{-73}	18
100522A	$9.98^{+0.02}_{-0.09}$	$6.72^{+0.58}_{-0.70}$	$6.91^{+0.47}_{-0.35}$	50[L]	$0.21^{+0.66}_{-0.11}$	$0.03^{+0.02}_{-0.02}$	$5.7^{+0.3}_{-0.3}$	98^{+2}_{-7}	587^{+13}_{-40}	34
111121A	$6.75^{+0.94}_{-1.89}$	$8.13^{+1.79}_{-3.92}$	$2.76^{+3.76}_{-0.74}$	153^{+11}_{-10}	$265.32^{+34.38}_{-31.01}$	$1.08^{+0.11}_{-0.11}$	10^{+6}_{-6}	62^{+36}_{-39}	255^{+299}_{-185}	5
150424A	$0.85^{+0.28}_{-0.27}$	$5.03^{+0.88}_{-1.43}$	$3.68^{+3.25}_{-1.04}$	470^{+33}_{-37}	$43.37^{+12.69}_{-9.36}$	$(6.36^{+2.22}_{-2.13}) \times 10^{-2}$	76^{+24}_{-42}	10^{+20}_{-8}	1[F]	2
160410A	$2.71^{+0.48}_{-0.88}$	$7.15^{+2.31}_{-3.87}$	$0.82^{+4.17}_{-0.55}$	549^{+1284}_{-496}	$20.68^{+210.20}_{-16.01}$	$21.26^{+26.83}_{-17.08}$	5[F]	40[F]	403^{+188}_{-317}	4

much worse, *e.g.*, GRB 100212A. The initial disc mass $M_{D,i}$ only approaches the upper limit for GRB 100212A and indicates more moderate results across the rest of the sample. This is a reflection of the enhanced energy output facilitated by Equation (2.25). Equation (2.25) does not produce a dramatic change in the morphology or energetics of the fits, nor does it significantly improve the fit statistics. However, the derived disc masses are more broadly in line with previous work (*e.g.*, Rosswog 2007).

3.4.6 The B-P Landscape

Fig. 3.8 shows where the results of this work fall in relation to other GRBs in both the long and short classifications. It needs to be noted that the results from Gompertz et al. (2014) used fixed efficiencies of $\eta_{\text{dip}} = 5\%$ and $\eta_{\text{prop}} = 40\%$, whereas the work done in Rowlinson et al. (2013) uses 100% efficiency instead, and my efficiencies have been free parameters in most fitting procedures. Also, Gompertz et al. (2014) used Equation (2.25) which enhances the dipole spin-down and so these results appear to occupy their own region of low magnetic field and spin period. Hence, conclusions drawn from this plot require some caution.

However, Fig. 3.8 does show that my results occupy a region of moderate to high magnetic field and spin period, indicating that the fallback accretion relaxes the constraints on the initial spin of the magnetar (*i.e.*, it does not need to be born near the break-up period) since it will be spun-up by the fallback regardless. Though this result could be due to either the addition of a $t^{-\frac{5}{3}}$ fallback accretion profile or my inclusion of beaming as a fitting parameter. The results of this work still do not approach the same same region as Gompertz et al. (2014) even when early-time, high luminosity data is excluded and Equation (2.25) is used which consolidates that the shift in B - P parameter space is due to the inclusion of fallback accretion.

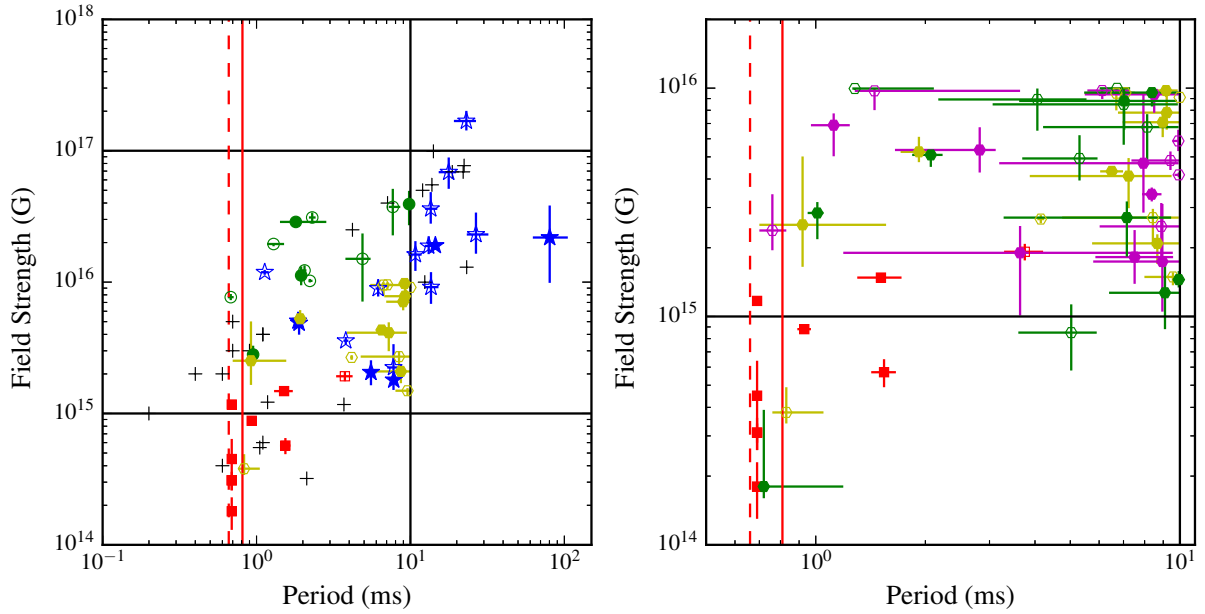


Figure 3.8: Plots of magnetic field strength versus initial spin period. The solid (dashed) red line represents the break-up period for a collapsar (binary merger) progenitor (Lattimer & Prakash, 2004). **Left panel** - blue stars: stable magnetars and green circles: unstable magnetars which collapse to form a black hole (Rowlinson et al., 2013). Black '+' symbols are the LGRB candidates identified by Lyons et al. (2010) and Dall'Osso et al. (2011). Red squares (both panels) show the values found in Gompertz et al. (2014). Yellow hexagons (both panels) represent the magnetic fields and initial spin periods of this work for the global best fit values in Table 3.5. **Right panel** - magenta hexagons are the B and P_1 values for fits excluding data < 10 s in Table 3.7; green hexagons are B and P_1 values for fits excluding data < 10 s and including Equation (2.25) in Table 3.9. Filled symbols have observed redshifts, open symbols use the sample average redshift, which is $z = 0.39$ for extended bursts and $z = 0.72$ for the short bursts from Rowlinson et al. (2013).

3.5 Conclusions

I used an MCMC to fit the modified magnetar propeller model with fallback accretion to a sample of short GRBs exhibiting extended emission for a range of free parameters and “sharpness” of propeller. I have found that the parameters derived from the fits produced by the propeller model with fallback accretion are consistent with theoretical predictions for magnetars.

My model can cope with long, dipole plateaux and flare-like variability but struggles with the early-time, short-timescale variability. However, since this variability is usually present in the prompt emission which is generally attributed to internal shocks rather than magnetic acceleration of particles, it is not strictly within the remit of the model to fit it.

The addition of fallback accretion provides a noticeable improvement in matching light curves compared to those presented in Gompertz et al. (2014) and fallback accretion may play a pivotal role in explaining the features of extended emission light curves. My model uses a smoothed representation of fallback disc feeding as a simplest case scenario. A more “clumpy” representation could potentially be more physical and useful to explain phenomena such as flares (Dall’Osso et al., 2017).

4

Fallback Accretion on to a Newborn Magnetar: Long GRBs with Giant X-ray Flares

The work presented in this chapter was published in Gibson et al. (2018).

Abstract

Flares in the X-ray afterglow of gamma-ray bursts (GRBs) share more characteristics with the prompt emission than the afterglow, such as pulse profile and contained fluence. As a result, they are believed to originate from late-time activity of the central engine and can be used to constrain the overall energy budget. In this chapter, a sample of 19 long GRBs observed by *Swift*-XRT that contain giant flares in their X-ray afterglows has been collected. I fit this sample with a version of the magnetar propeller model, modified to include fallback accretion. This model has already successfully reproduced extended emission in short GRBs. The best fits provide a reasonable morphological match to the light curves. However, 15 out of 19 of the fits require efficiencies for the propeller mechanism that approach 100%. The high efficiency parameters are a direct result of the high energy contained in the flares and the extreme duration of the dipole component, which forces either slow spin periods or low magnetic fields. I find that even with the inclusion of significant fallback accretion, in all but a few cases it is energetically challenging to produce prompt emission, afterglow and giant flares within the constraints of the rotational energy budget of a magnetar.

4.1 Introduction

As discussed in Section 1.1.3, the launch of the *Swift* satellite in 2004 (Gehrels et al., 2004) facilitated a break-through in our understanding of GRB physics thanks to its rapid slewing capabilities allowing early and well-sampled observations of afterglows by the X-ray Telescope (XRT) (Burrows et al., 2005a). This led to the formation of a ‘canonical’ X-ray afterglow model consisting of the following phases (Nousek et al., 2006; O’Brien et al., 2006) (see Section 1.4.4): (i) a steep, early decay; (ii) a plateau; (iii) a late decay; (iv) achromatic jet breaks; and (v) flares. Phases (iv) and (v) do not always have to be present and flares are often superposed onto the plateau phase (Curran et al., 2008).

Flares are a dramatic re-brightening in the X-ray light curve that are seen $\sim 30 - 10^5$ seconds

after the burst trigger (Burrows et al., 2005b; Beniamini & Kumar, 2016) and are observed in approximately half of all GRBs detected by *Swift*-XRT (O’Brien et al., 2006; Curran et al., 2008; Swenson & Roming, 2014). Margutti et al. (2011) note that, observationally, there appears to be two different evolutions of X-ray flare luminosity with time. The average luminosity of flares occurring before $t = 1000$ s decreases as $t^{-2.7}$, while the luminosity at later times decreases as $\sim t^{-1}$. Flares are characterised by a fast rise, exponential decay profile. The fluence of the largest flares (so-called giant flares) is often comparable to the prompt emission, potentially indicating a common origin between the two (Chincarini et al., 2010). The presence of an underlying continuum that is unaffected by the flare (*i.e.*, the superposition of the flare on the plateau phase) indicates that the flares do not share an emission site with the afterglow (Chincarini et al., 2010), which is believed to be produced by the deceleration of forward shocks in the ambient medium. GRB 050502B contains the first and the largest flare to be observed, re-brightening by a factor of ~ 500 above the continuum (Falcone et al., 2006). The additional energy release observed in giant flares like the one seen in GRB 050502B provide a unique test to constrain the energy budget of GRBs.

There are a variety of models which have been suggested to explain the origin of flares, including: ‘patchy’ shells (Mészáros et al., 1998; Kumar & Piran, 2000); refreshed shocks (Rees & Mészáros, 1998; Zhang & Mészáros, 2002); and density fluctuations (Wang & Loeb, 2000; Dai & Lu, 2002). The continued central engine activity model (Dai & Lu, 1998; Zhang & Mészáros, 2002) is often favoured, since the characteristics of flares are similar to the prompt emission (Chincarini et al., 2010). The new-born millisecond magnetar is a concept that is competing with black holes as the source of power in GRBs, mainly due to its potential as a naturally long-lived central engine (see Bernardini 2015 for a review). In the magnetar model, the rotational energy of a highly-magnetised neutron star is tapped via interactions between its intense dipole field and the circumstellar environment (see Zhang & Mészáros, 2001). This model has been successfully applied to short (Metzger et al., 2008; Gompertz et al., 2013; Rowlinson et al., 2013) and long GRBs (Lyons et al., 2010). However, it has a strict energy upper limit imposed by the rotational energy reservoir of the neutron star. This is typically assumed to be $\approx 3 \times 10^{52}$ ergs for a $1.4 M_{\odot}$ neutron star with a 1 ms spin period. The magnetar is expected to be spun down very rapidly

during the prompt emission phase, thereby decreasing the amount of energy available to power a flare (Beniamini & Kumar, 2016). However, fallback accretion may augment the magnetar energy budget, as it provides a mechanism to spin the magnetar back up. Recent work by Beniamini et al. (2017) and Metzger et al. (2018) suggests that the extractable energy from an isolated magnetar usable in a GRB is even further reduced. They predict for the same neutron star, the limit would be $\sim 2 \times 10^{51}$ erg making the need for fallback accretion even more severe.

In this chapter, I investigate whether flares can be powered by the delayed on-set of a propeller regime (Piro & Ott, 2011; Gompertz et al., 2014), in which in-falling material is accelerated to super-Keplerian velocities via magneto-centrifugal slinging and is ejected from the system. A magnetic propeller provides a path to a smoother emission profile than can be achieved by direct accretion onto a compact object, matching the phenomenology of giant flares more closely. I maximise the available energy reservoir by feeding the disc with fallback accretion, which was successfully used to match the light curves of short GRBs with extended emission in Gibson et al. 2017, following models such as Ekşi et al. (2005); Rosswog (2007); Kumar et al. (2008); Cannizzo et al. (2011); Parfrey et al. (2016).

I introduce the sample of long GRBs (LGRBs) with significant X-ray flares in Section 4.2. In Section 4.3, I briefly review the optimisation routine used in Section 3.3 and Gibson et al. (2017) and I present the results and discussion of the optimisation procedure in Section 4.4. I summarise my conclusions in Section 4.5.

4.2 Sample of *Swift* LGRBs with Giant X-ray Flares

I have chosen a sample of 19 LGRBs that exhibit significant flares in their X-ray afterglows to study. Since there is no consistent definition of a giant X-ray flare, I selected which LGRBs to study based on the sample rate of data through the duration of the flare. I require good data coverage near the peak of the flare and a reasonable constraint on the amplitude of the flare so that the optimisation routine can properly constrain the free parameters, as such a prominent feature

will drive the morphology of the fit.

The data were collected by *Swift*-XRT (Gehrels et al., 2004; Burrows et al., 2005a) and were processed by the UK *Swift* Science Data Centre (UKSSDC¹; Evans et al. 2007, 2009). As in Section 3.2 and Gibson et al. (2017), the data underwent a cosmological k -correction (Bloom et al., 2001) in order to produce bolometric, rest-frame light curves and were corrected for absorption using values in Table 4.1. For those GRBs with no observed redshift, the mean of the sample in Salvaterra et al. (2012) was used (*i.e.*, $z = 1.84$).

4.3 Optimisation Routine

As in Section 3.3 and Gibson et al. (2017), I implement a Markov chain Monte Carlo (MCMC) simulation package (Foreman-Mackey et al., 2013) to find the optimal values for the 9 free model parameters: B - magnetic field strength of the magnetar; P_i - spin period of the magnetar; $M_{D,i}$ - disc mass; R_D - disc radius; ϵ - fallback timescale fraction; δ - fallback mass budget fraction; η_{dip} - dipole energy to luminosity conversion efficiency; η_{prop} - propeller energy to luminosity conversion efficiency; and $1/f_B$ - beaming fraction. These parameters are defined after the prompt phase has ceased, which has been arbitrarily chosen to be $t = 1$ s. Again, I used 200 “walkers” taking 50,000 steps each and constructed a posterior probability distribution (see Eq. 2.28) from a Gaussian log-likelihood function (Eq. 2.26) and a flat prior function (Eq. 2.27), using the parameter limits given in Table 3.2, and implementing the *Python* module *emcee* to handle the MCMC simulation (Foreman-Mackey et al., 2013). An ordinary differential equation integrator solves the equation set in Section 2.2 to return the disc mass, M_D , and magnetar angular frequency, ω , over a time period, from which the total luminosity can be calculated. Fixed parameters are the viscosity prescription, $\alpha = 0.1$; the speed of sound in the accretion disc, $c_s = 10^7$ cm s⁻¹; the ratio $r_m/r_{\text{lc}} = 0.9$, which prevents ejected material from exceeding the speed of light; and the dimensionless parameter $n = 1$, which controls how rapidly the propeller emission becomes dominant.

¹www.swift.ac.uk

Table 4.1: The parameters required to perform a cosmological k -correction as described by Bloom et al. (2001). Γ is the photon index; σ is the absorption coefficient calculated from the ratio of counts-to-flux (unabsorbed) to counts-to-flux (absorbed); and z is the redshift given in the literature. For those GRBs with no observed redshift (marked with an *), the mean of the sample in Salvaterra et al. (2012) was used. ^aAfonso et al. (2011); ^bMirabal & Halpern (2006); ^cBerger & Gladders (2006); ^dFugazza et al. (2006); ^eBloom et al. (2006); ^fPenacchioni et al. (2013); ^gCabrera Lavers et al. (2011); ^hElliott et al. (2014); ⁱTanvir et al. (2016).

GRB	Γ	σ	z
050502B	$1.907^{+0.125}_{-0.098}$	1.11	5.2 ^a
060124	$1.91^{+0.06}_{-0.05}$	1.28	2.297 ^b
060526	$1.98^{+0.17}_{-0.12}$	1.15	3.21 ^c
060904B	$2.05^{+0.15}_{-0.15}$	1.49	0.703 ^d
060929	$3.5^{+1.0}_{-1.4}$	5.79	1.84*
061121	$1.82^{+0.06}_{-0.06}$	1.23	1.314 ^e
070520B	$2.5^{+0.8}_{-0.6}$	1.70	1.84*
070704	$2.3^{+0.5}_{-0.4}$	3.15	1.84*
090621A	$2.09^{+0.26}_{-0.25}$	2.42	1.84*
100619A	$2.30^{+0.16}_{-0.15}$	2.19	1.84*
110709B	$2.01^{+0.06}_{-0.06}$	1.38	0.75 ^f
110801A	$1.99^{+0.11}_{-0.10}$	1.25	1.858 ^g
110820A	$2.5^{+0.6}_{-0.5}$	2.62	1.84*
121123A	$1.85^{+0.11}_{-0.11}$	1.17	1.84*
121217A	$1.97^{+0.11}_{-0.11}$	1.66	3.1 ^h
140817A	$1.803^{+0.103}_{-0.100}$	1.30	1.84*
141031A	$1.85^{+0.32}_{-0.16}$	1.31	1.84*
141130A	$2.0^{+0.4}_{-0.3}$	1.15	1.84*
160425A	$2.47^{+0.20}_{-0.19}$	2.19	0.555 ⁱ

4.4 Results and Discussion

The best fits of the magnetar propeller with fallback accretion model to the LGRB giant flare sample are presented in Fig. 4.1. The model provides a reasonable fit to the morphology of the data across the sample, recreating the height and shape of the flare and fitting the emission ‘tail’ in 17 out of 19 GRBs. However in general terms, the model is struggling to meet the general energy budget of the sample which causes some of the parameters to be forced to the extremes of their allowed parameter space, see Table 3.5. The model consistently misses the emission preceding the flare, falling 1-2 orders of magnitude lower than the data. However, this emission is most likely the tail end of the prompt spike, which I do not fit in this chapter. The fits which performed the most poorly are to GRBs 100619A and 110801A. In the case of GRB 100619A, the model has missed the second flare entirely in favour of fitting to the first flare². Currently, the model is unable to fit multiple events like this as it does not contain an underlying flaring mechanism. Instead it describes a large release of energy that fits the general energetics of large flares. The closest approximation to multiple flares the model is currently capable of is a ‘stuttering’ type burst (see Section 2.4.1, Gompertz et al. 2014 and Gibson et al. 2017 for details of burst types). Double flares like this could be achieved using models such as ‘clumpy’ accretion (*e.g.*, Dall’Osso et al., 2017), a self-criticality regime of magnetic reconnection (similar to solar flares, *e.g.*, Wang & Dai, 2013), or modulating the fallback rate to no longer be a smooth profile. As discussed in Chapter 3 and Gibson et al. (2017) in the context of the early time prompt emission, the model struggles to replicate short-timescale variability in GRB 110801A, instead ‘smoothing’ through the main flare and the smaller, preceding flare. This is another feature that may be achievable with a ‘clumpy’ accretion model, self-critical solar flare-like activity, or a modulated fallback rate. Mass would be delivered intermittently, causing outbursts as opposed to the smooth feeding currently modelled here.

The parameter values derived from the best-fitting models are presented in Table 4.2. Across the sample, I have generally found low magnetic fields and slow initial spin periods, indicating that

²GRB 100619A exhibits a double flare which is most obvious in the joint BAT and XRT light curve from the UKSSDC’s Burst Analyser found here: http://www.swift.ac.uk/burst_analyser/424998.

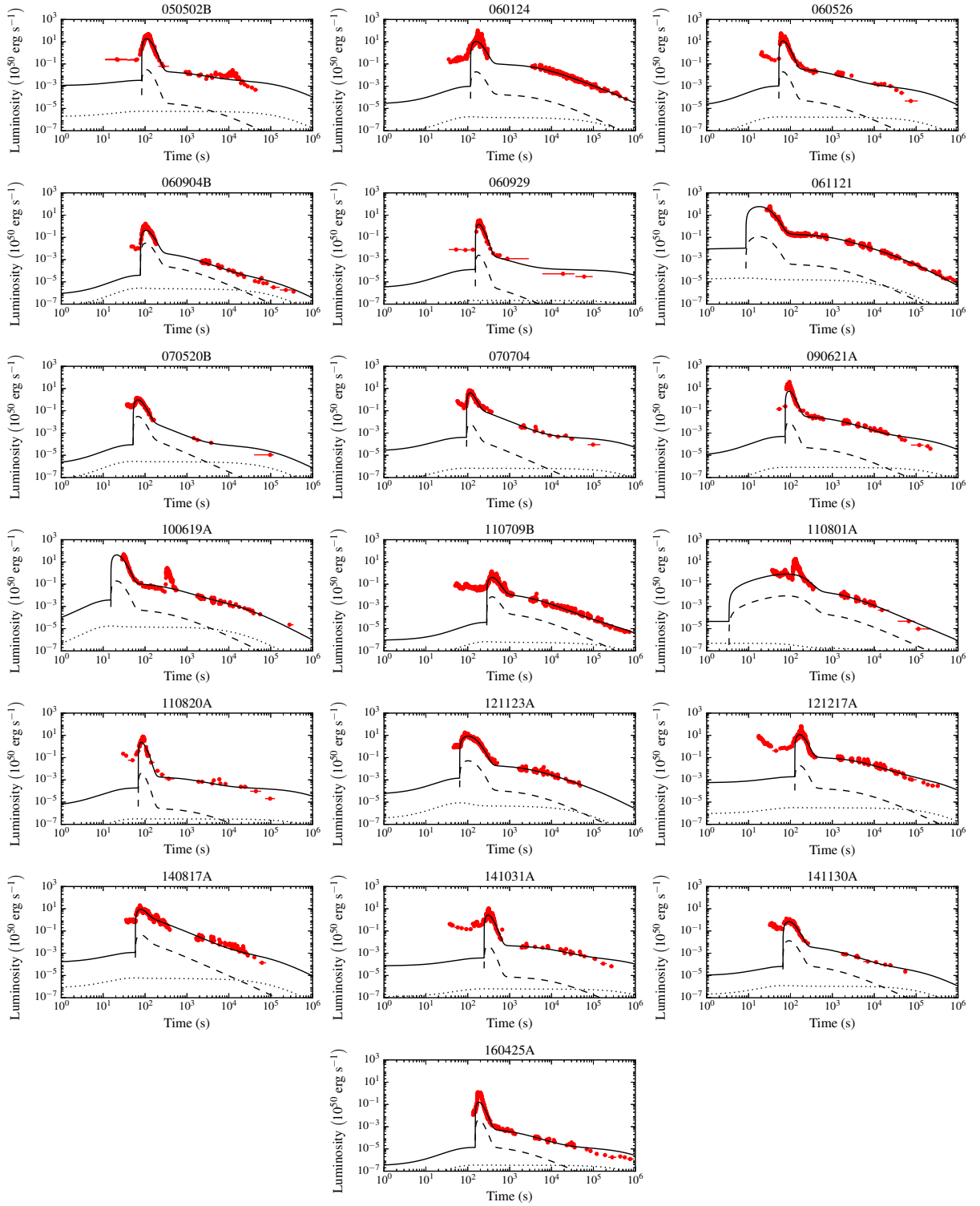


Figure 4.1: Fits of magnetar propeller model with fallback accretion to LGRB with X-ray flare sample. Red points are *Swift*-XRT data; solid, black line - total luminosity; dashed, black line - propeller luminosity; dotted, black line - dipole luminosity.

the propeller mechanism would not be that strong. A low B -field and fast spin period, or a high B -field and slow spin period have previously been shown to be necessary for an effective propeller (Rowlinson et al., 2013; Gompertz et al., 2014; Gibson et al., 2017). The driving factor behind these parameters is likely to be the duration of the dipole emission. The plateau duration is given by (cf. Zhang & Mészáros, 2001):

$$T_{\text{em}} = 10^3 I_{45} B_{\text{p},15}^{-2} P_{\text{i},0}^2 R_{10}^{-6} \text{ s}, \quad (4.1)$$

where I_{45} is the moment of inertia of the neutron star in units of 10^{45} g cm^2 , $B_{\text{p},15}$ is the dipole field strength in units of 10^{15} G , $P_{\text{i},0}$ is the spin period in ms and R_{10}^{-6} is the neutron star radius in units of 10 km. The dipole emission in the sample typically lasts $\sim 10^5 \text{ s}$, and assuming $I_{45} = R_{10}^{-6} = 1$, this requires $B_{\text{p},15}^{-2} P_{\text{i},0}^2 \approx 100$. From this it can clearly be seen that either B must be low, P must be high, or a combination of the two.

The left panel of Fig. 4.2 shows where the LGRB giant flare sample lies on the spin period-magnetic field plane. 13 GRBs are clustered against the 10 ms upper parameter limit and the majority of the sample have a magnetic field of the order of $1 \times 10^{15} \text{ G}$ or less, which are consistent with the theoretical predictions for a magnetar (Giacomazzo & Perna, 2013; Mereghetti et al., 2015; Rea et al., 2015). The right panel shows where the sample lies in energy space as a fraction of the initial spin energy. The cluster of 8 GRBs at the top of the plot all have low B -fields, $\lesssim 1 \times 10^{15} \text{ G}$, and slow spin periods, $\simeq 10 \text{ ms}$, one of the necessary conditions for an effective propeller.

Since $E \propto P_{\text{i}}^{-2}$, initial spin periods of $\sim 10 \text{ ms}$ reduce the total available energy by a factor of 100. Conversely, in most cases the efficiency of the propeller η_{prop} is forced to 100 per cent, likely in order to compensate for the low total available energy in the model. The mean beaming factor is 352, translating into a jet opening angle of $\theta_{\text{j}} \approx 4.32^\circ$. This narrow beam is likely a further symptom of a system short of energy. I note at this point that alternative sources of energy which have been ignored here may also make a significant contribution and lower the energy requirements for the model. In particular, the contribution of the synchrotron emission from the afterglow as the forward shock driven by the initial explosion decelerates has been neglected. Reprocessing of the dipole radiation in the forward shock will also allow longer-lived afterglow

Table 4.2: Parameters derived from fits shown in Fig. 4.1 and the χ^2_{ν} goodness of fit statistic. Values marked with an [L] are a parameter limit.

GRB	B ($\times 10^{15}$ G)	P_i (ms)	$M_{D,i}$ ($\times 10^{-2} M_{\odot}$)	R_D (km)	ϵ	δ	η_{dip} (%)	η_{prop} (%)	$1/f_B$	χ^2_{ν}
050502B	$0.28^{+0.02}_{-0.01}$	$2.47^{+0.14}_{-0.12}$	$9.99^{+0.01}_{-0.04}$	216^{+1}_{-1}	$91.43^{+41.88}_{-31.64}$	$(2.76^{+0.57}_{-0.52}) \times 10^{-4}$	1[L]	100[L]	599^{+1}_{-3}	8
060124	$0.69^{+0.02}_{-0.04}$	$9.62^{+0.36}_{-1.20}$	$9.30^{+0.66}_{-0.86}$	372^{+4}_{-4}	$158.87^{+13.05}_{-12.17}$	$(7.65^{+0.49}_{-0.46}) \times 10^{-3}$	1[L]	99^{+1}_{-5}	541^{+56}_{-62}	22
060526	$0.65^{+0.01}_{-0.01}$	$9.98^{+0.02}_{-0.07}$	$9.94^{+0.06}_{-0.21}$	119^{+1}_{-1}	$63.14^{+14.37}_{-12.79}$	$(3.22^{+0.41}_{-0.38}) \times 10^{-4}$	1[L]	100[L]	594^{+5}_{-18}	22
060904B	$0.82^{+0.01}_{-0.01}$	$9.97^{+0.03}_{-0.15}$	$9.94^{+0.06}_{-0.27}$	239^{+3}_{-3}	$33.82^{+7.76}_{-6.47}$	$(1.87^{+0.21}_{-0.19}) \times 10^{-3}$	1[L]	100[L]	14^{+1}_{-1}	12
060929	$0.245^{+0.001}_{-0.001}$	$9.98^{+0.02}_{-0.10}$	10.00[L]	$270.3^{+0.2}_{-0.2}$	$12.51^{+2.23}_{-2.03}$	$(2.00^{+0.14}_{-0.14}) \times 10^{-5}$	1[L]	100[L]	600[L]	224
061121	$2.44^{+1.00}_{-0.64}$	$5.01^{+1.31}_{-0.99}$	$1.93^{+1.16}_{-0.59}$	84^{+2}_{-2}	$164.59^{+17.26}_{-19.75}$	$(2.28^{+0.37}_{-0.38}) \times 10^{-2}$	2^{+2}_{-1}	86^{+13}_{-33}	491^{+104}_{-198}	3
070520B	$0.84^{+0.04}_{-0.04}$	$9.74^{+0.25}_{-0.99}$	$9.46^{+0.52}_{-1.95}$	139^{+2}_{-2}	$2.80^{+4.30}_{-2.62}$	$(8.11^{+30.30}_{-3.01}) \times 10^{-4}$	1[L]	99^{+1}_{-5}	31^{+11}_{-4}	20
070704	$0.31^{+0.01}_{-0.01}$	$6.69^{+0.43}_{-0.37}$	10.00[L]	181^{+1}_{-1}	$4.85^{+0.96}_{-0.87}$	$(5.49^{+0.59}_{-0.51}) \times 10^{-4}$	1[L]	100[L]	600[L]	52
090621A	$0.461^{+0.002}_{-0.002}$	$9.99^{+0.01}_{-0.06}$	10.00[L]	$152.4^{+0.3}_{-0.3}$	$97.19^{+6.99}_{-6.52}$	$(5.07^{+0.17}_{-0.17}) \times 10^{-4}$	1[L]	100[L]	600[L]	90
100619A	$2.20^{+0.29}_{-0.19}$	$9.94^{+0.06}_{-0.24}$	$9.55^{+0.43}_{-1.40}$	$50.6^{+0.4}_{-0.3}$	$72.47^{+3.60}_{-3.55}$	$(1.39^{+0.09}_{-0.09}) \times 10^{-3}$	1[L]	100[L]	218^{+45}_{-16}	124
110709B	$0.41^{+0.01}_{-0.01}$	$9.86^{+0.14}_{-0.54}$	$9.66^{+0.33}_{-1.00}$	857^{+7}_{-8}	$35.70^{+1.77}_{-1.66}$	$(5.72^{+0.20}_{-0.21}) \times 10^{-3}$	1[L]	99^{+1}_{-5}	55^{+8}_{-4}	17
110801A	$1.86^{+0.20}_{-0.27}$	$9.29^{+0.68}_{-2.37}$	$0.88^{+0.52}_{-0.22}$	738^{+17}_{-16}	$22.18^{+3.51}_{-3.11}$	$(7.16^{+0.59}_{-0.51}) \times 10^{-2}$	1[L]	92^{+8}_{-25}	91^{+39}_{-43}	37
110820A	$0.34^{+0.01}_{-0.01}$	$9.99^{+0.01}_{-0.05}$	$8.93^{+0.26}_{-0.26}$	116^{+1}_{-1}	$159.16^{+38.28}_{-31.98}$	$(3.87^{+0.54}_{-0.50}) \times 10^{-5}$	1[L]	100[L]	599^{+1}_{-5}	115
121123A	$1.59^{+0.03}_{-0.05}$	$9.83^{+0.16}_{-0.68}$	$9.67^{+0.32}_{-1.31}$	352^{+4}_{-3}	$101.32^{+28.31}_{-31.22}$	$(4.12^{+0.51}_{-0.55}) \times 10^{-3}$	$1.5^{+1.2}_{-0.4}$	78^{+22}_{-33}	163^{+124}_{-41}	6
121217A	$0.25^{+0.01}_{-0.01}$	$2.85^{+0.14}_{-0.14}$	$9.99^{+0.01}_{-0.04}$	334^{+2}_{-2}	$136.64^{+8.52}_{-7.99}$	$(3.72^{+0.15}_{-0.15}) \times 10^{-3}$	1[L]	100[L]	599^{+1}_{-4}	28
140817A	$0.61^{+0.08}_{-0.05}$	$4.52^{+1.01}_{-0.53}$	$9.91^{+0.08}_{-0.38}$	170^{+4}_{-4}	$4.21^{+0.65}_{-0.64}$	$(1.31^{+0.08}_{-0.07}) \times 10^{-2}$	1[L]	98^{+2}_{-9}	195^{+33}_{-20}	10
141031A	$0.16^{+0.02}_{-0.01}$	$3.72^{+0.46}_{-0.32}$	$9.98^{+0.02}_{-0.10}$	525^{+4}_{-4}	$217.60^{+49.33}_{-41.68}$	$(4.23^{+0.68}_{-0.61}) \times 10^{-4}$	1[L]	100[L]	598^{+2}_{-7}	21
141130A	$0.93^{+0.24}_{-0.39}$	$8.32^{+1.60}_{-4.97}$	$4.18^{+5.67}_{-3.68}$	228^{+6}_{-11}	$45.62^{+52.03}_{-21.91}$	$(1.90^{+0.45}_{-0.43}) \times 10^{-3}$	1[L]	86^{+13}_{-30}	52^{+467}_{-41}	11
160425A	$0.308^{+0.003}_{-0.003}$	$9.99^{+0.01}_{-0.03}$	$9.85^{+0.15}_{-0.76}$	300^{+1}_{-1}	$57.20^{+5.80}_{-5.31}$	$(1.89^{+0.10}_{-0.09}) \times 10^{-4}$	1[L]	100[L]	39^{+5}_{-2}	110

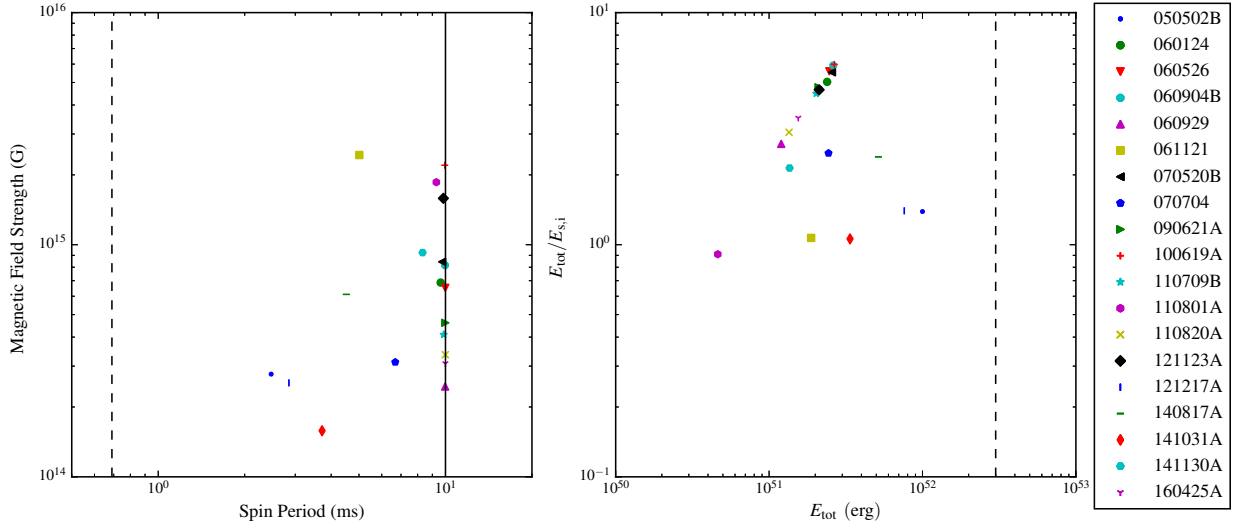


Figure 4.2: **Left panel:** A plot of the magnetic field strength, B , against the initial spin period P_i of the LGRB giant flare sample. The solid line indicates the upper limit of 10 ms and the dashed line indicates the lower, break-up limit of 0.69 ms for a collapsar (Lattimer & Prakash, 2004). Error bars were not included for clarity. **Right panel:** A plot showing the ratio of the total energy emitted to the initial spin energy, $E_{\text{tot}}/E_{s,i}$, against the total energy, E_{tot} . The total energy emitted through radiation is calculated by integrating $L_{\text{dip}} + L_{\text{prop}}$ over time of each best fit model. The initial spin energy is given by $E_{s,i} = \frac{1}{2}I\omega_i^2$, where $I = \frac{4}{5}MR^2$ is the moment of inertia of the magnetar and ω_i is the initial angular frequency. The dashed line represents the rotational energy reservoir ($\approx 3 \times 10^{52}$ ergs) for a $1.4 M_{\odot}$ neutron star with a 1 ms spin period.

emission and enable lower values of P and/or higher values of B compared to the simplified treatment of the dipole applied here (see *e.g.*, Gompertz et al., 2015). Although the relatively long initial spin periods found in the fits are primarily resultant from the need to fit the dipole emission component, I note here that they would be broadly consistent with an episode of magnetar spin down during the prompt emission phase.

The wide range of values in the fallback parameters ϵ and δ in Table 4.2 spin the magnetar up at a later period, producing a more effective propeller mechanism. I also find more initial disc masses at the upper parameter limit and with smaller disc radii, which shows that the model is attempting to extract as much energy as possible through high accretion rates to fuel the flares. The dipole and propeller efficiencies, η_{dip} and η_{prop} , are often pushed to their lowest and highest

parameter limits respectively. This is because the flares produce such large flux increases above the smooth continuum that the model can only reproduce a rise and drop-off of this magnitude by having extremely opposing efficiencies for the dipole and propeller luminosities, despite this not being observationally consistent.

Although having a mechanism with $> 50\%$ efficiency is likely unphysical and observationally inconsistent, it was found to be necessary for both efficiencies to be allowed to vary up to 100% in order for the MCMC simulation to find an acceptable fit with constrained parameters. I ran the MCMC with different combinations of upper limits on the efficiencies and the χ^2_ν values of these runs are presented in Table 4.3 along with the values for the fits in Fig. 4.1 for comparison. In each case over all the runs, the χ^2_ν value was worsened by the stricter limits on the two emission efficiency parameters. It is also shown that runs with the same value of η_{prop} find the same χ^2_ν value which suggests that the propeller emission is more important than the dipole in fitting the data and hence runs with the same limits on η_{prop} are finding similar solutions. In addition, I ran MCMC simulations that ignored the first 10 s after trigger, which is typically unconstrained by data. I found consistently poor fits, indicating that my conclusions are not dominated by the early (unconstrained) part of the light curve. The dominant limiting factor appears to be the long duration of the emission demanding extreme values of B and P , which forces the other parameters to work around them.

Table 4.4 presents the values of the Lorentz factors for the X-ray flares in the sample, Γ_X . These have been calculated using Equation (4.2), which comes from Lü et al. (2012) and Mu et al. (2016).

$$\log \Gamma_X = (2.27 \pm 0.04) + (0.34 \pm 0.03) \log L_{X,p,52} \quad (4.2)$$

where $L_{X,p,52}$ is the peak luminosity of the flare in units of $10^{52} \text{ erg s}^{-1}$.

I find that the Lorentz factor calculated from the data, $\Gamma_{X,\text{data}}$, is broadly consistent with the findings of Peng et al. (2014) where Γ_X takes values of around $\sim 60 - 150$. Whereas, the Lorentz factors calculated from the best fitting models, $\Gamma_{X,\text{model}}$, range from $\sim 20 - 160$. While this includes the range indicated by Peng et al. (2014), the values are often lower than those required by the data especially in the case of the most powerful flares, *e.g.*, GRB 060124. Since the model

Table 4.3: The χ^2_ν values for fits with different upper limits on the dipole and propeller efficiencies (η_{dip} and η_{prop} , respectively). The first column corresponds to the fits presented in Table 4.2.

GRB	χ^2_ν											
	$\eta_{\text{dip}} = 100\%$ $\eta_{\text{prop}} = 100\%$	$\eta_{\text{dip}} = 100\%$ $\eta_{\text{prop}} = 50\%$	$\eta_{\text{dip}} = 100\%$ $\eta_{\text{prop}} = 10\%$	$\eta_{\text{dip}} = 50\%$ $\eta_{\text{prop}} = 50\%$	$\eta_{\text{dip}} = 50\%$ $\eta_{\text{prop}} = 10\%$	$\eta_{\text{dip}} = 10\%$ $\eta_{\text{prop}} = 50\%$	$\eta_{\text{dip}} = 10\%$ $\eta_{\text{prop}} = 10\%$	$\eta_{\text{dip}} = 10\%$ $\eta_{\text{prop}} = 50\%$	$\eta_{\text{dip}} = 10\%$ $\eta_{\text{prop}} = 10\%$	$\eta_{\text{dip}} = 50\%$ $\eta_{\text{prop}} = 50\%$	$\eta_{\text{dip}} = 50\%$ $\eta_{\text{prop}} = 10\%$	$\eta_{\text{dip}} = 10\%$ $\eta_{\text{prop}} = 10\%$
050502B	8	58	62	58	62	58	62	58	62	58	62	62
060124	22	72	4,300	72	152	72	152	72	152	72	152	4,330
060526	22	58	63	58	63	58	63	58	63	58	63	63
060904B	11	56	234	56	235	56	235	56	235	56	235	696
060929	224	20,671	14,858	20,671	14,857	20,671	14,857	20,671	14,857	20,671	14,857	14,858
061121	3	6	15	6	15	6	15	6	15	6	15	15
070520B	20	115	110	115	110	115	110	115	110	115	110	110
070704	52	349	359	349	359	349	359	349	359	349	359	359
090621A	89	207	220	207	220	207	220	207	220	207	220	220
100619A	124	154	173	136,165	135,923	136,165	135,923	135,554	135,923	135,554	135,554	173
110709B	17	59	211	59	-	59	-	59	-	59	59	72
110801A	37	1,323	4,214	49	59	49	59	49	59	49	59	73
110820A	115	336	339	336	339	336	339	336	339	336	339	339
121123A	6	56	43	56	43	56	43	56	43	56	43	43
121217A	28	67	79	67	79	67	79	67	79	67	79	79
140817A	10	57	55	57	383	57	383	57	383	57	383	63
141031A	21	63	75	63	75	63	75	63	75	63	75	75
141130A	11	43	44	43	44	43	44	43	44	43	44	44
160425A	110	216	229	216	229	216	229	216	229	216	229	229

Table 4.4: Lorentz factor values of the X-ray flare sample, Γ_X , calculated using the $\Gamma_\gamma - E_{\gamma,\text{iso}}$ relation in Lü et al. (2012) and Mu et al. (2016). The first column corresponds to the flare Lorentz factor calculated from the *Swift* data, while the second column corresponds to the flare Lorentz factor calculated from the best fitting models. Since the model misses the second, well-defined flare in GRB 100619A, I have not provided a value of $\Gamma_{X,\text{model}}$ for it. GRBs marked with an * have no redshift and the mean of the sample in Salvaterra et al. (2012) was used.

GRB	$\Gamma_{X,\text{data}}$	$\Gamma_{X,\text{model}}$
050502B	145.75 ± 0.56	105.10
060124	187.85 ± 0.59	87.02
060526	153.04 ± 0.52	89.72
060904B	46.42 ± 0.16	29.20
060929*	59.06 ± 0.11	44.87
061121	158.54 ± 0.50	155.43
070520B*	44.28 ± 0.12	38.54
070704*	75.49 ± 0.17	62.73
090621A*	135.58 ± 0.37	70.37
100619A*	55.24 ± 0.15	—
110709B	43.47 ± 0.13	28.60
110801A	104.93 ± 0.33	36.43
110820A*	77.57 ± 0.19	51.99
121123A*	103.35 ± 0.34	80.34
121217A	161.01 ± 0.49	89.44
140817A*	107.60 ± 0.35	82.06
141031A*	86.33 ± 0.27	54.62
141130A*	42.54 ± 0.14	34.37
160425A	41.62 ± 0.10	20.78

cannot produce Lorentz factors much greater than ~ 100 , this further highlights that it is struggling to reach the energies demanded of it by the data.

4.5 Conclusions

Due to their similarity to the prompt emission, giant X-ray flares in LGRBs are often considered to be evidence of continuing central engine activity. In this chapter, I have tested the feasibility of one of the most natural long-lived central engines: the magnetar model, in which the rotational energy of a highly-magnetised millisecond neutron star is released to the surrounding environment via its intense dipole field. The model for flaring is a magnetic propeller, which accelerates local material via magneto-centrifugal slinging and ejects it from the system. The magnetar is fed by fallback accretion, which maximises the available energy. I have provided fits to a sample of 19 LGRBs with giant flares in their X-ray light curves using MCMC simulations.

The results show that despite a good phenomenological match of the model to the data, in all but a few cases it is very energetically challenging to explain giant flares in LGRBs using a magnetar alone, especially given the further reduction of usable extracted energy predicted by Beniamini et al. (2017) and Metzger et al. (2018). This has strong implications for any models trying to explain LGRB prompt emission or late X-ray plateaux (Beniamini & Mochkovitch, 2017) with a magnetar, as the rotational energy budget appears to not be sufficient for flares without extra emission components or substantial fallback. However, the energy constraints may be lessened somewhat by the inclusion of the standard synchrotron afterglow and the reprocessing of the dipole emission in the forward shock.

5

Conclusions and Future Work

Throughout the science chapters of this thesis, I have modified the magnetar propeller model to include fallback accretion and have rigorously tested it against synthetic light curves and data from the *Swift* satellite of short gamma-ray bursts with extended emission and long gamma-ray bursts with giant X-ray flares. This final chapter summarises the main findings of the work I have undertaken thus far and presents preliminary methodologies and results for the next modelling test these samples could be subjected to.

5.1 Key Conclusions

The magnetar model is incredibly versatile since it is a naturally long-lived central engine that can provide continuous energy injection into a gamma-ray burst (GRB) fireball in order to explain phenomena such as: X-ray plateaux (Rowlinson et al., 2013; Gompertz et al., 2013), extended emission in short GRBs (SGRBs; Gompertz et al. 2014), and flares (Chincarini et al., 2010). This is achieved by the extraction of rotational energy from the magnetar and conversion into emission via a Blandford-Znajek mechanism (Blandford & Znajek, 1977) or magnetic propelling (Piro & Ott, 2011; Gompertz et al., 2014). The investigations I have outlined and discussed in the science chapters of this thesis have yielded insights into the role of fallback accretion within the magnetar model when applied to the subtypes of GRBs which pose the greatest challenge to the standard fireball picture of GRB prompt and afterglow emission - specifically short GRBs (SGRBs) with extended emission and long GRBs (LGRBs) with giant X-ray flares.

In Chapter 2, I modified a simple version of the magnetic propeller model to include fallback accretion. Fallback accretion augments the energy budget of the magnetar as it provides a mechanism to spin the magnetar back up, and hence easing the restrictions on the upper limit of the rotational energy of the magnetar. Extensive testing of this modified model showed that the four types previously defined in Gompertz et al. (2014) are recoverable with the modifications, although they have moved in parameter space, and a new set of light curve morphologies were revealed. This allows for a more diverse range of features in *Swift* light curves to be accounted for.

In Chapter 3, I began fitting the magnetar model with fallback accretion to *Swift* data of SGRBs with extended emission. Fallback accretion is an appropriate addition in this context since, after a collapsar or compact object binary merger (the most common evolutionary paths for magnetar formation), it is expected that a reservoir of mass would be available for fallback (up to $\approx 0.1 M_{\odot}$; Rosswog 2007; Lee et al. 2009). The parameters derived from the fits produced by the propeller model with fallback accretion to the SGRB with extended emission sample are consistent with theoretical predictions for magnetars. The model can cope with long dipole plateaux and

flare-like variability but struggles with the early-time, short-timescale variability. The addition of fallback accretion provided a noticeable improvement in matching light curves compared to those presented in Gompertz et al. (2014) and hence fallback accretion may play a pivotal role in explaining the features of extended emission light curves.

In Chapter 4, the magnetar propeller model with fallback accretion was then applied to LGRBs with giant X-ray flares. Due to their similarity to the prompt emission, giant X-ray flares in LGRBs are often considered to be evidence of continuing central engine activity. The magnetic propeller accelerates local material via magneto-centrifugal slinging and ejects it from the system which produces the emission for the flares. The fits show that despite a good phenomenological match of the model to the data, in all but a few cases it is very energetically challenging to explain giant flares in LGRBs using a magnetar alone. This has strong implications for any models trying to explain LGRB prompt emission or late X-ray plateaux (Beniamini & Mochkovitch, 2017) with a magnetar, as the rotational energy budget appears to not be sufficient for flares without extra emission components or substantial fallback.

Fig. 5.1 is a scatterplot matrix of the samples used to infer the best fitting parameters for the short GRB 061006 pertaining to Table 3.5 in Section 3.4 (arbitrarily chosen). It shows that the distributions for each parameter can be approximated by a normal distribution and have been well constrained, except in cases where the sampler has come against a hard parameter limit and the distribution has been distorted *e.g.*, P_i and η_{prop} . Fig. 5.2 is a similar scatterplot matrix for the long GRB 070704 pertaining to Table 4.2 in Section 4.4. As well as showing the normal distribution of the samples and that they are well constrained, it also shows some of the underlying correlations between the parameters, *i.e.*, $B \rightarrow P_i$, $B \rightarrow \log_{10}(R_D)$, $P_i \rightarrow \log_{10}(R_D)$ and $\log_{10}(\epsilon) \rightarrow \log_{10}(\delta)$, some of which are discussed in Section 2.5.1. Together these figures demonstrate that my methodology of running a full MCMC simulation, selecting the best individual probabilities, then using them as a starting point for a second MCMC simulation worked just as well for the real-world data as it did for the synthetic data, discussed in Section 2.5.

Overall, the application of the magnetar propeller model with fallback accretion to these challenging GRB subtypes provides mixed results. The ability to replenish the mass of the accretion

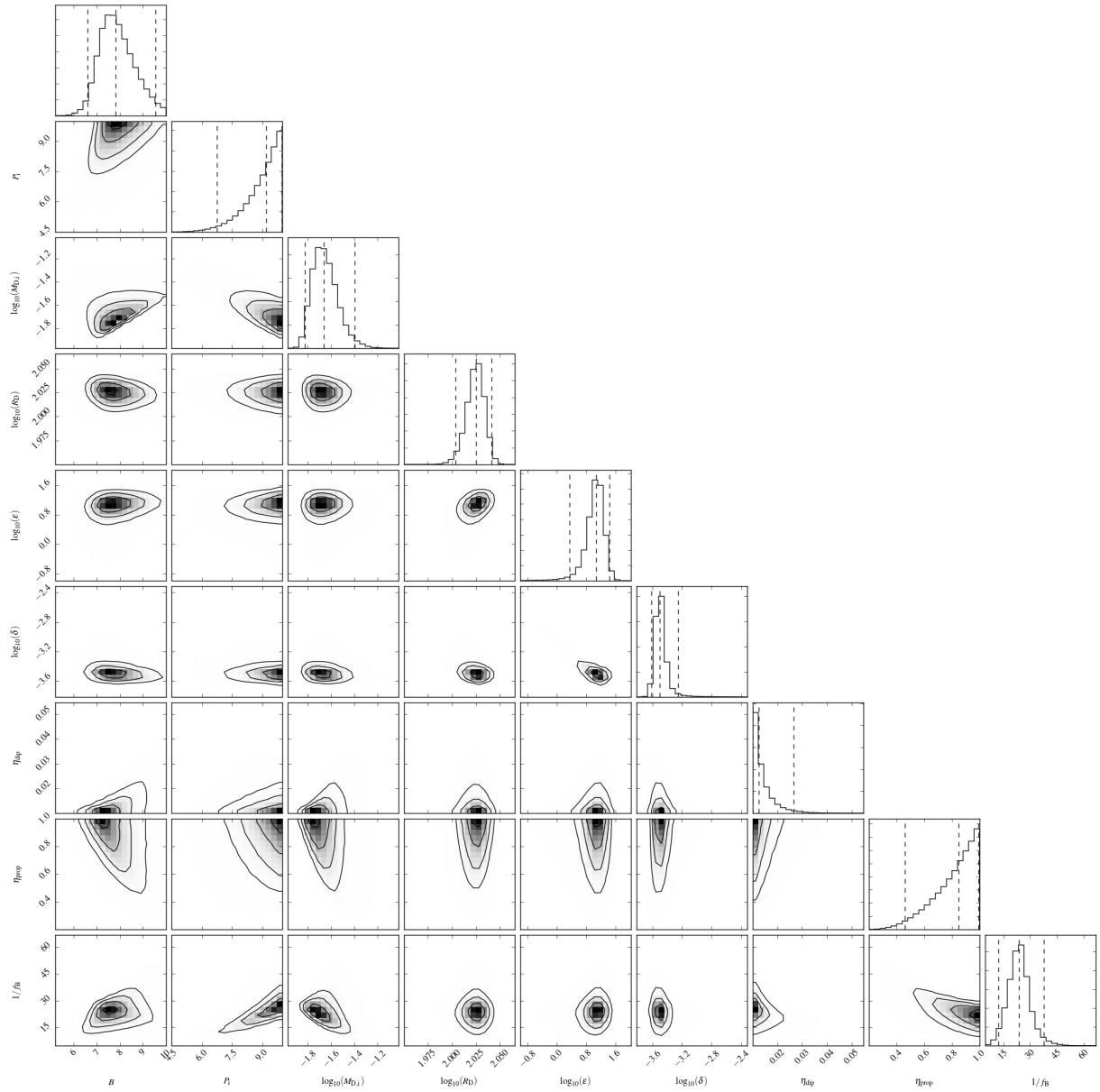


Figure 5.1: A scatterplot matrix of the sample distributions generated by the MCMC optimisation to SGRB 061006 using $n = 1$ and 9 free parameters pertaining to the results presented in Table 3.5 in Section 3.4.

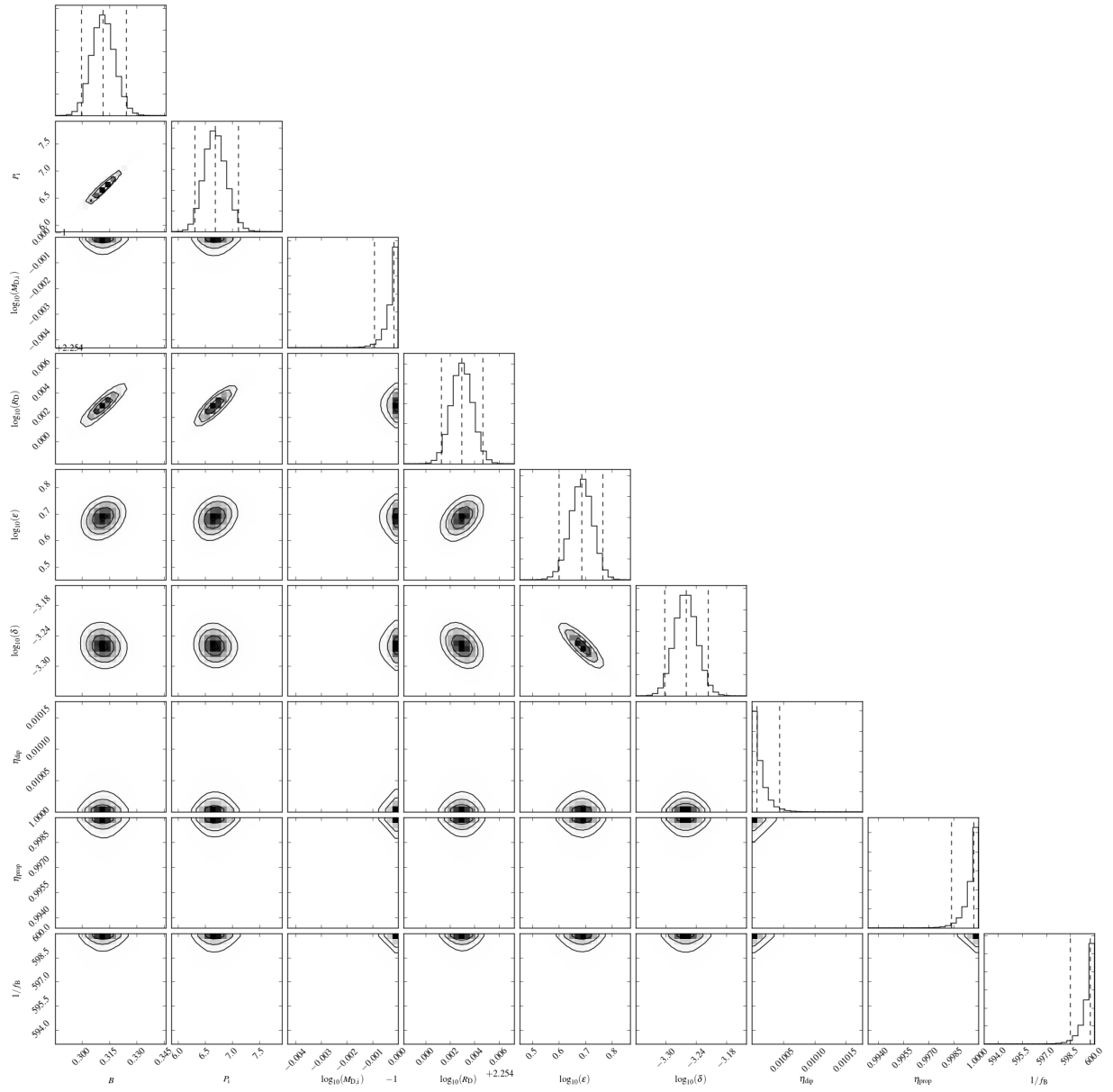


Figure 5.2: A scatterplot matrix of the sample distributions generated by the MCMC optimisation to LGRB 070704 pertaining to the results in Table 4.2 in Section 4.4.

disc and maximise the rotational energy of the magnetar is evidently an important contribution when considering the magnetar as a central engine for GRBs. It has been successful in improving the fits to SGRBs with extended emission but it is energetically challenged by LGRBs with giant X-ray flares. This suggests that, if a magnetar is the central engine in a long GRB, then there must be additional energy supplied by one or more processes external to the central engine. Such processes that have not been accounted for in this thesis include standard synchrotron afterglow and the reprocessing of the dipole emission in the forward shock.

5.2 Future Work

The main weakness of the magnetar propeller model with fallback accretion is the difficulty it faces in reproducing the short timescale variability that is observed throughout the *Swift* light curves. This is particularly noticeable in the flares in *e.g.*, LGRBs 060124, 110709B and 110801A which exhibit precursor flares or a “jaggedness” to the peak of their flares that could imply multiple flares in a short time period. Also, SGRBs such as 060614, 080503 and 100522A show a lot of variability in their early-time light curves that could suggest bursts of energy being released rapidly in a short timescale rather than a smooth energy release.

Wang & Dai (2013) have performed a statistical analysis indicating that a magnetic reconnection-driven, self-organised criticality regime causing continual solar flares may also be the origin of flares in GRB afterglows. In this scenario, small-scale flares are regularly occurring and sum together to create a background continuum. The amplitude population of these flares form a power-law distribution with a negative index which leads to the less regular occurrence of a large flare.

In the following sections, I explore a pulse model to represent the flares, outline a methodology for drawing the pulses from statistical distributions and matching the model to a synthetic light curve. I then discuss preliminary results from a test run of this methodology and where the pulse model needs to be improved upon.

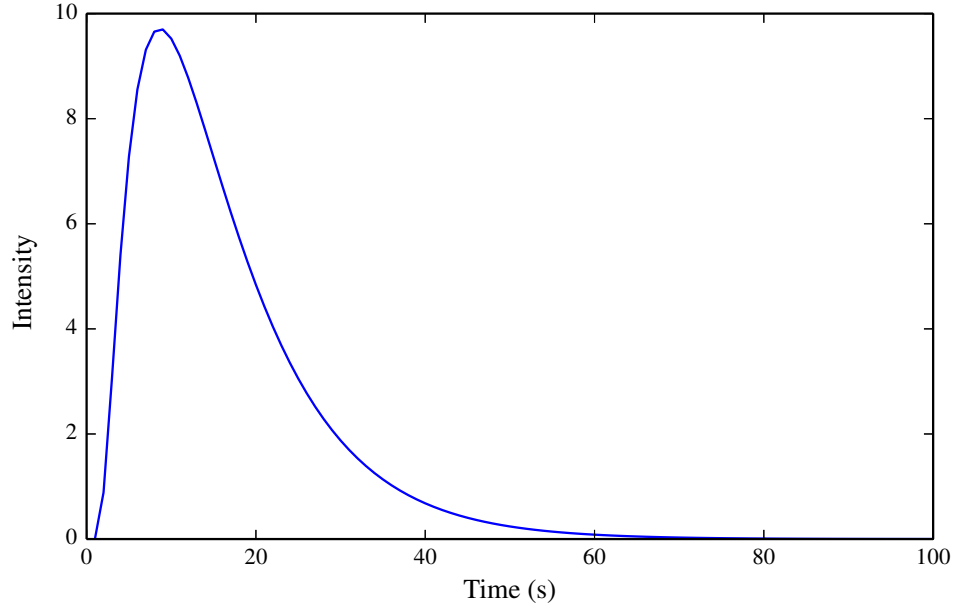


Figure 5.3: Equation (5.1) plotted for $\tau_1 = 8.10$ s and corresponding $\tau_2 = 9.24$ s. An amplitude $A = 9.71$ (dimensionless in this example) was randomly selected from a power-law distribution of index $N = -1.11$. The corresponding peak time is $\tau_{\text{peak}} = 8.65$ s and the rise and decay times are $\tau_{\text{rise}} = 5.44$ s and $\tau_{\text{decay}} = 14.69$ s.

5.2.1 Pulse Model

To create the pulses, I used the model described in Norris et al. (2005) and Peng et al. (2010)

$$I(t) = A\lambda \exp\left[-\frac{\tau_1}{t} - \frac{t}{\tau_2}\right] \quad \text{for } t > 0 \quad (5.1)$$

where A is the amplitude of the pulse which is chosen randomly from a power-law index of $-3.0 < N < -0.5$; τ_1 and τ_2 are the two fundamental timescales of the fast rise, exponential decay pulse - τ_1 is randomly selected from a power-law distribution of index $0 < M < 3$ and, for simplicity, I have used the relation $\tau_2 \approx 16.6\tau_1^{-0.28}$ (Norris et al., 2005) in order to reduce the number of free parameters; finally, $\lambda = \exp(2\mu)$ where $\mu = (\tau_1/\tau_2)^{\frac{1}{2}}$. An example pulse using Equation (5.1) is depicted in Fig. 5.3.

It is important to note that the effects of τ_1 and τ_2 on the amplitude are not obvious since their influence arises from the combination of exponentials, and both terms operate across the pulse's

duration. As a result, τ_1 and τ_2 are not respectively the rise and decay timescales - I calculate these below. In a minimal physical sense, this model represents an exponential process supplying energy on a timescale τ_1 and a similar but separate process affects a condition necessary for the continuance of the supply on a timescale τ_2 . The former could be a cascading injection of radiating particles and the latter an explosive expansion of the source, as an example (Norris et al., 2005).

After a timescale of $\tau_{\text{peak}} = (\tau_1\tau_2)^{\frac{1}{2}}$, the intensity of the pulse is at its maximum, normalised by λ to a peak intensity of A . The width of the pulse is measured between the two points where the intensity is equal to $1/e$.

$$\omega = \Delta\tau_{1/e} = \tau_2(1 + 4\mu)^{\frac{1}{2}} \quad (5.2)$$

The term $(1 + 4\mu)^{\frac{1}{2}}$ describes the inverse of the asymmetry of the pulse, κ^{-1} , which can also be expressed as $\kappa = \tau_2/\omega$ using Equation (5.2). This allows for a symmetric pulse in the limit $\mu = (\tau_1/\tau_2)^{\frac{1}{2}} \rightarrow \infty$. From the definition of κ and Equation (5.2), the decay and rise timescales of the pulse can be calculated as follows.

$$\tau_{\text{decay,rise}} = \frac{1}{2}\omega(1 \pm \kappa) \quad (5.3)$$

5.2.2 Methodology

For testing purposes, a type I synthetic burst from Chapter 2 was used. The whole synthetic light curve was integrated, using the trapezium rule, in order to place limits on the maximum and minimum pulse amplitudes that could be drawn from the probability. These limits were chosen to be $10^{-12}E_{\text{tot}} < A < 10^{-8}E_{\text{tot}}$ (where E_{tot} is the total energy of the synthetic light curve) as testing showed this range excluded large oscillations in the light curve, which would be unphysical, though still allowing for a variability on the scale represented in *Swift* light curves. The main fitting parameters are M , the index of the power-law distribution τ_1 values are drawn from, and N , the index of the power-law distribution the amplitudes are drawn from. Though ideally, these would be linked so that small amplitudes have short timescales and large amplitudes have long timescales, leaving N as the only fitting parameter. However, this would require a physical theory to under-pin such a link - such as magnetic reconnection, a fragmented accretion

disc causing “clumpy” fallback, or another unknown mechanism - which is beyond the scope of this thesis.

The synthetic light curve was separated into bins of ~ 100 s and pulses were added to each bin until the integration of the pulsed light curve was approximately equal to the integration of the synthetic light curve, to within a $\pm 5\%$ tolerance, before moving onto the next bin. An offset was randomly selected from a uniform distribution across the bin so that the pulses were spread evenly throughout. Any pulses that “spilled over” into the next bin were allowed to straddle the boundary and the additional energy was accounted for in the integration before adding more pulses to that bin. Any pulses that caused the integration of the pulsed light curve to exceed the upper 5% tolerance of the synthetic light curve were discarded, however, this should be updated so that a subroutine carries such a burst over to the next available bin.

5.2.3 Preliminary Results

The result of a preliminary test of the methodology is presented in Fig. 5.4. While the model performs well when reconstructing the tail of the emission, the early-time emission and the rise of the hump feature are poorly matched. This is largely due to the discrepancy in scaling. While the synthetic burst and the pulsed model have been generated in linear time intervals, the features of the synthetic curve can only be seen on a log-log scaled plot. Hence, the pulsed model does not have the resolution at early times to adequately match the data which results in a very large χ^2_ν value. Though this could also be in part due to the lack of errors on the synthetic light curve. It would be interesting to conduct another test using the data from Section 2.5 to ascertain whether the errors would reduce the χ^2_ν value.

Due to the random selection process for the input parameters and the processing time to individually generate pulses and regularly integrate the pulsed light curve, a standard MCMC routine cannot be used to match the model as the random number generator seed would have to become a fitting parameter in its own right. Instead, I propose to divide the ranges of N and M into suitable increments and, for each N - M pairing, run the program a given number of times and calculate a

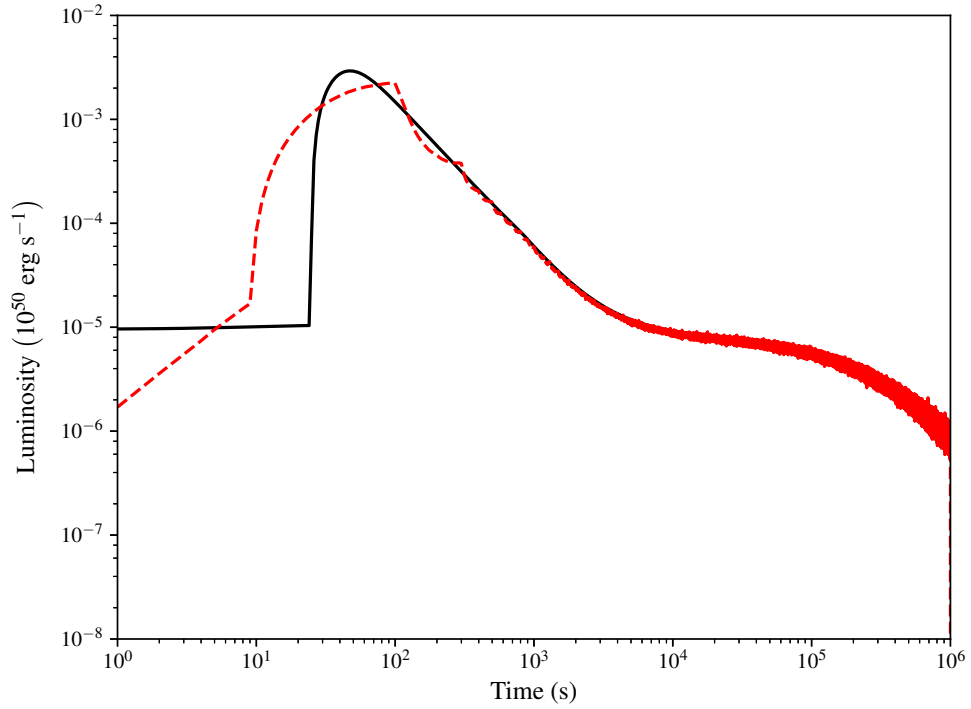


Figure 5.4: Preliminary results of matching a pulsed light curve to a synthetic data set using integration. Black, solid line - synthetic type I burst; red, dashed line - pulsed light curve model. The goodness-of-fit statistic is $\chi^2_\nu = 4.62 \times 10^{89}$.

χ^2_ν value. A histogram of the of the collected χ^2_ν values would provide the most probable values of N and M .

Presently, this model needs an improved method to provide better resolution at early times, especially since this is when a lot of variability takes place in SGRBs particularly. This would help improve the χ^2_ν values of the matching results.



Derivation of the Alfvén Radius from the Magnetic and Ram Pressures

By equating Equations 2.1 (magnetic pressure) and 2.2 (ram pressure) and rearranging for r , it can be shown that the coefficient of the Alfvén radius equation is approximately unity.

$$\frac{\mu^2}{8\pi r^6} = \frac{\dot{M}}{4\pi} \left(\frac{2GM_*}{r^5} \right)^{\frac{1}{2}} \quad (\text{A.1})$$

$$\frac{\mu^2}{2} = 2^{\frac{1}{2}} (GM_*)^{\frac{1}{2}} \dot{M} \left(\frac{1}{r^5} \right)^{\frac{1}{2}} r^6 \quad (\text{A.2})$$

$$\mu^2 = 2^{\frac{3}{2}} (GM_*)^{\frac{1}{2}} \dot{M} r^{-\frac{5}{2}} r^{\frac{12}{2}} \quad (\text{A.3})$$

$$\mu^2 = 2^{\frac{3}{2}} (GM_*)^{\frac{1}{2}} \dot{M} r^{\frac{7}{2}} \quad (\text{A.4})$$

$$r^{\frac{7}{2}} = 2^{-\frac{3}{2}} \mu^2 (GM_*)^{-\frac{1}{2}} \dot{M}^{-1} \quad (\text{A.5})$$

$$r = 2^{-\frac{3}{7}} \mu^{\frac{4}{7}} (GM_*)^{-\frac{1}{7}} \dot{M}^{-\frac{2}{7}} \quad (\text{A.6})$$

$$2^{-\frac{3}{7}} \approx 1 \therefore r_m \simeq \mu^{\frac{4}{7}} (GM_*)^{-\frac{1}{7}} \dot{M}^{-\frac{2}{7}} \quad (\text{A.7})$$

B

Exploded Plots of Burst Types

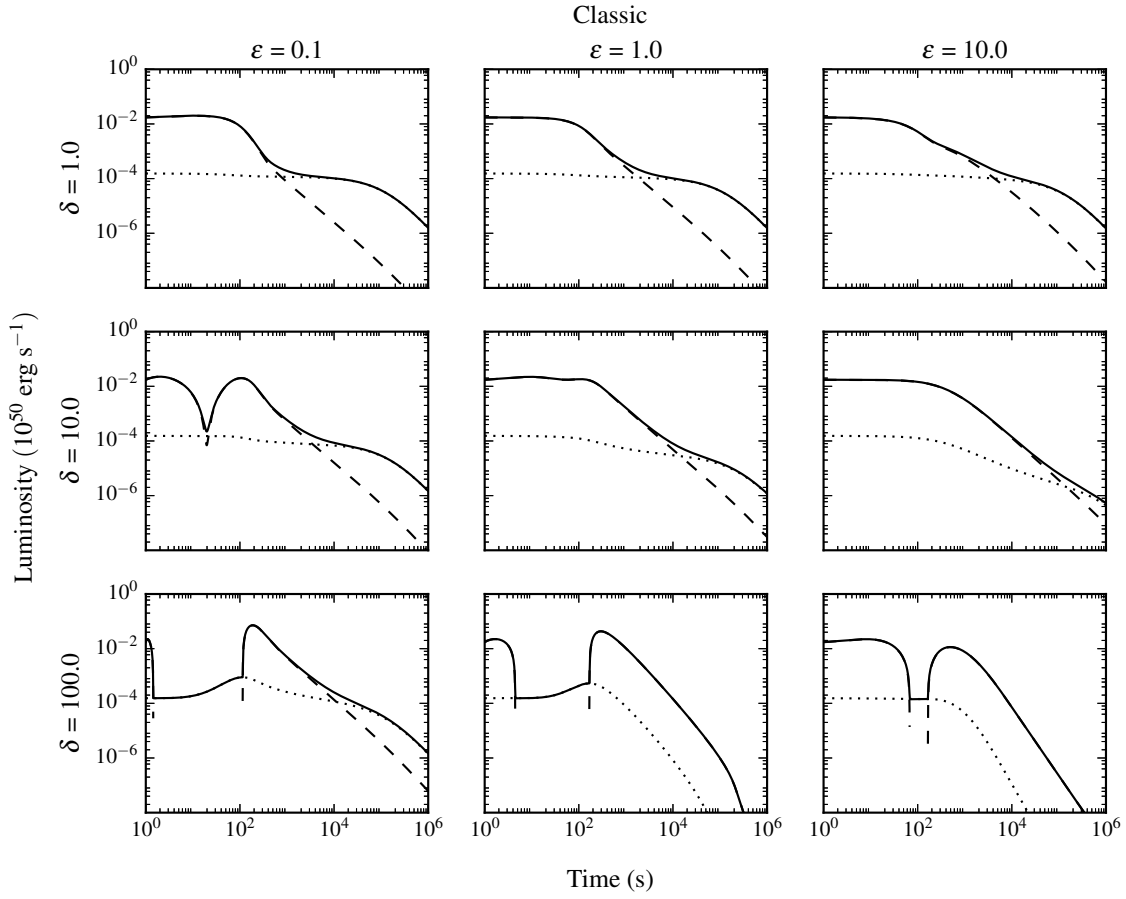


Figure B.1: “Exploded” view of a ‘classic’ type burst (of arbitrary parameters) depicting how the fallback parameters effect the morphology of the burst. The fraction of the fallback timescale, ϵ , increases from left to right and the fraction of the fallback mass, δ , increases from top to bottom.

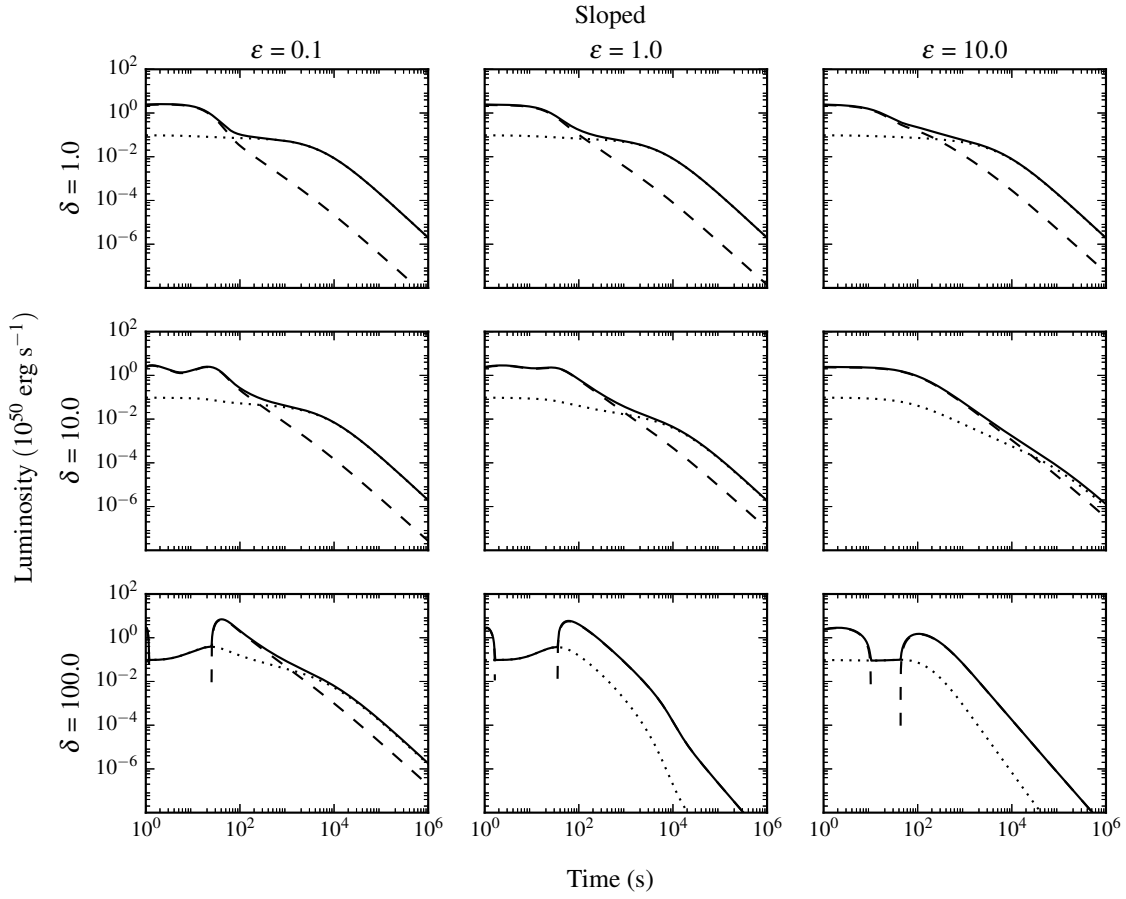


Figure B.2: “Exploded” view of a ‘sloped’ type burst (of arbitrary parameters) depicting how the fallback parameters effect the morphology of the burst. The fraction of the fallback timescale, ϵ , increases from left to right and the fraction of the fallback mass, δ , increases from top to bottom.

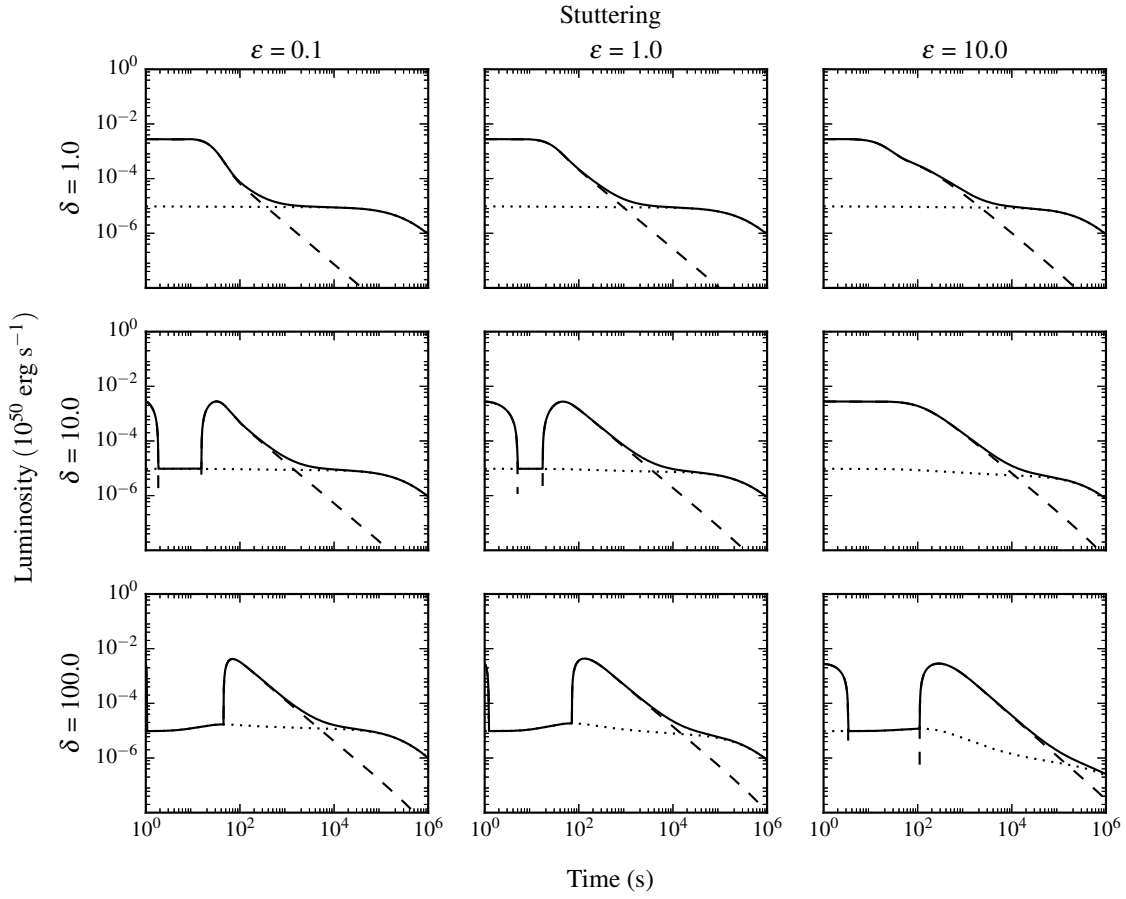


Figure B.3: “Exploded” view of a ‘stuttering’ type burst (of arbitrary parameters) depicting how the fallback parameters effect the morphology of the burst. The fraction of the fallback timescale, ϵ , increases from left to right and the fraction of the fallback mass, δ , increases from top to bottom.

C

Correlations between Fitting Parameters

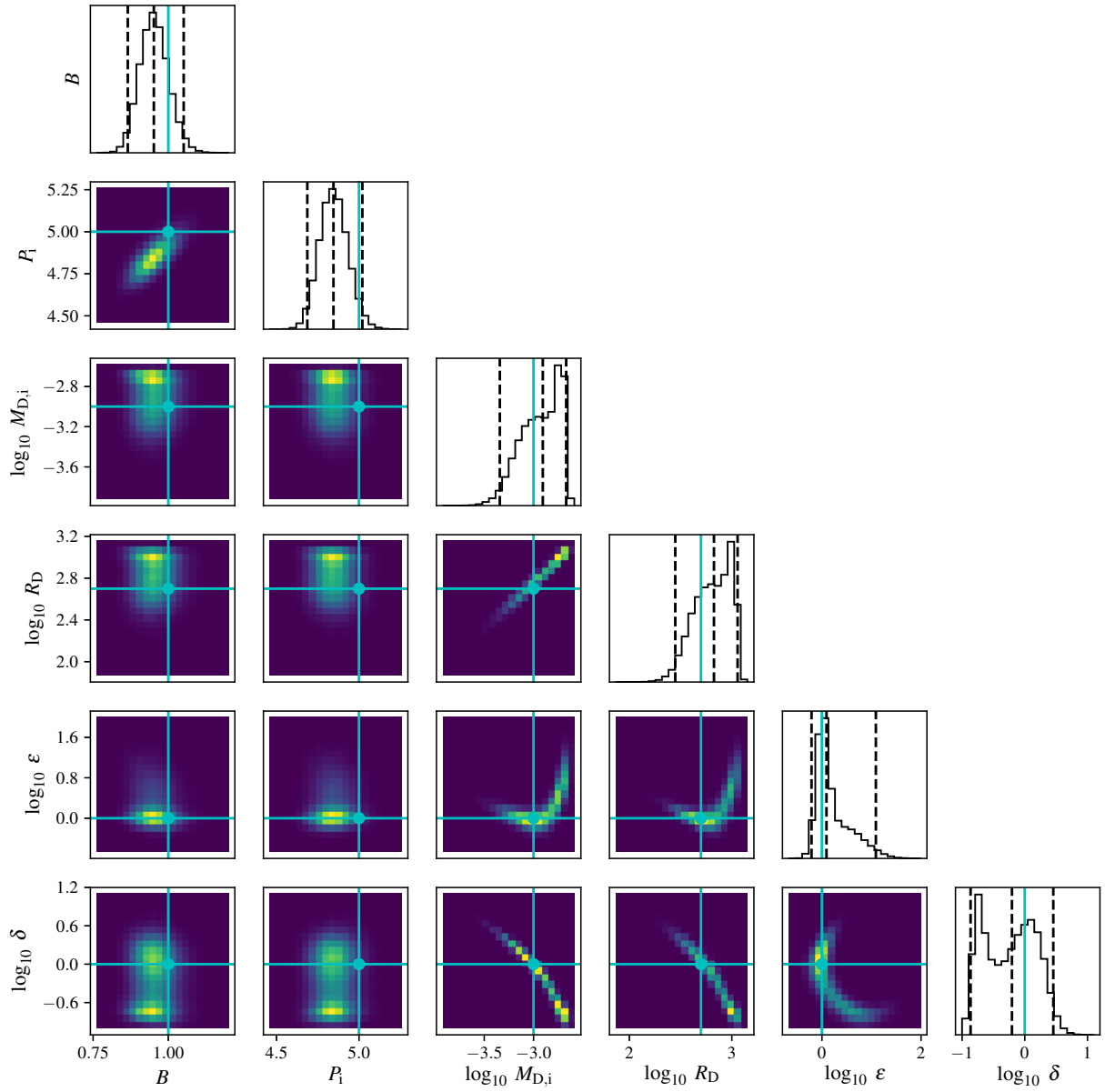


Figure C.1: A scatterplot matrix showing correlations between fitting parameters for a fit to a type II classic burst.

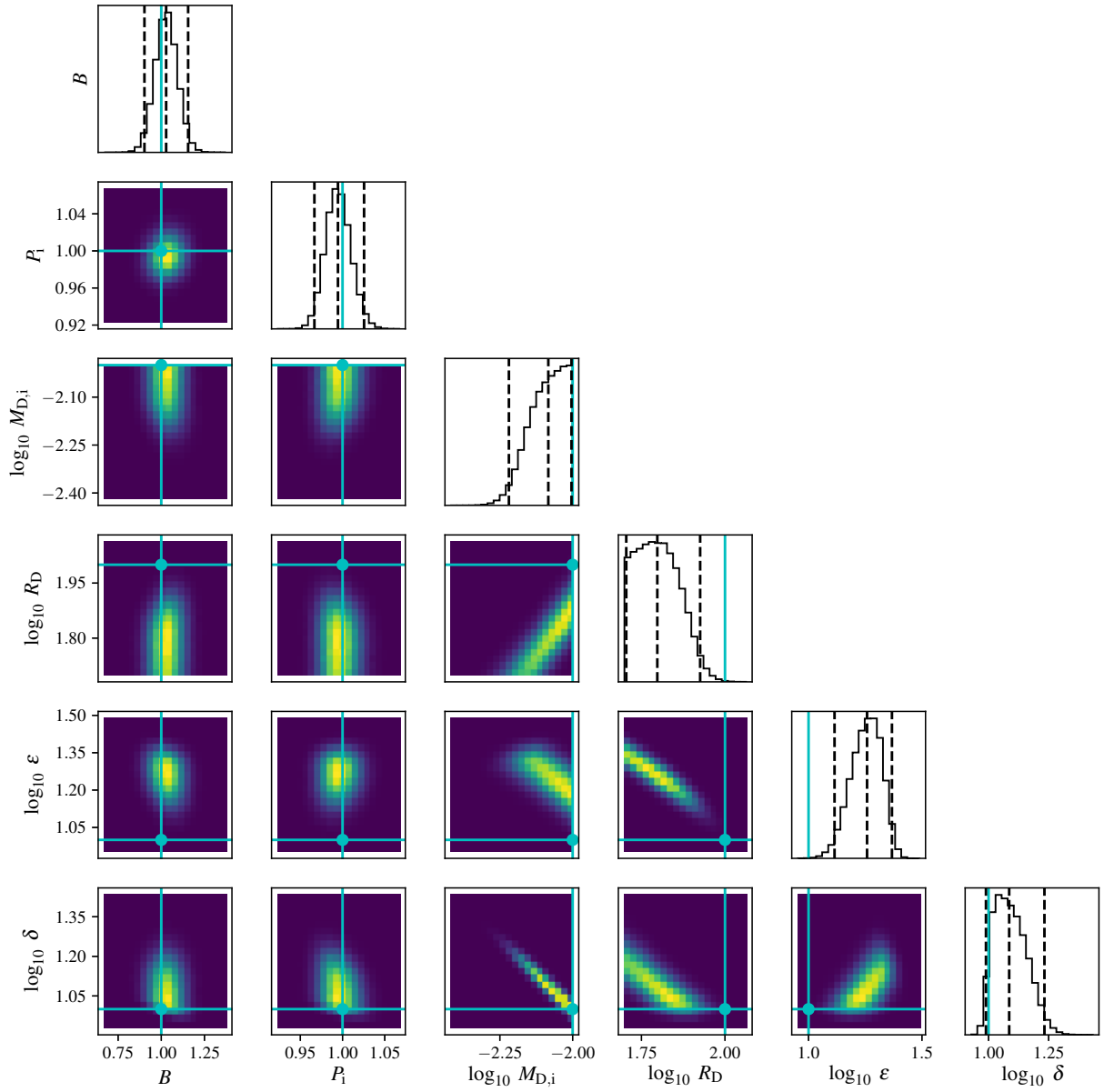


Figure C.2: A scatterplot matrix showing correlations between fitting parameters for a fit to a type III sloped burst.

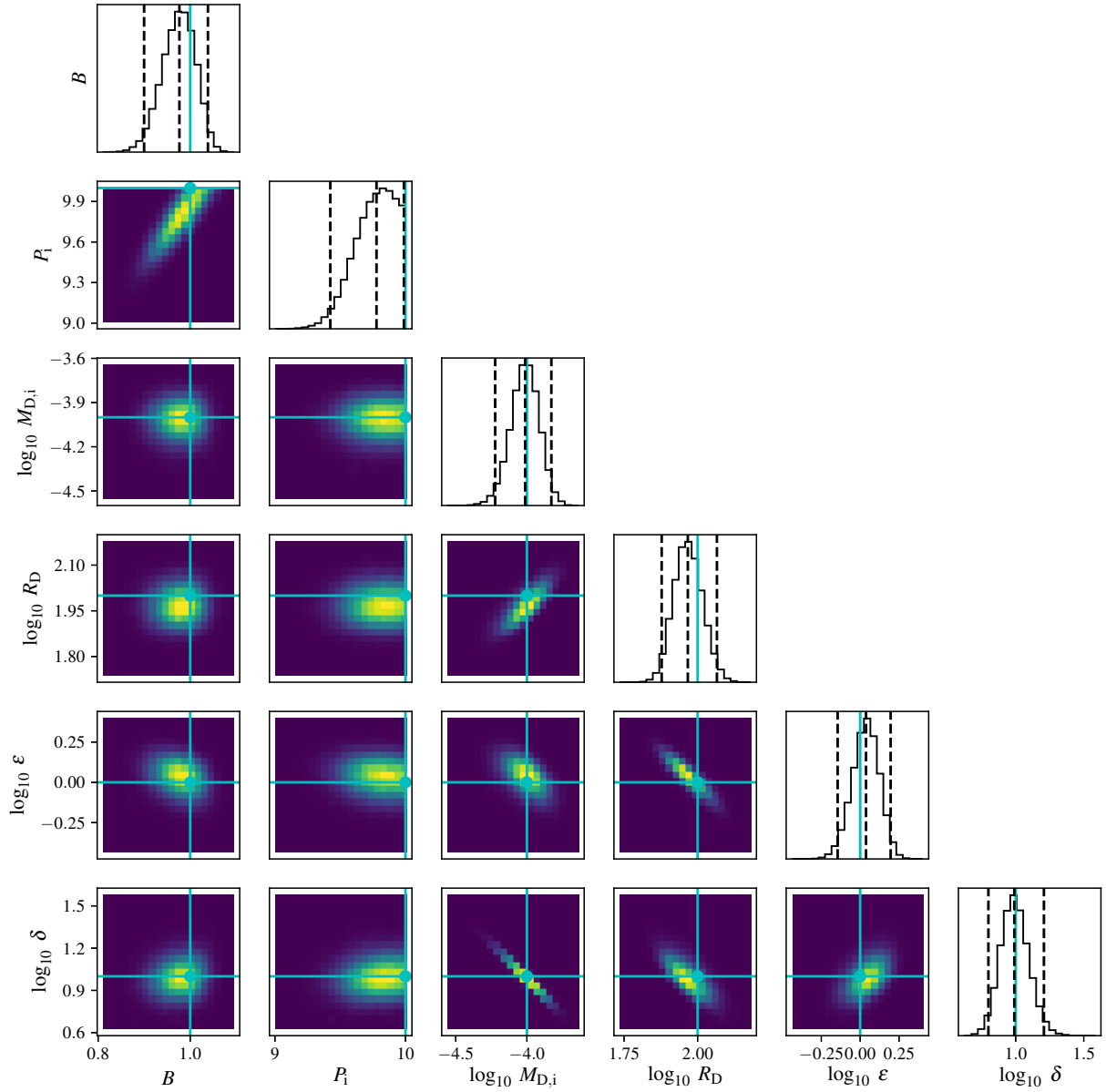


Figure C.3: A scatterplot matrix showing correlations between fitting parameters for a fit to a type IV stuttering burst.

Bibliography

- Abbott B. P., et al., 2017a, Phys. Rev. Lett., 119
- Abbott B. P., et al., 2017b, ApJL, 848
- Abbott B. P., et al., 2017c, ApJL, 848, L12
- Afonso P., et al., 2011, A&A, 526, A154
- Akiyama S., Wheeler J. C., Meier D. L., Lichtenstadt I., 2003, ApJ, 584, 954
- Aptekar R. L., et al., 1995, Space Science Rev., 71, 265
- Atwood W. B., et al., 2009, ApJ, 697, 1071
- Band D., et al., 1993, in American Astronomical Society Meeting Abstracts #182. p. 924
- Barkov M. V., Pozanenko A. S., 2011, MNRAS, 417, 2161
- Barthelmy S. D., et al., 1994, in Fishman G. J., ed., American Institute of Physics Conference Series Vol. 307, Gamma-Ray Bursts. p. 643
- Barthelmy S. D., et al., 2005, Space Science Rev., 120, 143
- Belczynski K., Perna R., Bulik T., Kalogera V., Ivanova N., Lamb D. Q., 2006, ApJ, 648, 1110
- Beniamini P., Kumar P., 2016, Monthly Notices of the Royal Astronomical Society: Letters, 457, L108

Beniamini P., Mochkovitch R., 2017, *Astronomy & Astrophysics*, 605, A60

Beniamini P., Giannios D., Metzger B. D., 2017, *MNRAS*, 472, 3058

Berger E., 2007, *ApJ*, 670, 1254

Berger E., 2010, *ApJ*, 722, 1946

Berger E., Gladders M., 2006, *GRB Coordinates Network*, 0, 5170

Bernardini M. G., 2015, *Journal of High Energy Astrophysics*, 7, 64

Blandford R. D., Znajek R. L., 1977, *MNRAS*, 179, 433

Bloom J. S., Djorgovski S. G., Kulkarni S. R., Frail D. A., 1998, *ApJL*, 507, L25

Bloom J. S., Sigurdsson S., Pols O. R., 1999a, *MNRAS*, 305, 763

Bloom J. S., et al., 1999b, *Nature*, 401, 453

Bloom J. S., Frail D. A., Sari R., 2001, *ApJ*, 121, 2879

Bloom J. S., Kulkarni S. R., Djorgovski S. G., 2002, *ApJ*, 123, 1111

Bloom J. S., et al., 2006, *ApJ*, 638, 354

Boella G., Butler R. C., Perola G. C., Piro L., Scarsi L., Bleeker J. A. M., 1997, *A&AS*, 122, 299

Bromberg O., Nakar E., Piran T., et al., 2013, *ApJ*, 764, 179

Bucciantini N., Thompson T. A., Arons J., Quataert E., Del Zanna L., 2006, *MNRAS*, 368, 1717

Bucciantini N., Metzger B. D., Thompson T. A., Quataert E., 2012, *MNRAS*, 419, 1537

Burrows D. N., et al., 2005a, *Space Science Rev.*, 120, 165

Burrows D. N., et al., 2005b, *Science*, 309, 1833

Cabrera Lavers A., de Ugarte Postigo A., Castro-Tirado A. J., Gorosabel J., Thoene C. C., 2011, *GRB Coordinates Network*, 0, 12234

Cannizzo J., Troja E., Gehrels N., 2011, *ApJ*, 734, 35

Cavallo G., Rees M. J., 1978, *MNRAS*, 183, 359

Cavanaugh J. E., Neath A. A., 2011, in , *International Encyclopedia of Statistical Science*. Springer, pp 26–29

Cenko S., Kasliwal M., Cameron P., Kulkarni S., Fox D., 2006, *GRB Coordinates Network*, 5946, 1

Chapman R., Levan A. J., Priddey R. S., Tanvir N. R., Wynn G. A., King A. R., Davies M. B., 2007, in Napiwotzki R., Burleigh M. R., eds, *Astronomical Society of the Pacific Conference Series Vol. 372, 15th European Workshop on White Dwarfs*. p. 415

Chincarini G., et al., 2010, *MNRAS*, 406, 2113

Cucchiara A., et al., 2011, *ApJ*, 736

Curran P. A., Starling R. L. C., O’Brien P. T., Godet O., van der Horst A. J., Wijers R. A. M. J., 2008, *A&A*, 487, 533

D’Avanzo P., Fiore F., Piranomonte S., Covino S., Tagliaferri G., Chincarini G., Stella L., 2007, *GRB Coordinates Network*, 7152

D’Avanzo P., et al., 2009, *A&A*, 498, 711

Dai Z., Lu T., 1998, arXiv preprint astro-ph/9810402

Dai Z., Lu T., 2002, *ApJL*, 565, L87

Dall’Osso S., Stratta G., Guetta D., Covino S., De Cesare G., Stella L., 2011, *A&A*, 526, A121

Dall’Osso S., Perna R., Tanaka T. L., Margutti R., 2017, *MNRAS*, 464, 4399

Dermer C. D., 2004, *ApJ*, 614, 284

Dessart L., Burrows A., Livne E., Ott C. D., 2007, *ApJ*, 669, 585

Dessart L., Burrows A., Livne E., Ott C. D., 2008, *ApJL*, 673, L43

Djorgovski S. G., Kulkarni S. R., Bloom J. S., Goodrich R., Frail D. A., Piro L., Palazzi E., 1998, ApJL, 508, L17

Drenkhahn G., Spruit H. C., 2002, A&A, 391, 1141

Duncan R. C., Thompson C., 1992, ApJL, 392, L9

Ekşi K. Y., Hernquist L., Narayan R., 2005, ApJL, 623, L41

Elliott J., et al., 2014, A&A, 562, A100

Evans P. A., et al., 2007, A&A, 469, 379

Evans P. A., et al., 2009, MNRAS, 397, 1177

Evans P., et al., 2017, Science, p. 9580

Falcone A. D., et al., 2006, ApJ, 641, 1010

Fan Y.-Z., Xu D., 2006, MNRAS, 372, L19

Fishman G. J., Meegan C. A., Parnell T. A., Wilson R. B., Paciesas W., Matteson J. L., Cline T., Teegarden B., 1985, ICRC, 3, 343

Foreman-Mackey D., Hogg D. W., Lang D., Goodman J., 2013, Publications of the Astronomical Society of the Pacific, 125, 306

Fox D. B., et al., 2005, Nature, 437, 845

Frail D. A., et al., 2001, ApJL, 562, L55

Fruchter A. S., et al., 1999, ApJL, 519, L13

Fruchter A. S., et al., 2006, Nature, 441, 463

Fryer C. L., Woosley S. E., Herant M., Davies M. B., 1999, ApJ, 520, 650

Fugazza D., et al., 2006, GRB Coordinates Network, 0, 5513

Galama T. J., et al., 1998, Nature, 395, 670

Galama T. J., et al., 2000, ApJ, 536, 185

Gehrels N., Razzaque S., 2013, Frontiers of Physics, 8, 661

Gehrels N., et al., 2004, ApJ, 611, 1005

Gehrels N., et al., 2005, Nature, 437, 851

Gehrels N., Ramirez-Ruiz E., Fox D. B., 2009, ARA&A, 47, 567

Giacomazzo B., Perna R., 2013, ApJL, 771, L26

Gibson S. L., Wynn G. A., Gompertz B. P., O'Brien P. T., 2017, MNRAS, 470, 4925

Gibson S. L., Wynn G. A., Gompertz B. P., O'Brien P. T., 2018, MNRAS, 478, 4323

Goad M. R., et al., 2007, A&A, 476, 1401

Goldstein A., et al., 2017, ApJL, 848, L14

Gomboc A., 2012, Contemporary Physics, 53, 339

Gompertz B. P., O'Brien P. T., Wynn G. A., Rowlinson A., 2013, MNRAS, p. 293

Gompertz B. P., O'Brien P. T., Wynn G. A., 2014, MNRAS, 438, 240

Gompertz B. P., van der Horst A. J., O'Brien P. T., Wynn G. A., Wiersema K., 2015, MNRAS, 448, 629

Gompertz B., et al., 2017, arXiv preprint arXiv:1710.05442

Goodman J., 1986, ApJL, 308, L47

Goodman J., Weare J., 2010, Communications in applied mathematics and computational science, 5, 65

Graham J., et al., 2009, ApJ, 698, 1620

Grindlay J., Portegies Zwart S., McMillan S., 2006, Nat. Phys., 2, 116

Harrison F. A., et al., 1999, ApJL, 523, L121

Hindmarsh A. C., 1983, in Stepleman R. S., ed., IMACS Transactions on Scientific Computation
Vol. 1, IMACS Transactions on Scientific Computation. North-Holland, Amsterdam, pp 55–64

Hjorth J., et al., 2003, *Nature*, 423, 847

Hurley K., et al., 2005, *Nature*, 434, 1098

Kaneko Y., Bostancı Z. F., Göğüş E., Lin L., 2015, *MNRAS*, 452, 824

Katz J. I., 1997, *ApJ*, 490, 633

Klebasedel R. W., Strong I. B., Olson R. A., 1973, *ApJ*, 182, L85

Kouveliotou C., Meegan C. A., Fishman G. J., Bhat N. P., Briggs M. S., Koshut T. M., Paciesas
W. S., Pendleton G. N., 1993, *ApJ*, 413, L101

Kumar P., Panaitescu A., 2000, *ApJL*, 541, L51

Kumar P., Piran T., 2000, *ApJ*, 535, 152

Kumar P., Narayan R., Johnson J. L., 2008, *MNRAS*, 388, 1729

Lattimer J. M., Prakash M., 2001, *ApJ*, 550, 426

Lattimer J., Prakash M., 2004, *Science*, 304, 536

Lee W. H., Ramirez-Ruiz E., López-Cámara D., 2009, *ApJL*, 699, L93

Lei W.-H., Zhang B., Liang E.-W., 2013, *ApJ*, 765, 125

Lü J., Zou Y.-C., Lei W.-H., Zhang B., Wu Q., Wang D.-X., Liang E.-W., Lü H.-J., 2012, *ApJ*,
751, 49

Lyons N., O’Brien P., Zhang B., Willingale R., Troja E., Starling R., 2010, *MNRAS*, 402, 705

MacFadyen A. I., Woosley S. E., 1999, *ApJ*, 524, 262

MacKay D. J. C., 2003, *Information Theory, Inference, and Learning Algorithms*. Cambridge
University Press

Mangano V., et al., 2007, *A&A*, 470, 105

Margutti R., et al., 2011, *MNRAS*, 417, 2144

Mazets E. P., Golenetskii S. V., 1981, *Ap&SS*, 75, 47

Meegan C. A., Fishman G. J., Wilson R. B., Paciesas W. S., Pendleton G. N., Horack J. M., Brock M. N., Kouveliotou C., 1992, *Nature*, 355, 143

Meegan C., et al., 2009, *ApJ*, 702, 791

Mereghetti S., Pons J. A., Melatos A., 2015, *Space Science Rev.*, 191, 315

Mészáros P., 2002, *ARA&A*, 40, 137

Mészáros P., 2006, *Reports on Progress in Physics*, 69, 2259

Mészáros P., Rees M. J., 1993, *ApJL*, 418, L59

Mészáros P., Rees M. J., 1997, *ApJ*, 476, 232

Mészáros P., Rees M. J., 1999, *MNRAS*, 306, L39

Mészáros P., Rees M. J., 2014, arXiv e-print, arXiv:1401.3012

Mészáros P., Rees M., Wijers R., 1998, *ApJ*, 499, 301

Metzger M. R., Djorgovski S. G., Kulkarni S. R., Steidel C. C., Adelberger K. L., Frail D. A., Costa E., Frontera F., 1997, *Nature*, 387, 878

Metzger B. D., Quataert E., Thompson T. A., 2008, *MNRAS*, 385, 1455

Metzger B. D., Arcones A., Quataert E., Martínez-Pinedo G., 2010, *MNRAS*, 402, 2771

Metzger B. D., Giannios D., Thompson T. A., Bucciantini N., Quataert E., 2011, *MNRAS*, 413, 2031

Metzger B. D., Beniamini P., Giannios D., 2018, *ApJ*, 857, 95

Miller M. C., Miller J. M., 2015, *Phys. Rep.*, 548, 1

Mirabal N., Halpern J. P., 2006, GRB Coordinates Network, 0, 4591

Mu H.-J., et al., 2016, ApJ, 831, 111

Narayan R., Piran T., Shemi A., 1991, ApJL, 379, L17

Narayan R., Paczynski B., Piran T., 1992, ApJL, 395, L83

Norris J. P., Bonnell J. T., 2006, ApJ, 643, 266

Norris J. P., Hertz P., Wood K. S., Kouveliotou C., 1991, ApJ, 366, 240

Norris J. P., Nemiroff R. J., Bonnell J. T., Scargle J. D., Kouveliotou C., Paciesas W. S., Meegan C. A., Fishman G. J., 1996, ApJ, 459, 393

Norris J. P., Bonnell J. T., Kazanas D., Scargle J. D., Hakkila J., Giblin T. W., 2005, ApJ, 627, 324

Norris J. P., Barthelmy S. D., Cummings J. R., Gehrels N., 2015, GRB Coordinates Network, 17759

Nousek J. A., et al., 2006, ApJ, 642, 389

O'Brien P. T., et al., 2006, ApJ, 647, 1213

Paczynski B., 1986, ApJL, 308, L43

Paczynski B., 1990, ApJ, 363, 218

Paczynski B., 1991, Acta Astronomica, 41, 257

Palmer D. M., et al., 2005, Nature, 434

Panaitescu A., Kumar P., 2001, ApJL, 560, L49

Panaitescu A., Mészáros P., Gehrels N., Burrows D., Nousek J., 2006, MNRAS, 366, 1357

Parfrey K., Spitkovsky A., Beloborodov A. M., 2016, ApJ, 822, 33

Penacchioni A. V., Ruffini R., Bianco C. L., Izzo L., Muccino M., Pisani G. B., Rueda J. A., 2013, A&A, 551, A133

Peng Z. Y., Yin Y., Bi X. W., Zhao X. H., Fang L. M., Bao Y. Y., Ma L., 2010, *ApJ*, 718, 894

Peng F.-K., Liang E.-W., Wang X.-Y., Hou S.-J., Xi S.-Q., Lu R.-J., Zhang J., Zhang B., 2014, *ApJ*, 795, 155

Perley D. A., et al., 2009, *ApJ*, 696, 1871

Phinney E. S., 1991, *ApJL*, 380, L17

Piran T., 1999, *Phys. Rep.*, 314, 575

Piro A. L., Ott C. D., 2011, *ApJ*, 736, 108

Popham R., Woosley S. E., Fryer C., 1999, *ApJ*, 518, 356

Poza H. B., 1981, *Journal of Spacecraft and Rockets*, 18, 178

Price D. J., Rosswog S., 2006, *Science*, 312, 719

Price P. A., Berger E., Fox D. B., 2006, *GRB Coordinates Network*, 5275

Prochaska J., Bloom J., Chen H.-W., Hansen B., Kalirai J., Rich M., Richer H., 2005, *GRB Coordinates Network*, 3700, 1

Qin Y., et al., 2012, *ApJ*, 763, 15

Racusin J. L., et al., 2009, *ApJ*, 698, 43

Ramirez-Ruiz E., Fenimore E. E., 2000, *ApJ*, 539, 712

Rea N., Gullón M., Pons J. A., Perna R., Dainotti M. G., Miralles J. A., Torres D. F., 2015, *ApJ*, 813, 92

Rees M. J., Meszaros P., 1992, *MNRAS*, 258, 41P

Rees M. J., Meszaros P., 1994, *ApJL*, 430, L93

Rees M. J., Mészáros P., 1998, *ApJL*, 496, L1

Rhoads J. E., 1999, *ApJ*, 525, 737

Ripa J., Mészáros A., 2015, preprint

Ritz S. M., Gehrels N., McEnery J. E., Meegan C., Michelson P. F., Thompson D. J., Team F. M., 2009, Bulletin of the AAS, 41, 416

Roming P. W. A., et al., 2005, Space Science Rev., 120, 95

Rosswog S., 2007, MNRAS, 376, L48

Rosswog S., Ramirez-Ruiz E., Davies M. B., 2003, MNRAS, 345, 1077

Rowlinson A., et al., 2010, MNRAS, 409, 531

Rowlinson A., O'Brien P. T., Metzger B. D., Tanvir N. R., Levan A. J., 2013, MNRAS, 430, 1061

Ryan G., Van Eerten H., MacFadyen A., Zhang B.-B., 2015, ApJ, 799, 3

Sakamoto T., et al., 2016, GRB Coordinates Network, 19276

Salvaterra R., et al., 2012, ApJ, 749, 68

Sari R., Piran T., Narayan R., 1998, ApJL, 497, L17

Sari R., Piran T., Halpern J. P., 1999, ApJL, 519, L17

Savchenko V., et al., 2017, ApJL, 848

Selsing J., et al., 2016, GRB Coordinates Network, 19274

Shapiro I. I., 1964, Phys. Rev. Lett., 13, 789

Shapiro S. L., Teukolsky S. A., 1983, Black Holes, White Dwarfs, and Neutron Stars: The physics of compact objects. Wiley-VCH

Soderberg A. M., Berger E., Ofek E., 2005, GRB Coordinates Network, 4186

Soderberg A. M., et al., 2006, ApJ, 650, 261

Sonbas E., MacLachlan G. A., Shenoy A., Dhuga K. S., Parke W. C., 2013, ApJL, 767, L28

Stanek K. Z., et al., 2003, ApJL, 591, L17

Svensson K. M., Levan A. J., Tanvir N. R., Fruchter A. S., Strolger L.-G., 2010, MNRAS, 405, 57

Swenson C. A., Roming P. W. A., 2014, ApJ, 788, 30

Tanvir N. R., et al., 2009, Nature, 461, 1254

Tanvir N. R., Xu D., Kruehler T., Malesani D., Fynbo J. P. U., Pugliese G., Levan A. J., Cano Z., 2016, GRB Coordinates Network, 19350

Thompson C., Duncan R. C., 1993, ApJ, 408, 194

Thompson C., Duncan R. C., 1995, MNRAS, 275, 255

Thompson T. A., Quataert E., Burrows A., 2005, ApJ, 620, 861

Troja E., et al., 2007, ApJ, 665, 599

Tunnicliffe R. L., et al., 2014, MNRAS, 437, 1495

Usov V. V., 1992, Nature, 357, 472

Villar V. A., et al., 2017, arXiv preprint arXiv:1710.11576

Wainwright C., Berger E., Penprase B. E., 2007, ApJ, 657, 367

Wang F., Dai Z., 2013, Nature Physics, 9, 465

Wang X., Loeb A., 2000, ApJ, 535, 788

Wijers R. A. M. J., Galama T. J., 1999, ApJ, 523, 177

Willingale R., Genet F., Granot J., O'Brien P. T., 2010, MNRAS, 403, 1296

Winkler C., Pace O., Volonté S., 1993, ESA J., 17, 207

Woosley S. E., 1993, ApJ, 405, 273

Xu D., et al., 2009, ApJ, 696, 971

Zhang B., 2007, Chinese J. Astron. Astrophys., 7, 1

Zhang B., Mészáros P., 2001, ApJL, 552, L35

Zhang B., Mészáros P., 2002, ApJ, 566, 712

Zhang B., Mészáros P., 2004, International Journal of Modern Physics A, 19, 2385

Zhang B., Yan H., 2011, ApJ, 726, 90

Zhang B., Fan Y. Z., Dyks J., Kobayashi S., Mészáros P., Burrows D. N., Nousek J. A., Gehrels N., 2006, ApJ, 642, 354

Zhang B., Zhang B.-B., Liang E.-W., Gehrels N., Burrows D. N., Mészáros P., 2007, ApJL, 655, L25

van Paradijs J., et al., 1997, Nature, 386, 686